2009

Testing of GdCl3 Doping in Water Cherenkov Antineutrino Detectors

William Fitzgerald Coleman
Louisiana State University and Agricultural and Mechanical College, wcolem2@lsu.edu

Recommended Citation

Coleman, William Fitzgerald, "Testing of GdCl3 Doping in Water Cherenkov Antineutrino Detectors" (2009). *LSU Doctoral Dissertations*. 84.
https://digitalcommons.lsu.edu/gradschool_dissertations/84

TESTING OF GdCl3 DOPING IN WATER CHERENKOV ANTINEUTRINO DETECTORS

A Dissertation
Submitted to the Graduate Faculty of the
Louisiana State University and
Agricultural and Mechanical College
in partial fulllment of the
requirements for the degree of
Doctor of Philosophy

in

The Department of Physics and Astronomy

by
Willam Fitzgerald Coleman
B.S., Southeastern Louisiana University, 1983
M.S., Naval Postgraduate School, 1991
December 2009

Acknowledgements

I would like to express my deepest appreciation and thanks to Professor Bob Svoboda for his guidance and for his friendship over the past 4 1/2 years. It seems a lifetime ago since I sent that first email from the Avondale Shipyard expressing an interest in returning to school. I am here today because of Bob's interest and encouragement.

I would like to thank Professor Bill Metcalf for his patience and understanding. I thank him most of all for pulling this dissertation out of me and putting me back on track when I was derailed.

I would like to thank Dr. Steven Dazeley at LLNL. Steven not only cheerfully answered my stupid questions and overlooked my many incompetences, he allowed me to piggy-back onto his experiment and uncomplainingly waited for me to take a year and a half to do what he could have done in much much less time.

I would like to thank Dr. Adam Bernstein and Dr. Nathaniel Bowden and the rest of the LLNL crew. Neither I nor my family will ever forget the opportunities that our LLNL experiences afforded us. For this I thank Bob and Steven as well.

I would like to thank Arnell Dangerfield, Ophelia Dudley, Beverly Rodriguez and Gay Sutton for their many kindnesses.

I would like to thank an old friend now deceased who I fondly remember.

I would like to thank my mother and father.

I would like to thank my son, Lucas. There are many disadvantages to being the 5-10 year old son of a physics graduate student. Lucas could give the details but he never did. It's time that we go sailing.

I would like to thank my wife, Nancy, for everything. Everything!

Table of Contents

List of Tables

List of Figures

Abstract

Improved neutron and neutrino detection using water Cherenkov detectors loaded with gadolinium has been proposed for potential application in both large and small volume detectors. In this thesis, work performed to determine the effect on transparency resulting from use of $GdCl_3$ in stainless steel constructed water Cherenkov detectors is presented. In addition, results of an experiment performed using a small volume water Cherenkov detector are reported. This was the first use of gadolinium loaded water to detect reactor antineutrinos.

Chapter 1

Introduction

Charged particles traveling through a material with a speed greater than c/n, where n is the refractive index, will emit Cherenkov photons. In a transparent material, these photons can be detected by using light sensitive detectors, such as photomultiplier tubes. Since pure water is very transparent compared to other materials, large, inexpensive water detectors can be built. In fact, such devices have been used for over twenty-five years in large mass neutrino experiments such as IMB, SNO, and Super-Kamiokande.

This thesis focuses on the use of a water Cherenkov detector for one type of neutrino experiment for detection of the inverse beta decay reaction on protons in the water, $\overline{\nu}_e + p \rightarrow n + e^+$, which produces a positron and neutron. The Cherenkov light from the positron is easily detectable. This is not the case for the uncharged neutron which is only detectable in this type of device via the gammas that are emitted after it captures on protons in the water. The result of the neutron capture on a proton is a 2.2 MeV gamma ray. Since water has a refractive index of 1.33, an electron must have a kinetic energy greater than

$$m_e c^2 \left[\frac{n}{(n^2-1)^{1/2}} - 1 \right] = 0.26 MeV$$

before it can emit light. Since the 2.2 MeV gamma energy is typically spread over several Compton scattered electrons, the result is that only a small amount of detectable light is emitted per neutron capture.

If one dopes the water with a nucleus that emits higher energy neutron capture gammas, however, this situation can be improved. For example, gadolinium, which can be introduced via the water-soluble compound gadolinium tri-chloride, $GdCl_3$, emits an 8 MeV gamma cascade that should increase the number of detectable photomultiplier hits for even a small-volume ($\sim$1m^3) Cherenkov detector. In addition, with an average cross section of 40,000 b compared to 0.2 b for hydrogen, the neutron captures following inverse beta decays will be dominated by gadolinium even at small concentrations.

The ability to observe the double-coincidence signature of the positron and neutron energy depositions from inverse beta decay in a water Cherenkov detector has important physics and nuclear security applications. For example:

- For large Super-Kamiokande type detectors, the ability to observe the double-coincidence signature of the positron and neutron energy depositions from inverse beta decay would substantially reduce troublesome backgrounds in searches for ν_e and $\overline{\nu}_e$ from the Diffuse Supernova Neutrino Background (DSNB)[1] [1]. Also $GdCl_3$ doping would allow precise extraction of the antineutrino time structure from a Galactic Supernova burst. In addition, the capability of a water Cherenkov detector to observe both neutrinos and antineutrinos would expand the physics reach of these detectors greatly. For example, experimenters could test for the Standard Solar Model (SSM) prediction that no antineutrinos should be present in the solar neutrino flux. A $GdCl_3$-doped water Cherenkov SK-type detector would allow confirmation of this prediction at the precision of 1 antineutrino out of 10,000 neutrinos. Likewise, neutron detection would add the capability to differentiate neutrino from antineutrino interactions in the neutrinos generated by cosmic rays in Earth's atmosphere.

- Neutrons are an important background for experiments searching for Weakly Interacting Massive Particles (WIMPs). WIMP detectors work with a very low energy threshold, and are sensitive to and require to be shielded from neutrons from all possible sources. Since neutrons and WIMPs both induce nuclear recoils it is crucial that the neutron flux be suppressed. A neutron detecting water Cherenkov detector could serve as an active neutron shield with the capability of tagging neutrons produced *inside* and outside the detector.

---

[1] The DSNB is described in detail in chapter 2.

- This type of detector would make possible the construction of large water Cherenkov detectors which could be used as neutron radiation detectors. Such devices would have a very large acceptance and rely on coincident neutron detection to find Special Nuclear Material (SNM) buried inside cargo containers. This would potentially be very fast, easy to operate, and environmentally friendly compared to existing detectors.

- Another nuclear security application which is addressed specifically by this thesis is that of using $GdCl_3$ doped water Cherenkov detectors for nuclear reactor monitoring.

Before any of these potential applications can be pursued, several potential questions involved in determining whether or not it is feasible to use $GdCl_3$ in water need to be investigated. These are: Is the transparency of the $GdCl_3$ doped water still high enough to allow propagation of ultraviolet Cherenkov photons over long distances? What will be the effects of the dopant on detector materials? Is the light generated by the 8 MeV gamma cascade sufficient to make a water Cherenkov detector feasible? This thesis will address these questions in detail. The following paragraphs summarize the content of this thesis.

Chapter 2 gives an historical overview of neutrino physics and includes a discussion of neutrino properties, interactions, sources and areas of current neutrino research. In Chapter 3, the methods for detection of a particle so elusive that it has been termed, the “ghost particle” are described. This chapter also includes a detailed description and explanation of water Cherenkov detectors and describes the detection of the signature inverse beta decay reaction resulting from the capture of the product neutron on a dopant in water.

In Chapter 4, experiments conducted at Lawrence Livermore National Laboratory (LLNL) to determine the feasibility of using $GdCl_3$ as a dopant in water are described. The theoretical basis for the experiments and a detailed description of the experimental apparatus, methods and procedure is presented. In addition, the uncertainties associated with these experiments as well as results and conclusions for the use of $GdCl_3$ in water are given. These results are published in [2].

In Chapter 5, the topic of the second major focus of this thesis is introduced by describing a $GdCl_3$ doped water Cherenkov detector and its potential use in nuclear reactor monitoring.

To set the stage for the detailed discussion of this topic in Chapter 6, a description of the theoretical basis for using antineutrinos as a remote reactor monitoring tool is provided as is the results of an earlier reactor monitoring experiment using a liquid scintillator antineutrino detector.

Chapter 6 is devoted to analysis of the data from the SONGS water Cherenkov detector installed at the San Onofre Nuclear Generating Station in San Onofre, California. Two different techniques are used to determine the ability of this detector to observe reactor antineutrinos.

Chapter 7 provides a summary and conclusions.

Chapter 2

Overview of Neutrino Physics

Every cubic centimeter of space is suffused with particles called neutrinos which were formed immediately following the creation of the universe. Other sources produce these particles as well. For example, our sun produces prodigious numbers. Trillions stream directly from the sun through our bodies every second. Humans also produce these particles in high energy accelerators and at nuclear power reactors in equally mind-boggling numbers [3].

Our current understanding is that matter is comprised of only two types of particles: quarks and leptons. Quarks combine to form relatively heavy particles like protons and neutrons while leptons are further divided into two sub-types: the charged leptons and the uncharged neutrinos.

So, by our current understanding, neutrinos comprise one of nature's truly fundamental particles. Yet we know relatively little about them and recently, much of what we thought we knew about neutrinos has changed. In this chapter, we will discuss what is currently known.

2.1 Introduction and Historical Overview

By the early decades of the 20th century, physicists knew that matter was made up of atoms and that these atoms consisted of other smaller particles, protons and electrons. These two particles appeared to form the two fundamental building blocks of all matter. Yet it was clear early on that all was not well with this simple picture because from the very beginning, it was known that atoms disintegrate via radioactive decay.

One of the earliest studied atomic decay processes involved the emission of negatively charged electrons from an atomic nucleus in a process called negative beta decay (β^-). One striking feature of these β-decay electrons was that they had a continuous distribution of energies from zero up to some upper 'endpoint energy'. A source of confusion for early modern era physicists was that if β-decay was like another known two-body radioactive decay process (α-decay), the product β particles would have been expected to have a unique energy. Since this was not the case, several hypotheses to account for the 'missing' energy were proposed but eventually ruled out by subsequent experiments [4]. By 1930, Niels Bohr was positing the restricted validity of the principle of energy conservation (not for the first or last time) [5] to account for the β particle energy distribution. Because of it's proven use in all other fields of physics, Wolfgang Pauli would not accept Bohr's energy non-conservation hypothesis and in a famous letter to a gathering of "Radioactive Ladies and Gentlemen" meeting in Tübingen, he countered with what he self-termed a 'desperate remedy' to save the conservation of energy, momentum and angular momentum. In his letter, Pauli developed the idea that during β^- decay, in addition to the electron, an electrically neutral particle is emitted in such a way that the sum of energies of both particles is constant.

Enrico Fermi took up Pauli's idea and from it developed what is now known as the 'Fermi Theory of β Decay'. It was also Fermi who would give this little neutral particle its name [6] [7]. It would take twenty-five years before experimental proof of the existence of the neutrino was obtained and many years more before a consensus theoretical understanding of particle physics placed the neutrino properly in the elementary particle hierarchy.

From Desperate Remedy to Standard Model Particle

Within the Standard Model of Particle Physics all of the elementary particles are grouped into three generations, each with two quarks and two leptons (see Figure 2.1) [8].

Ordinary matter is built from the constituents of the lightest generation: the up and down quarks which make up protons and neutrons, the electron and the electron neutrino, ν_e, which is involved in negative beta decay. Heavier versions of each of these particles comprise the

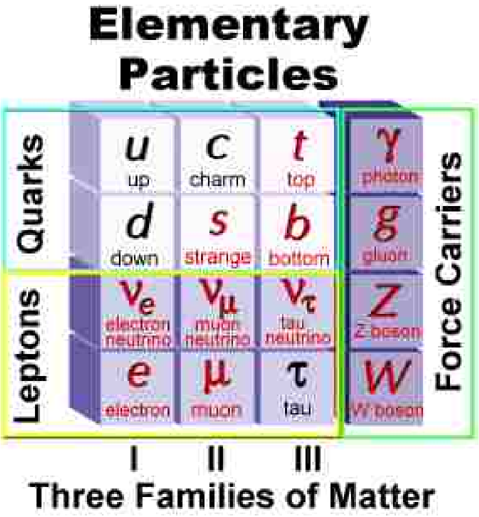

Figure 2.1: The Elementary particles within the Standard Model.

second and third generations. Each of these particles have a corresponding antiparticle with opposite electric charge.[1] The Standard Model also includes three of the fundamental forces of Nature, the strong, electromagnetic and weak forces but does not include gravity because General Relativity which describes gravity cannot be integrated with quantum mechanics at high energies using the framework of quantum field theory. The spin-1 gauge bosons (to the right in the figure) mediate interactions among the fermions (spin-1/2) on the left. In QED, interactions among electrically charged particles are due to the exchange of massless photons (γ). The strong force of quantum chromodynamics (QCD) is mediated by the exchange of massless gluons (g) between quarks that carry a quantum number called color. Unlike the case of photons, the gluons, or quanta of the 'chromomagnetic' field possess color charge and so couple to one another. Because of this the color force between two colored particles increases in strength with increasing distance and hence quarks and gluons cannot appear as free particles but exist only in composite particles like protons and neutrons. The third of the fundamental interactions is the weak force which is associated with the charged W and neutral Z bosons that mediate it. Because the W bosons are electrically charged they also couple to the γ's. This requires a gauge theory that unites the weak and electromagnetic interactions similar to that in QCD [9].

---

[1] In the Standard Model, neutrinos are massless.

In the Standard Model, neutrinos interact only via the weak interaction. However, due to the large mass of the weak force bosons ($\approx$ 90 MeV/c^2), which have a mean lifetime of about 3x10^{-27} sec, the resulting range of the weak interaction is less that 10^{-18} m. It is the very small weak force interaction range that is the reason the neutrino can traverse the universe virtually unhindered and makes the neutrino so extremely difficult to detect.

The neutrino interactions described by Fermi's theory involved electrons. In 1962 it was discovered that the neutrinos produced in pion decay produce muons, not electrons, when they interact with matter [10]. This suggested that there were at least two kinds of neutrinos, termed electron-neutrinos and muon-neutrinos.

Likewise, when the τ lepton was discovered in 1975 [11] the existence of a τ neutrino was immediately inferred. The interaction of the ν_τ was first observed in 2001 [12]. These three appear to be all of the active types of neutrinos since a study of the decay widths of the Z boson shows that there are 2.984 ± 0.008 neutrino flavors which couple to the Z[2] [8] [13].

The Standard Model does not predict the mass of the fundamental particles but it does provide a mechanism whereby these particles acquire a mass via the Higgs field which is postulated to permeate all space. Particles that interact with the Higgs field cannot propagate at the speed of light and thus, in analogy with the index of refraction that slows a photon traversing matter, these particles acquire a mass proportional to their interaction rate with the Higgs field.

It was previously mentioned that the neutrino interacts only via the weak interaction. In the weak interaction the W bosons couple only to left-handed particles. Indeed, the fact that neutrinos are left-handed had been well established by 1958 from the study of electron capture on ^{152}Eu [14]. But in the Standard Model, the handedness of a particle may change when it interacts with the Higgs field. This implies that the neutrino has to be massless if the Standard Model is a complete theory[3] [3].

---

[2] Strictly, this limit to the number of neutrino families applies only to light neutrinos, with masses below half the Z mass.

[3] Perhaps a more direct way to understand why neutrino mass is forbidden in the Standard Model is to understand that if a neutrino has mass then according to special relativity, it can never travel at the speed of light and, in principle, an observer traveling faster than the neutrino could overtake it and observe a right-handed neutrino not described by the Standard Model.

But of course, the Standard Model is *not* a complete theory since it does not include gravity. Although gravity plays no significant role in most atomic and subatomic processes because the strength of gravity only approaches the other fundamental forces at the Planck scale ($\sim 1\times 10^{28}$ eV), a theory of fundamental interactions that does not include it can posit no claims of completeness. Other evidence of physics beyond the Standard Model comes from astronomical observations indicating the existence of an unknown type of matter and energy comprising 96% of the mass-energy of the Universe [15]! However, the most compelling confirmed evidence for physics beyond the Standard Model was the announcement by the Super-Kamiokande collaboration in June 1998 that it had obtained the first evidence for neutrino oscillations which imply neutrino mass [16].

There are two basic ways to extend the Standard Model in order to produce massive neutrinos. The first way incorporates the concept of a Dirac neutrino. The mass of Dirac neutrinos can be generated via the Higgs mechanism. However, this model suggests that the neutrinos should have masses similar to the other particles in the Standard Model. Since this is clearly not the case, the strength of neutrino interactions with the Higgs boson must be at least 12 orders of magnitude weaker than that of the top quark. For this reason this theory is not favored by most neutrino physicists.

A second way to extend the Standard Model to incorporate neutrino mass involves lepton number-violating Majorana neutrinos which are their own antiparticles. The mass producing mechanism in this case follows from the idea that in the condition that a particle can be its own antiparticle, an observer who overtakes a left-handed neutrino and sees a right-handed neutrino really sees a right-handed *antineutrino*. So there is no contradiction to the Standard Model prohibition against right handed neutrinos. In this case, it is possible for right-handed neutrinos to have a mass of their own without relying on the Higgs boson [17]. The mass of the right-handed neutrino, M, is not tied to the mass scale of the Higgs boson and can be much heavier than other particles. When a left-handed neutrino collides with the Higgs boson, it acquires a mass, m, which is comparable to the mass of other quarks and leptons. At the same time it can transform into a right-handed neutrino which is much heavier than energy conservation would normally allow. However, the Heisenberg uncertainty principle allows this state to exist for a short time interval, Δt, given by $\Delta t \sim h/Mc^2$, after which the particle transforms back into a left-handed neutrino with mass m by colliding with the Higgs boson again. Therefore, one can think of the neutrino as having an average mass of m^2/M over time.

This "seesaw mechanism" [18] [19] can naturally give rise to light neutrinos with normal-strength interactions if M is much larger than the typical masses of quarks and leptons. Right-handed neutrinos must therefore be very heavy, as predicted by grand-unified theories that aim to combine electromagnetism with the strong and weak interactions. For a short review of neutrino mass models, particularly see-saw models involving three active neutrinos see reference [17].

2.2 Neutrino Sources

A brief survey of neutrino sources is provided below:

- **Relic Neutrinos**: According to standard cosmology, not only should neutrinos be abundant - second only to the Cosmic Microwave Background (CMB) photons - but since these decoupled from the Big Bang thermal soup about 1 second after the birth of the Universe, these neutrinos should be the oldest particles existent.[4] The relic neutrinos are comprised of all three neutrino flavors and have energies corresponding to an effective temperature of about 2 K ($\approx$ 0.17 meV) [20].

  The CMB photons and the primordial abundances of the light elements are widely regarded as two strong observational 'pillars' supporting the standard Big Bang model of the Universe. But detection of relic neutrinos with the predicted thermal spectrum would be perhaps the cleanest evidence for the standard Big-Bang model because it would be difficult to explain their thermal background via any other hypothesis [21].

---

[4] Dark Matter WIMPs - if they exist - would be older.

- **Supernova and the Diffuse Supernova Background**: Another source of astrophysical neutrinos are both individual supernovae and the Diffuse Supernova Neutrino Background (DSNB) resulting from all supernova explosions occurring throughout the Universe since the beginning of stellar formation. These neutrinos come from cooling of the proto-neutron star after collapse. Supernovae occur somewhere in our Universe about once every second but although the current generation of neutrino detectors can detect the transient signal from a supernova in our Milky Way, the expected signal from a supernova in a more distant galaxy is fewer than one event. Likewise, efforts to detect the DSNB have not yet been successful [22]. A proposal to improve the Super-Kamiokande DSNB detection capability motivated the work presented in Chapter 4 of this thesis.

- **Geo-neutrinos**: Geo-neutrinos are neutrinos and antineutrinos from the decay of ^{238}U, ^{232}Th, and ^{40}K in the Earth's crust and mantel [23]. Earth composition models suggest that about 16 TW of the Earth's heat generation come from these decays (about 40% of the Earth's total heat dissipation). Radiogenic heat is therefore an essential component of the present dynamics of our planet. It is possible that these phenomena could be directly studied through detection of geo-neutrinos [24].

- **Nuclear Power Reactors**: Nuclear power reactors emit large numbers of antineutrinos, about 6×10^{20} $\overline{\nu}_e$ per second, broadly distributed over energies up to about 12 MeV with a peak at $\sim$ 0.3 MeV [25]. From the first detection of the antineutrino by Reines and Cowan in 1956 to the observation of reactor antineutrino disappearance at KamLAND, reactor neutrino experiments have played a major role in the development of neutrino physics over the past 50 years. Reactor antineutrinos and antineutrino detection will be addressed in detail in Chapter 3.

- **Solar Neutrinos**: The sun is powered by a main fusion chain -the proton-proton chain - whereby a proton transmutes into a neutron close enough to another proton for the resulting neutron and proton to bind together to make a deuteron. The deuteron combines with another proton to form helium-3 and then two helium-3 nuclei can react with another helium-3 nucleus to form stable helium-4. This branch of the proton-proton chain is termed the pp I-process. A second major branch of the proton-proton chain (the pp II-process) leads to the production of helium with a probability of $\sim 15\%$ via $^7\text{Be} + e^- \rightarrow {}^7\text{Li} + \nu_e$. From the proton-proton chain, two ν_e are produced with energies less than 0.42 MeV for the I-process and either 0.862 MeV(90%) or 0.383 MeV(10%) for the pp-II process[5] [26].

The expected number of neutrinos can be easily calculated from the Sun's measured luminosity (3.86×10^{26} joules per second) and from knowledge that approximately 25 MeV (4×10^{-12} joules) is released in forming each helium nucleus. The total number of solar neutrinos produced is therefore around 2×10^{38} per second [27].

- **Atmospheric Neutrinos**: Another source of neutrinos are as the decay products of hadrons (mainly pions and kaons) produced by cosmic ray interactions in the atmosphere. These "atmospheric neutrinos" are primarily ν_e and ν_μ.

  The pions and kaons decay predominantly into $\mu^\pm + \nu_\mu(\overline{\nu}_\mu)$ and then the product muons decay as $e^\pm + \nu_e(\overline{\nu}_e) + \overline{\nu}_\mu(\nu_\mu)$. Supposing that all the pions and kaons and muons decay, one would expect about two muon-like neutrinos for each electron-like neutrino and for the ratio $\nu_e/\overline{\nu}_e$ to be close to the ratio μ^+/μ^-. The theoretical uncertainty for the individual fluxes is about 10% [29] but predictions for the ratio $r = \phi_{\nu_\mu}/\phi_{\nu_e}$ agree to about 2% [28].

- **Accelerator Neutrinos**: Neutrinos can also be produced at accelerators. This idea was proposed independently by Schwartz [30] and Pontecorvo [31]. Using accelerators, neutrino beams are produced from the decays of charged π and K mesons, which in turn are created from proton beams striking thick nuclear targets. Proton beam energies of 1-10 GeV can produce neutrinos of several MeV up to several GeV energies. A detailed review of accelerator neutrino physics is provided in [32].

---

[5] The pp cycle produces 98.4% of the solar energy and there are other branches of this cycle than the two main branches described here. Of particular interest is the decay of $^8\text{B} \rightarrow {}^8\text{Be} + e^+ + \nu_e$. Although less than $10^{-4}\%$ of the neutrino flux comes from this decay, these neutrinos are the most easily detected due to their higher energy ($E_\nu \approx 15$ MeV).

Table 2.1: Neutrino Energies, Sources and Flavors

Energy Range	Source	$\nu/\overline{\nu}$ flavor
$\sim$ 0.0017 eV	Relic (Big Bang)	all
1-40 MeV	SuperNova/DSNB	all
$\sim$ 1 MeV	GeoNeutrinos	$\overline{\nu}_e$
1-8 MeV	Nuclear Reactors	$\overline{\nu}_e$
0.5-19 MeV	Solar	ν_e
100 MeV→ 10 TeV	Cosmic rays (Atmospheric)	ν_μ, $\overline{\nu}_\mu$, ν_e
0.5 GeV-300 GeV	Accelerator	ν_μ, $\overline{\nu}_\mu$, fractions of others

Table 2.1 and Figure 2.2 summarizes the neutrino energies, sources and flavors and fluxes produced by the sources that we have discussed. In the next section, we shall discuss in more detail the properties of neutrinos including the origin and mechanism of neutrino oscillations.

2.3 Neutrino Oscillations

The idea of neutrino oscillation was first discussed by Pontecorvo in 1967 in the context of the possibility of solar neutrino oscillations [34]. The idea is straight-forward: If the flavor states are superpositions of mass eigenstates then the probabilities that the flavor state α will oscillate into the flavor state β or remain an α are for the case of two component mixing:

$$P(\nu_\alpha \to \nu_\beta) = \sin^2(2\theta)\sin^2(\frac{1.27\Delta\mathrm{m}^2(\mathrm{eV}^2)\mathrm{L(km)}}{\mathrm{E(GeV)}}) \tag{2.3.1}$$

and

$$P(\nu_\alpha \to \nu_\alpha) = 1 - P(\nu_\alpha \to \nu_\beta). \tag{2.3.2}$$

where E is the neutrino energy, $\Delta\mathrm{m}^2$ is the difference of the mass eigenvalues squared: $\Delta\mathrm{m}^2 = \mathrm{m}_2^2 - \mathrm{m}_1^2$ and θ is the mixing angle between the two mass states. Note that oscillation experiments can only measure the differences in m^2 and not the neutrino masses themselves.

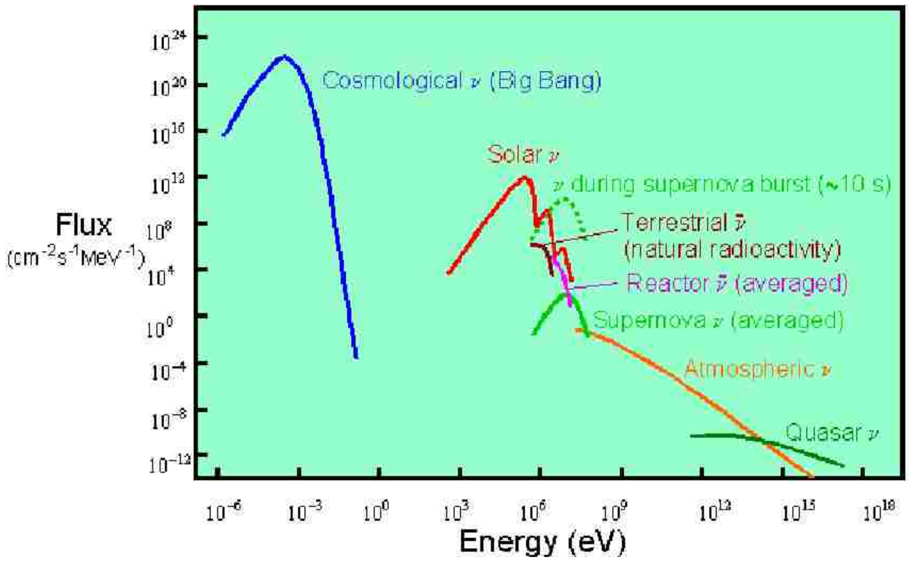

Figure 2.2: Flux on Earth of neutrinos from the various non-accelerator sources discussed in this section. Figure taken from [33].

On the other hand, these experiments are sensitive to mass differences much smaller than direct neutrino mass measurements.

For the case of three mixing neutrinos, the oscillation probabilities depend on two differences of the mass squares[6], three mixing angles between the three mass states and three separate phases as discussed below.

By standard convention, these parameters are expressed via the Maki-Nagakawa-Sakata (MNS) unitary mixing matrix [84]

$$\begin{pmatrix} U_{e1} & U_{e2} & U_{e3} \\ U_{\mu 1} & U_{\mu 2} & U_{\mu 3} \\ U_{\tau 1} & U_{\tau 2} & U_{\tau 3} \end{pmatrix} =$$

$$\begin{pmatrix} 1 & 0 & 0 \\ 0 & \cos\theta_{23} & \sin\theta_{23} \\ 0 & -\sin\theta_{23} & \cos\theta_{23} \end{pmatrix} \times \begin{pmatrix} \cos\theta_{13} & 0 & e^{-i\delta_{CP}}\sin\theta_{13} \\ 0 & 1 & 0 \\ -e^{i\delta_{CP}}\sin\theta_{13} & 0 & \cos\theta_{13} \end{pmatrix} \times$$

---

[6] One of the Δm^2_{ij} is determined by the condition $\Delta m^2_{12} + \Delta m^2_{23} + \Delta m^2_{31} = 0$.

$$\begin{pmatrix} \cos\theta_{12} & \sin\theta_{12} & 0 \\ -\sin\theta_{12} & \cos\theta_{12} & 0 \\ 0 & 0 & 1 \end{pmatrix} \times \begin{pmatrix} e^{i\alpha/2} & 0 & 0 \\ 0 & e^{i\alpha/2+i\beta} & 0 \\ 0 & 0 & 1 \end{pmatrix}. \qquad (2.3.3)$$

The contribution of the mass state j to the flavor state i is given by the squared modulus of the matrix element U_{ij}. In Equation 2.3.3, the first matrix describes the mixing in the atmospheric neutrino sector. The second matrix is associated with reactor neutrino oscillations and off-axis beam experiments. This matrix also contains the phase, δ_{CP}, related to CP violation. This term is due to quark-lepton symmetry which suggests that the mixing matrix should violate CP invariance. In analogy with the Cabibbo-Kobayashi-Maskawa (CKM) matrix which characterizes mixing of quarks, this is accomplished by making $\sin\theta_{13}$ complex, i.e. $\sin\theta_{13} = |\sin\theta_{13}|\ e^{i\delta}$ [35]. Note that the possibility of observing CP violation in neutrino oscillation experiments depends entirely on a measurable non-zero value of $\sin\theta_{13}$. The physics of the third matrix is associated with solar neutrino oscillations. The fourth matrix on the right hand side of Equation 2.3.3 contains what are called the Majorana phases, α and β, which are important in the neutrinoless double beta decay process. One additional item important in neutrino oscillation physics should be mentioned. This is that neutrinos traveling through a medium of high density are effected by the matter they travel through in ways which are not reflected in Eqs. 2.3.1 - 2.3.3. Specifically, ν_e can interact with electrons via W and Z while the ν_μ and ν_τ neutrinos can only interact with electrons via the Z boson. When neutrinos travel through regions with no muons and taus, the ν_e eigenstates will propagate differently than the ν_μ and ν_τ eigenstates. The end result is that the oscillation length and mixing angles are modified by factors that depend on the electron density of the matter. This is the so-called Mikikheyev, Smirnov, Wolfenstein (MSW) effect. It can effect solar neutrinos as they travel outwards from the sun or as they cross earth and can have important implications for solar and supernova neutrino experiments [36] [37].

2.4 Neutrino Oscillation Experiments

2.4.1 Solar Oscillation Experiments

Solar neutrinos have been studied in the SAGE, GALLEX, Kamiokande, Super-Kamiokande and SNO experiments (plus others) [38]. These followed the Homestake experiments of Ray Davis [39] that initially uncovered the solar ν puzzle wherein a less than predicted flux of solar neutrinos was measured. The solution to this puzzle is now almost universally accepted: ν_e produced in the sun change flavor through flavor oscillation (described through the parameters θ_{12} and $\Delta \mathrm{m}_{12}^2$) and the MSW effect. The convincing evidence for this solution was provided by the SNO experiment [40] [41] which confirmed the initial calculation of ν_e flux production in the sun. The beauty of the SNO detector is that it can simultaneously measure the ν_e flux from the reaction $\nu_e + d \to p + p + e^-$ (a charged-current reaction) and the total neutrino flux ($\nu_e + \nu_\mu + \nu_\tau$) in the reactions $\nu_x + d \to n + p + \nu_x$ (a neutral current reaction). The cross-section for the NC reaction is the same for each type of neutrino. Only ν_e's are produced in the Sun so if ν_μ and ν_τ are measured, they must originate from ν_e oscillation.

The fluxes measured at SNO are:

$$\Phi_{CC} = (1.76 \pm 0.05 \pm 0.09) \times 10^6 \text{ cm}^{-2}\text{sec}^{-1},$$

$$\Phi_{NC} = (5.09^{+0.44+0.46}_{-0.43-043}) \times 10^6 \text{ cm}^{-2}\text{sec}^{-1}.$$

These results indicate that the charged current flux has been reduced while the total flux, $\nu_e + \nu_\mu + \nu_\tau$, from the neutral current reaction agrees with that of the prediction from solar theoretical calculations: $\Phi_{NC} = (5.05 \pm 1) \times 10^6 \text{ cm}^{-2}\text{sec}^{-1}$.

The SNO results when combined that of KamLAND and that of other solar neutrino data, especially Super-Kamiokande, uniquely specify the large mixing angle (LMA) MSW solar solution with three active light neutrino states. According to recent global fits, the best values of the fitted parameters are: $\Delta \mathrm{m}_{12}^2 \approx 7.59 \times 10^{-5}\mathrm{eV}^2$, $\sin^2\theta_{12} \approx 0.30$ [42] [43].

Also, recently the Borexino collaboration reported the direct measurement of the ^{7}Be solar neutrino signal measured with its low background liquid scintillator detector. This was the first real-time spectral measurement of sub-MeV solar neutrinos. The result for 0.862 MeV ^{7}Be neutrinos of 47 $\pm 7_{stat} \pm 12_{sys}$ counts/(day·100 ton), is consistent with predictions of the Standard Solar Model and neutrino oscillations with LMA-MSW parameters [44].

2.4.2 Atmospheric Neutrino Oscillation Experiments

Beginning in the 1980s, the IMB and Super-Kamiokande experiments (plus others: Soudan2, Frejus, Nusex) measured the number of atmospheric muon neutrino events compared to electron neutrino events by reporting the double-ratio

$$\frac{(N_\mu/N_e)_{data}}{(N_\mu/N_e)_{predicted}}.$$

In all but the Frejus and Nusex cases[7], the ratio obtained was about 60% the expected value of unity, which would result assuming no oscillations. Later measurements at Super-Kamiokande (SK) [45] of ν_μ and ν_e fluxes as functions of the zenith angle indicated that they were directly related to the length of the neutrino path through the Earth. Measurements of the asymmetry between the fluxes of the upward-going and downward-going muons give $-0.303 \pm 0.030 \pm 0.004$ which is significantly different from an asymmetry value of zero which would have been expected without oscillation. Since atmospheric neutrinos reaching SK from below travel further, the fact that SK detected fewer muon neutrinos traveling upward is consistent with an interpretation that some muon neutrinos have oscillated into another flavor while traveling trough Earth.

No corresponding enhancement of upward-going ν_e was observed, pointing to the oscillations $\nu_\mu \rightarrow \nu_\tau$ described by the parameters θ_{23} and $\Delta \mathrm{m}^2_{23}$. The current best fit values of the oscillations parameters are $\sin^2 2\theta_{23} = 1.0, \Delta \mathrm{m}_{23}{}^2 = 2.5 \times 10^{-3}$ eV^2 [48].

2.4.3 Accelerator Neutrino Oscillation Experiments

The first accelerator long baseline neutrino oscillation experiment was K2K [45]. Neutrinos (ν_μ) from a beamline source were detected at Super-Kamiokande after traversing a distance

---

[7] The Frejus and Nusex experiments had relatively low statistics compared to the other experiments.

of 250km. The average energy of the ν_μ beam was ≈ 1.3 GeV so that E/L corresponded to the atmospheric neutrino oscillation region. Comparison of the ν_μ flux and energy spectrum measured at Super-Kamiokande with that predicted by those observed in a detector near the source indicate a ν_μ flux depletion and modification of the energy spectrum. The K2K data confirm the $\nu_\mu \rightarrow \nu_\tau$ oscillation as measured by Super-Kamiokande for the atmospheric neutrinos and provide best fit values of the oscillation parameters of $\sin^2 2\theta_{23} = 1.0, \Delta\mathrm{m_{23}}^2 = 2.8 \times 10^{-3}\ \mathrm{e}V^2$ [47].

MINOS (Main Injector Neutrino Oscillation Search) with a neutrino beam pointed from Fermilab to the Soudan mine in Minnesota (a 735km baseline) started running in 2005. The recently reported results of their search for ν_μ disappearance are $\sin^2 2\theta_{23} > 0.9, \Delta\mathrm{m_{23}}^2 = (2.43 \pm 0.13) \times 10^{-3}\ \mathrm{e}V^2$ [49].

2.4.4 Reactor Oscillation Experiments

While the CHOOZ [50] and Palo Verde [51] reactor experiments did not observe disappearance of $\overline{\nu}_e$, for E/L values suggested by SK (and subsequently confirmed by K2K and MINOS), they did set limits on the mixing angle: $\sin^2 2\theta_{13} \leq 0.19$ at the 90% C.L. for $\Delta m_{13}^2 = 0.002eV^2$.

Another reactor experiment, KamLAND, observed an antineutrino flux of 0.658 ± 0.044(stat) $\pm$ 0.047(syst) of the expected signal for no oscillations from 30 reactors at an average distance of 180km [52]. These results confirmed antineutrino oscillations in the solar oscillation region manifested by suppression of initial antineutrino flux (1609 observed events versus 2179 ± 89 expected) and the modulation of the $\overline{\nu}_e$ energy spectrum [53].

2.4.5 Status of Current Oscillation Parameters

Four of the six oscillation parameters are at least approximately known [54]:

- $\Delta\mathrm{m}^2_{23}$ and θ_{23} based on the oscillations of the atmospheric and accelerator ν_μ neutrinos which correspond to maximal mixing of the mass states ν_2 and ν_3
- $\Delta\mathrm{m}^2_{12}$ and θ_{12} based on the oscillations of the solar ν_e neutrinos into the ν_μ and/or ν_τ neutrinos and of the reactor $\overline{\nu}_e$ into $\overline{\nu}_\mu$ and/or $\overline{\nu}_\tau$ which correspond to the large but not maximal mixing of the mass states ν_1 and ν_2.

The current status of all neutrino oscillation experiments is summarized in Figure 2.3. Although the figure is busy, the allowed atmospheric region can be identified ($\Delta m^2 \approx 3 \times 10^{-3} eV^2$) and corresponds to the region labeled "SuperK 90/99%". The allowed solar region ($\Delta m^2 \approx 8 \times 10^{-5} eV^2$) corresponds to the intersection of the upper SNO kidney shaped region with the thin upper KamLAND region. The possible mass spectra for three neutrinos are shown in Figure 2.4. In the figure, the neutrino spectrum is seen to contain 2 mass eigenstates separated by the splitting $\Delta m^2_{12} \approx 7{\times}10^{-5}$ eV^2 needed to explain the solar and KamLand data and a third mass eigenstate separated by the first two by the larger splitting $\Delta m^2_{23} \approx 2.1{\times}10^{-3}$ eV^2 required to explain the atmospheric, MINOS and K2K data.

The missing information is:

- θ_{13} which describes the sub-dominant oscillation $\nu_\mu \rightarrow \nu_e$ in the atmospheric region. At present we only know that the angle is small.
- The sign of Δm^2_{23} ($\mathrm{m}_3 > \mathrm{m}_1$ or $\mathrm{m}_3 < \mathrm{m}_1$).[8]
- The CP phase δ.

---

[8] The sign of Δm^2_{12} is positive since ν_2 is defined to be the heavier of the two mass eigenstates ν_1 and ν_2 in both the normal and inverted mass spectrum.

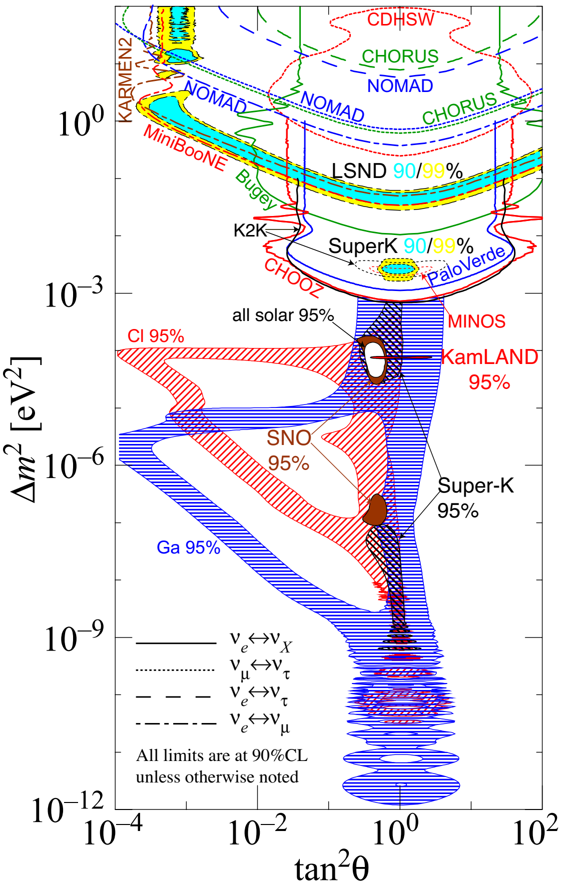

http://hitoshi.berkeley.edu/neutrino

Figure 2.3: Summary of the allowed regions from global analysis of atmospheric and solar neutrino experiments (from http://hitoshi.berkeley.edu/neutrino, 2008).

2.5 Future Experiments

In this section, a brief overview of some areas of current neutrino research are presented and future experiments are discussed.

2.5.1 Future Oscillation Experiments

The next generation of solar neutrino experiments will measure solar neutrinos with better energy resolution and a lower energy threshold. Three of these experiments are MOON (Molybdenum Observatory of Neutrinos) which will use ^{100}Mo, LENS (Low-Energy Neutrino Spectrometer) that will capture neutrinos on ^{176}Yb, and HERON (HElium Roton Observation of Neutrinos) which will use superfluid liquid helium to measure scintillation and the

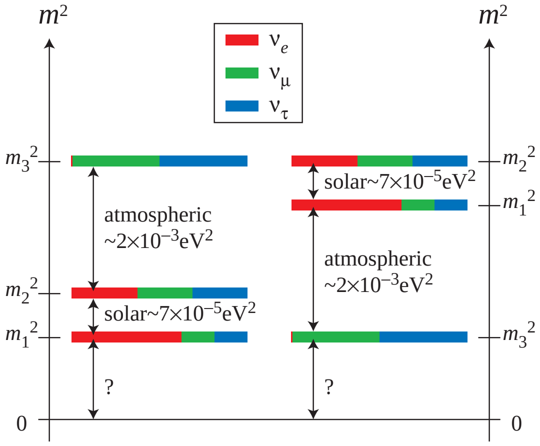

Figure 2.4: The two possibilities for the arrangement of neutrino mass. The normal hierarchy is shown on the left and the inverted hierarchy is shown on the right. In addition to not knowing the ordering of the masses, the zero of the scale is also not known. The colored bands indicate the probability of finding a particular weak eigenstate ν_e, ν_μ and ν_τ in a particular mass eigenstate. The figure is taken from [42].

phonons produced by neutrino interactions.

A primary goal of future neutrino experiments is measurement of θ_{13} [62] because of its importance in the physics of neutrino mixing, in CP violation and in the determination of neutrino hierarchy (normal: $m_{\nu_3} > m_{\nu_2} \approx m_{\nu_1}$ or inverted: $m_{\nu_2} \approx m_{\nu_1} > m_{\nu_3}$). Future experiments will accomplish this either by searching for ν_e appearance in the $\nu_\mu \to \nu_e$ oscillations or by looking for $\overline{\nu}_e$ flux suppression in a reactor disappearance experiment.

Two long baseline experiments (NuMI and CNGS) have recently started. The main goal of NuMI/MINOS [63] is improvement of the Δm^2_{23} and $\sin^2 2\theta_{23}$ values to about 10% whereas the goal of the CNGS experiment is to look for $\nu_\mu \to \nu_\tau$ appearance.

Starting in 2009, the SK detector will serve as the far detector for the T2K long baseline experiment [64] using an intense off-axis beam of protons (approaching 1MW) to produce $\nu_\mu s$. T2K expects to reach a sensitivity of 0.01 for $\sin^2 2\theta_{13}$ (at $\sin\delta = 0$). The NOνA experiment [65] will be another of the “second generation” long baseline experiments. It is off-axis of the NUMI neutrino beam and at a distance of about 800km from the ν_μ source. NOνA is planned to have a larger energy than T2K and will be sensitive to matter effects since at the NOνA baseline, matter effects on the ν_e component of the oscillating neutrino state are important.

These depend on the mass hierarchy, increasing the appearance probability for neutrinos for normal hierarchy over the inverted case (and conversely for antineutrinos). Via comparison of measurements using beams of ν vs. $\overline{\nu}$ these effects will provide the mechanism by which the NOνA experiment will address the question of normal or inverted neutrino hierarchy [66].

In the ν_e appearance experiments, the sub-dominant term in $\nu_\mu \longrightarrow \nu_e$ oscillations is proportional to $\sin^2 2\theta_{13}$.

The approximate expression[9] [62] is

$$\begin{aligned}
&P\left(\overline{\nu}_\mu \rightarrow \overline{\nu}_e\right) = \\
&\quad \sin^2\theta_{23}\sin^2\Delta_{13} + \tfrac{\Delta m^2_{21}}{\Delta m^2_{13}}\sin^2 2\theta_{13}\sin\delta_{CP}\cos\theta_{13}\sin 2\theta_{12}\sin 2\theta_{23}\sin^3\Delta_{13} \quad + \ldots \\
&P\left(\nu_\mu \rightarrow \nu_e\right) = \\
&\quad \sin^2\theta_{23}\sin^2\Delta_{13} - \tfrac{\Delta m^2_{21}}{\Delta m^2_{13}}\sin 2\theta_{13}\sin\delta_{CP}\cos\theta_{13}\sin 2\theta_{12}\sin 2\theta_{23}\sin^3\Delta_{13} \quad + \ldots
\end{aligned}$$

where $\Delta_{13} = \frac{\Delta m^2_{31} L}{4E+\nu}$. The above equations indicate that a non-zero value of $\sin 2\theta_{13}$ allows measurement of CP violation. In other words, one must measure $\sin 2\theta_{13}$ to determine the optimum measurements for CP violation.

The CP asymmetry in $\nu_\mu - \nu_e$ channel to leading order in the Δm^2 is given by [67]:

$$\frac{P(\nu_\mu \rightarrow \nu_e) - P(\overline{\nu}_\mu \rightarrow \overline{\nu}_e)}{P(\nu_\mu \rightarrow \nu_e) + P(\overline{\nu}_\mu \rightarrow \overline{\nu}_e)} = -\left(\frac{\sin 2\theta_{12}\sin 2\theta_{23}}{2\sin^2\theta_{23}}\right)\left(\frac{\sin 2\Delta_{12}}{\sin 2\theta_{13}}\right)\sin\delta_{CP} \tag{2.5.3}$$

However, there are potential ambiguities from the following parameter degeneracies [62]:

- the $\delta_{CP} - \theta_{13}$ ambiguity
- the $\Delta\mathrm{m}^2_{32}$ sign ambiguity
- the θ_{23} ambiguity (from the fact that $\sin^2 2\theta_{23}$ is measured not θ_{23})

The θ_{23} degeneracy can be overcome by combining results of experiments at different

---

[9] Matter effects are ignored.

baselines or optimizing the experimental set up [68] [69] however θ_{13} may still not be uniquely determined.

Reactor experiments offer a complimentary approach to θ_{13} determination through disappearance of $\overline{\nu}$ with the baseline corresponding to the atmospheric Δm^2_{23}. The advantage of this approach is that the survival probability of $\overline{\nu}$ directly measures $\sin^2 2\theta_{13}$ without parameter degeneracies resulting from Equation 2.5.4 [62]:

$$(\overline{\nu}_e \rightarrow \overline{\nu}_e) = 1 - \sin^2 2\theta_{13} \sin^2 \Delta_{13} - .... \tag{2.5.4}$$

Several designs have been proposed to improve sensitivity over the current best results from CHOOZ. These include Daya Bay in China [70], Double Chooz in France[71] and RENO [72] in Korea. The Daya Bay experiment will use eight identical detectors deployed at three locations. Civil construction began in February 2008. It is expected that data collection will begin in 2010. Sensitivity of 0.01 is expected in $\sin^2 2\theta_{13}$ with 3 years data. Meanwhile, the sensitivity of the Double Chooz experiment to $\sin^2 2\theta_{13}$ will reach 0.03 in 3.5 years using two detectors (a near detector at about 400m distance from the reactors and a far detector at a distance of about 1050m). Construction of the Double Chooz far detector is underway. The first Double Chooz neutrino event is expected by Spring 2010.

2.5.2 Absolute Mass Measurement Experiments

- **Direct Mass Measurements**

  The first suggestion of a method to directly determine the neutrino mass was included in Fermi's original paper on beta decay [7] where he proposed using the end-point energy of the β spectrum to measure this quantity. As Fermi noted, the largest possible electron energy is

  $$E_{max} = m_i - m_f - m_\nu$$

  where m_i is the mass of the initial nucleus and m_f is the mass of the final nucleus. From the β spectrum of tritium, a current upper limit on the mass of the electron neutrino of 2 eV/c^2 has been established using this method[10] [73].

Similar kinematic measurements have set limits for the muon neutrino mass from the muon spectrum resulting from pion decay at rest yielding $m_{\nu_\mu} < 170$ keV/c^2, and for the tau neutrino mass from tau decays yielding, $m_{\nu_\tau} < 18.2$ MeV/c^2 [74] [75]. The largest planned direct ν_e mass experiments are KATRIN using tritium [76] and MARE [77] which will use ^{187}Re. Both experiments expect to reach a sensitivity of 0.2 eV/c^2 by 2015.

There are currently no direct mass limits on $\overline{\nu}_\mu$ and $\overline{\nu}_\tau$ masses.

- **Neutrinoless Double Beta Decay**

  Normal double beta decay occurs when two electrons and two antineutrinos are emitted by the nucleus of an atom.

$$(Z, A) \rightarrow (Z + 2, A) + 2e^- + 2\overline{\nu}_e. \tag{2.5.5}$$

  This process conserves lepton number with ΔL = 0, since electrons have lepton number L = 1 and antineutrinos have L = -1. Normal double beta decay has been observed in nine isotopes with long half lives (from $\sim 10^{20}$ - 10^{25} years).

  Should the neutrino be it's own anti-particle (i.e. should it be a Majorana fermion), the neutrinoless double beta decay reaction,

$$(Z, A) \rightarrow (Z + 2, A) + 2e^-, \tag{2.5.6}$$

  is possible and observation of this reaction would indicate a non-zero neutrino mass. The decay rate of Equation 2.5.7 is dependent upon the neutrino mass and can be used to set mass limits. There has been one unconfirmed claim of observation of $0\nu\beta\beta$ decay in ^{76}Ge (KKDC) [78] which set a limit on the effective neutrino mass of 100-900 meV at 99.73% confidence level. Until the next generation $0\nu\beta\beta$ experiments come online

---

[10] Interpretation of these results is complicated by the fact that the measured neutrino mass-squared from the fits of the spectrum end point have yielded negative (and therefore unphysical) values.

(GERDA [79], CUORE [80], Majorana [81] and EXO [82]), there is only one running experiment, CUORICINO [83], which is capable of confirming (but not disproving) the KKDC result.

- **Astrophysical Bounds on Neutrino Mass**

  Finally, it should be noted that one can obtain a limit of neutrino mass from cosmological considerations. Such limits are all highly model and data set dependent[11] and derive from the fact that deviations in the CMB temperature and angular distributions are influenced by massive particles such as neutrinos. By knowing the neutrino number density ($\approx 113cm^{-3}$) and energy density (Ω_ν) the total neutrino mass (M_ν) can be obtained from:

  $$\Omega_\nu h^2 = \frac{M_\nu}{94eV}$$

  where h is the Hubble parameter [84]. Recent results from CMB experiments and galaxy redshift surveys give an upper limit of $\sim$ 1 eV/c^2 for M_ν [85]. Neutrinos heavier than this limit would lead to galaxies being less clumped than actually observed. With improved precision and new techniques (weak gravitational lensing and CMB lensing), ambitions claims have been made that with future CMB measurements from the Planck satellite, a sensitivity as low as $M_\nu \sim 0.05\text{eV}/c^2$ could be reached [86].

2.5.3 Supernovae Neutrinos

As already stated, core-collapse supernovae are a primary source of neutrinos. Supernovae neutrinos are in fact the most luminous source of neutrinos in the universe [87]. These stellar explosions produce about 3×10^{53} ergs in neutrinos within a few seconds.

Average core collapse supernovae neutrino energies are about 12 MeV for ν_e, 15 MeV for $\overline{\nu_e}$, and 18 MeV for all other flavors. The neutrinos are emitted over a total timescale of tens of seconds, with about half emitted during the first 1-2 seconds. A detailed description of supernovae types, spectra and light curves is provided in [88].

---

[11] WMAP, BOOMERanG, Acbar, CBI, VSA, etc...

In 1987, about twenty supernova neutrinos were detected for the first time from SN 1987A in the Large Magellanic Cloud [90] [91] [89]. Detection of these neutrinos provided a rough confirmation of the picture of stellar core collapse and neutron star formation in that the number of measured electron neutrinos and their total energy were in rough agreement with theoretical expectations. Although the neutrino data from SN1987A set limits on the neutrino lifetime, charge, number of neutrino families, neutrino magnetic moment, axions, and even extra dimensions, the SN1987A detected events were not sufficient to provide tight constraints on the dynamics of supernova explosions. However, detection of neutrinos from a Galactic supernova, which are estimated to occur about once every 30-50 years and are expected to produce around 10,000 neutrino events in a detector like Super-Kamiokande, could yield extremely valuable information concerning the details of the supernova explosion mechanism such as [92]:

- detection of the high-luminosity ν_e's would confirm the theoretical concepts of core bounce, shock formation and shock break-out.
- Also, a detailed measurement of ν_e and $\overline{\nu}_e$ fluxes with time would probe the density profile of the progenitor star as well as the dynamics. For example, the onset of the explosion should be well delineated by a significant reduction in ν_e and $\overline{\nu}_e$ luminosities. Spectral information could reveal neutrino heating conditions which produce the delayed explosion.
- Detection of ν_μ and ν_τ would provide valuable information on the thermal structure of the neutron star surface layers and neutrino transport and interactions as well as the binding energy release during neutron star formation.
- Neutrino flavor transformation matter effects during the outward propagating shock should imprint time-dependent features on the spectra of supernova neutrinos and may manifest themselves as an anomalously hot ν_e spectrum.

In addition to better understanding the physics of supernovae themselves, there is other interesting physics associated with the study of supernova neutrinos. For instance, several scenarios exist for black hole formation following supernova explosions [93]. A supernova that continues its collapse to a black hole would be distinctly signaled by a sharp cutoff in neutrino luminosity in all flavors.

2.5.4 The Diffuse Supernova Neutrino Background (DSNB)

Instead of waiting for an individual supernova in our galaxy to study Supernova neutrinos, it has been suggested that the superposition of neutrino fluxes from *all* supernovae in the universe could be detected [94] [95] [96]. This is the Diffuse Supernova Neutrino Background (DSNB). The DSNB flux is dependent on the neutrino spectrum emitted from each supernova explosion and the cosmic Star Formation Rate (SFR). In fact, because supernova explosions have occurred in both the past and continue in the present, the DSNB can provide model dependent information concerning the SFR at both high and low redshifts. In addition, fundamental neutrino properties such as possible neutrino decay and lifetime could be constrained [97].

Although the DSNB includes all neutrino flavors, the best current limit has been achieved in the $\overline{\nu}_e$ channel via the inverse beta decay reaction on free protons at Super-Kamiokande. They determined an upper limit of 2.8-3.5 events per year above the triggering threshold of 5 MeV, depending on different DSNB theoretical models. In addition, SK found an upper limit of 20-130 $\overline{\nu}_e$ cm^{-2} s^{-1} for the total DSNB and an upper limit on the DSNB flux of 1.2 $\overline{\nu}_e$ cm^{-2} s^{-1} above 19.3 MeV [97]. This result was close to most predictions and suggested that the DSNB might be detectable with a suitably designed detector.

However, because of the very low flux, DSNB detection experiments will be background-dominated and will require a very large liquid-scintillator or water Cherenkov detector. Most likely the detection will use the inverse beta decay reaction [22] [97] [98].

In reference [99], - prompting much of the work of this thesis, Beacom and Vagins proposed adding 0.2% $GdCl_3$ to the Super-Kamiokande water Cherenkov detector to detect antineutrinos by tagging neutrons following $\overline{\nu}_e + p \rightarrow e^+ + n$. The resulting double coincidence signal (the Cherenkov radiation from the relativistic positron plus the Cherenkov radiation from a delayed relativistic electron Compton-scattered above the Cherenkov threshold by the relatively energetic gammas resulting from neutron capture on the gadolinium) greatly reduce backgrounds.

However, neutrons from other sources could mimic this coincidence reaction and act as background. Sources of low-energy $\overline{\nu}_e$ can come from reactors and/or geo-neutrinos. In addition, neutral current reactions of atmospheric neutrinos can produce background neutrons. However, as pointed out in [99] the spallation neutron backgrounds can be rejected by requiring very small time separation between the positron and neutron events and reduced neutron rates from background sources.[12] Beacom and Vagins estimate that backgrounds from cosmic rays, notably muon-induced spallation and muon-decay electrons, can be reduced by a factor of ~ 5 with the addition of $GdCl_3$.

Figure 2.5, which is taken from [99] shows a range of DSNB spectra. While the DSNB cannot be detected currently with SK, the addition of $GdCl_3$ might sufficiently reduce backgrounds such that the DSNB would become visible at energies between about 10 and 20 MeV.

---

[12] Beacom and Vagins quote neutron rates of one per day from reactor $\overline{\nu}_e$, about 4 per day from U/Th decay, about 2 per day from atmospheric neutrinos and about one per day from ^{152}Gd for the Super-Kamiokande detector.

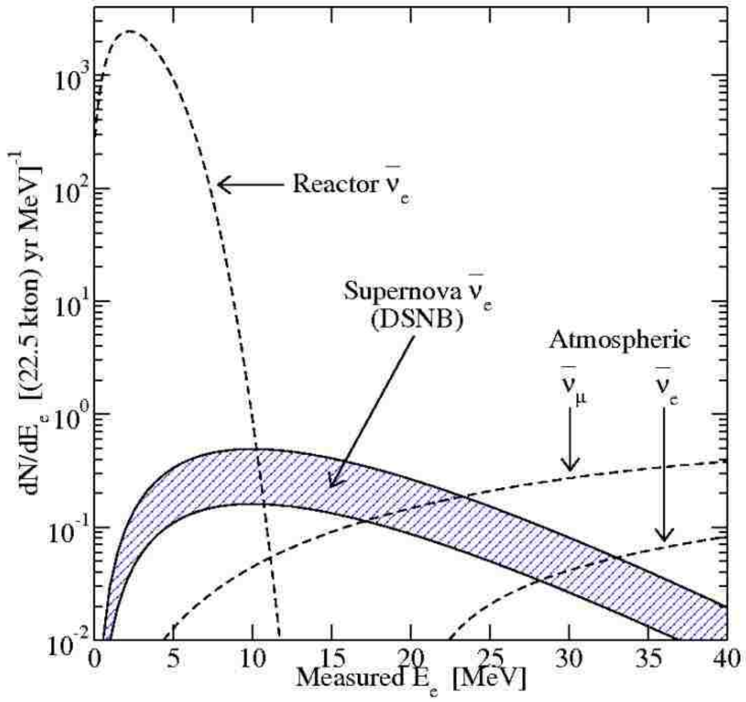

Figure 2.5: The range of DSNB spectra and potential backgrounds shown for the Super-Kamiokande (SK) site. The upper edge of the hatched band is set by the SK limit and the lower edge by modern DSNB models. This figure indicates the potential window between 10 - 20 MeV for which the addition of $GdCl_3$ to the SK water Cherenkov detector could make DSNB detection possible.

Chapter 3

Neutrino Detection Processes and $GdCl_3$

The perfect neutrino detector would: a) collect as many neutrino events as possible; b) provide event-by-event timing resolution; c) accurately determine the neutrino energy spectrum; d) mark the original neutrino interaction point of origin and e) tag each interaction by neutrino flavor for all neutrino flavors [100]. There are no perfect neutrino detectors. Instead, the design of each detector is optimized for the specific physics which one wishes to explore. In this chapter, a brief general overview of neutrino/antineutrino detection processes is presented and then two types of detectors for detecting MeV range antineutrinos are discussed in greater detail. To conclude the chapter, the advantages and potential disadvantages of doping water with $GdCl_3$ in water Cherenkov detectors are introduced and discussed.

3.1 The Neutrino Detection Processes

In all neutrino detectors, neutrinos interact with the individual target atoms in the detector and one seeks signals that a neutrino has interacted with the target atoms. For neutrinos in the MeV energy range, typical reactions are 2-body → 2-body [101]: There are "charged-current" reactions:

$$\nu_e + (A, Z) \rightarrow e^- + (A, Z+1) \tag{3.1.1}$$

$$\overline{\nu_e} + (A, Z) \rightarrow e^+ + (A, Z-1) \tag{3.1.2}$$

and "neutral-current" reactions:

$$\nu + (A, Z) \rightarrow \nu + (A, Z) \tag{3.1.3}$$

$$\overline{\nu} + (A, Z) \rightarrow \overline{\nu} + (A, Z) \tag{3.1.4}$$

where (A,Z) denotes a nucleus with Z protons and A-Z neutrons. There is also elastic neutrino scattering:

$$\overset{(-)}{\nu}_e + e^- \xrightarrow{W,Z} \overset{(-)}{\nu}_e + e^- \tag{3.1.5}$$

$$\nu_i + e^- \xrightarrow{Z} \nu_i + e^- \tag{3.1.6}$$

where $\xrightarrow{W,Z}$ denotes which vector bosons are involved and $i = \mu{,}\tau$.

The workhorse detection mechanism of MeV energy reactor experiments has been the Charged Current (CC) inverse beta decay reaction on a proton:

$$\bar{\nu}_e + p \xrightarrow{W} n + e^+. \tag{3.1.7}$$

The primary advantage to the use of this reaction is that it dominates other reactions in any detector in this energy region. Reaction 3.1.7 produces almost isotropically distributed positrons ($E_{e^+} = E_{\overline{\nu}} - \Delta m; \Delta m = m_n - m_p$). Of course, charged current interactions occur for bound nucleons as well. For these interactions, large uncertainties can often be involved due to the nuclear physics although, here too, a charged lepton is usually observable [100]. As indicated by reactions 3.1.3 and 3.1.4, the character of the Neutral Current (NC) interactions are that they are flavor-blind. Also, several NC interactions on nuclei have cross-sections that yield reasonable rates. Of these some also include a tag via ejected nucleons or de-excitation γ's. As examples, a 15.5 MeV de-excitation γ tags the NC excitation of ^{12}C*, ν_x + ^{12}C $\rightarrow$ ν_x+ ^{12}C* and a cascade of 5-10 MeV de-excitation γ's can tag ν_x + ^{16}O $\rightarrow$ ν_x+ ^{12}O* in a water Cherenkov detector [102]. In addition, NC coherent neutrino-nucleus scattering, $\nu + A \rightarrow \nu + A$, occurs at higher rates than νp scattering. However, because the targets are heavy, recoil energies are much smaller - tens of keV. Detectors using these reactions are currently in development for WIMP detection [103].

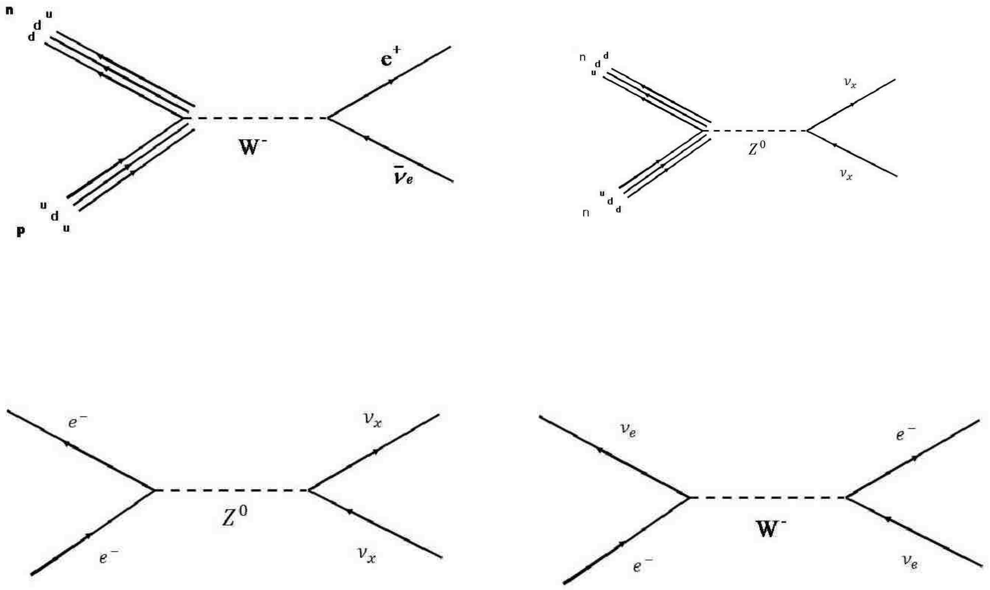

Figure 3.1: Top: First order Feynman diagrams for neutrino nucleon interactions. The interaction on the top left shows inverse beta decay $\nu_e + n \rightarrow e + p$. The spectator quarks are also shown. The neutral current interaction on the right applies to all quarks and neutrino flavors. Bottom: First order Feynman diagrams for ν-e scattering. All neutrino flavors scatter via the neutral current reaction (left) while only the electron neutrino can interact through a charged current interaction with an electron (right). The time arrow runs from the bottom of the figure to the top.

As per reactions 3.1.5 and 3.1.6, elastic neutrino-electron scattering (ES) occurs via both CC and Neutral Current (NC) reactions. Although the ES reaction has a cross section of just a few percent of that for the inverse beta decay rate [100], an advantage of ES is that the neutrino energy can be more accurately measured from the measured energy of the recoil electron. This allows detectors to perform neutrino spectroscopy and disentangle different neutrino flux contributions. Another distinct advantage of ES is that it is directional and can be used, for example, in supernova pointing [104] or to reject isotropic background events.

Figure 3.1 shows the Feynman diagrams of the neutrino interactions described above [105].

3.2 Water Cherenkov Detectors

As discussed in Chapter 1, many detector designs have been proposed and used for detecting neutrinos. Different experimental designs have different advantages and disadvantages. The primary considerations are: (i) target mass; (ii) location; (iii) high material radio-purity; (iv) optimized detection efficiency for the physics of interest; and (v) incorporation of a characteristic signal tag to enhance background rejection. A brief listing of common types of detectors is provided below:

- Liquid Argon: Liquid Argon is the detecting medium. Charged particle tracks are identified in the liquid based on the pattern of ionization produced by the tracks. This type of detector has good calorimetry and particle identification capability.
- Iron Calorimeter: Iron modules are interspersed with active detector elements in which charged particles deposit energy. These detectors are primarily used for observing ν_μ and $\overline{\nu_\mu}$ interactions at high energies.
- Emulsion: Emulsion films are primarily employed to observe the trajectories of τ and the products of its decay. These films are interleaved with (thick) lead plates to provide large target mass.
- Radio-chemical: Radio chemical experiments were proposed by Bruno Pontecorvo [106] as early as 1946 and played a critical role in uncovering the solar neutrino problem. These are based on neutrino capture reactions, $\nu_e + {}^{A}_{Z}\mathrm{Y} \rightarrow {}^{A}_{Z+1}\mathrm{Y} + e^-$ and the subsequent decay of the nuclide ${}^{A}_{Z+1}\mathrm{Y}$ back to the stable ${}^{A}_{Z}\mathrm{Y}$. Chemical extraction of the produced nuclei is accomplished periodically to measure the decay activity and yield the number of neutrino interactions at the time of extraction.
- Scintillation Detectors: The oldest and perhaps most commonly used neutrino detectors are scintillator detectors [109]. Scintillation is the result of ionization energy loss occurring when charged particles traveling through a medium (solid, liquid or gas)

excite molecules along their path. The resulting de-excitation emits light that is isotropic and delayed with respect to the passage of the particle. Many different types of materials scintillate. These materials include non-organic crystals (NaI, CsI, BGO), organic crystals (Anthracene), organic plastics and organic liquids.

This section and much of this thesis addresses one specific type of detector, the water Cherenkov detector. Cherenkov radiation is the coherent emission of light by a charged particle moving through an dielectric medium at superluminal velocities. The velocity of light in a medium is characterized by the index of refraction, n, of that medium: $\mathrm{c}_n = \mathrm{c}/n$. Charged particles that move faster than c_n (the Cherenkov threshold) create a photonic shock-wave analogous to the sonic boom caused by supersonic particles. The wavefront of this shock is conical and emitted with a characteristic opening angle θ_C defined by

$$\cos\theta_C = \frac{1}{\beta n(\lambda)} \tag{3.2.8}$$

where β is the relativistic velocity v/c and n(λ) shows the explicit dependence of the refractive index on the wavelength of the emitted light.

The conical shock-wave travels as shown in Figure 3.2 with θ_C decreasing as the particles velocity decreases until it drops below Cherenkov threshold. The disturbance is normally detected as a ring (the cross section of a cone) on the detector. For a particle of charge Ze moving above threshold, the number of photons emitted per unit wavelength per unit path length is

$$\frac{d^2N}{d\lambda dx} = \frac{2\pi\alpha Z^2}{\lambda^2}\sin^2\theta_C \tag{3.2.9}$$

where α is the fine structure constant ($2\pi e^2/hc$) [111]. Note that this equation indicates that for a given charge, equal numbers of photons are created per centimeter path length. In other words, particles with greater energy - and thus longer path lengths - generate more light than lower energy particles. For fully contained events this can be used to measure the energy of an event.

The relativistic energy formula provides the minimum kinetic energy, KE_{min}, required for a particle's velocity, v, to exceed the speed of light in a material. It is:

$$KE_{min} = mc^2 \left(\sqrt{\frac{1}{1 - v^2/c^2}} - 1. \right) \tag{3.2.10}$$

where $v = c/n$ can be substituted to establish the condition for the minimum kinetic energy. KE_{min} for e$^-$,μ^+, p^+, and ^{16}O are given in Table 3.1.

Table 3.1: Several particles and their respective Cherenkov light production threshold in water (n=1.33).

Particle	**KE$_{min}$ (MeV)**
e$^-$	0.263
μ^+	53.23
p$^+$	480.3
^{16}**O**	7626

Typically, the charged particles are accelerated above the Cherenkov threshold either directly (the product positron of the inverse beta decay reaction is an example) or via scattering processes such as Compton scattered electrons. In this second case, it should be noted that while Table 3.1 gives the Compton thresholds for electrons as 263 keV in water (n = 1.332) the scattering γ-ray must possess an energy in excess of this energy which can be calculated as follows:

$$E_\gamma = E_e + E_\gamma^{'} + \phi \tag{3.2.11}$$

where E_e is the energy of the Compton electron, $E_\gamma^{'}$ is the energy of the Compton scattered photon given by:

$$E_\gamma^{'} = \frac{E_\gamma}{1 + (E_\gamma/0.511MeV)(1 - \cos\theta)} \tag{3.2.12}$$

and ϕ is the electron binding energy.

In Equations. 3.2.11 and 3.2.12, the binding energy, ϕ can be neglected Thus, for $\theta = 180^o$ (complete back-scattering)

$$E_\gamma = E_e + \frac{E_\gamma}{1 + 2(E_\gamma/0.511MeV)}. \tag{3.2.13}$$

Therefore, $E_\gamma = 0.422$ MeV is the threshold γ-ray required for the production of Cherenkov radiation in water.

The number of photons emitted by a Cherenkov detector is generally much fewer than that emitted from equivalent energy loss in a good scintillator. For a 1 MeV electron only a few hundred photons may be emitted. Notwithstanding this fact, like scintillator detectors, water Cherenkov detectors have been in use in neutrino detection for many years. To date, their primary application has been as inexpensive detectors of neutrino-electron interactions and in proton decay experiments. Examples of water Cherenkov detector experiments are IMB, Super-Kamiokande, SNO and as a veto for KamLAND and Borexino.

- **Relevant Wavelengths**

Before proceeding further, there is an important point to consider regarding the use of photomultiplier tubes (PMTs) for detection of Cherenkov light. Typically, PMTs are made of borosilicate glass. As indicated in Figure 3.3, the UV region of the electromagnetic spectrum is poorly suited to these types of PMTs since the number of photons emitted per unit wavelength per unit path length varies as $1/\lambda^2$. The result is that Cherenkov radiation emits more photons at smaller wavelengths and therefore the greater part of Cherenkov photons are emitted in the ultraviolet range. The reduced transparency of borosilicate glass to UV radiation combined with the poor photon yield of Cherenkov detectors compared to that of scintillator detectors suggests that attaining and maintaining water purity and transparency at UV wavelengths is a critical feature to the proper operation of water Cherenkov detectors.

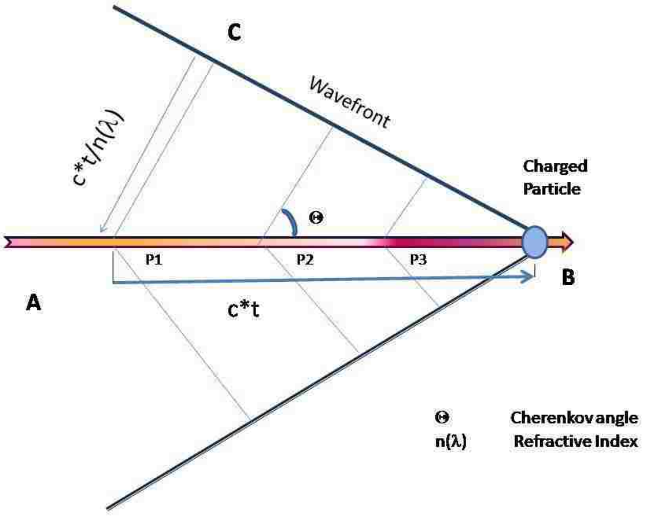

Figure 3.2: If a charged particle's velocity, cβ, exceeds the velocity of light in the medium, a 'Mach cone' is created. Huygens wavelets emitted from each point in time, $P1$, $P2$, $P3$ add up constructively along a line defined by the Cherenkov angle Θ.

3.3 Gd-Doped Water Cherenkov Detectors

Considering this sensitivity to transparency, one might wonder why water Cherenkov detectors should be considered at all as neutrino detectors. The reasons are several. First, water Cherenkov detectors are much less expensive per unit volume than scintillator detectors and therefore can be constructed of much larger size. Second, there are significantly reduced material handling and hazard control considerations required compared even to solid scintillator detectors. Also, from a physics perspective, one important advantage of water Cherenkov detectors over scintillator detectors is that water Cherenkov detectors lack two important backgrounds that scintillator detectors generally possess. First, since the energy threshold for proton recoils in water is ≈1.5 GeV, muon produced neutrons do not induce significant backgrounds. This is also true for relatively low energy cosmic secondary hadronic interactions in water. Only very high energy hadrons will induce a background.

More central to this thesis, an important downside to Cherenkov detectors compared to scintillator detectors has been the inability of the water Cherenkov detectors to detect the absorption of thermal neutrons. Neutrons capturing on protons in light water emit a characteristic 2.2 MeV gamma ray from the reaction $n+p \rightarrow d+\gamma$. Since the gamma energy is typically spread over several electrons, the Compton scattered electrons are close to the Cherenkov threshold and only a small amount of detectable light is emitted. As an example of the difficulty for neutron detection, in the Super-Kamiokande water Cherenkov detector, simulations show that only a few photo-tubes would be hit - making detection essentially impossible against the background of roughly three hits expected from dark noise in a 50 ns time window. The result is that light water detectors like Super-Kamiokande can not distinguish between neutrino interactions and antineutrino interactions.

To overcome this problem, the addition of solutes to the water have been proposed [99] [110] [112] [113] to introduce new charge-current channels for the detection of ν's and as neutrophage targets for detection of neutrons following the charged current inverse beta decay reaction. *To use water Cherenkov detectors for the detection of antineutrinos, some method to detect neutrons in water is required.*

3.3.1 Proposed Dopants to Improve Water Cherenkov Neutrino and Antineutrino Detection

In the first category (i.e. dopants for improving water Cherenkov detector sensitivity to neutrinos) were proposals [113] for the detection of ν's using the reaction $^7\mathrm{Li}+\nu_e \rightarrow e^- + ^7\mathrm{Be}$ in lithium-bearing solutes. Several of these (e.g. LiCl) are soluble. The advantage to this reaction is it's low reaction threshold ($\sim$ 0.8 MeV) but unfortunately, LiCl was found to have severe light attenuation problems at high concentrations ($\sim$ 30%) and work with this compound was abandoned before the light attenuation at lower concentrations could be measured.

Another proposed solute serving as a new charge-current channel for ν detection is $^{11}\mathrm{B}$ through the reaction $^{11}\mathrm{B} + \nu_e \rightarrow e^- + ^{11}\mathrm{C}$ which has a threshold of 1.982 MeV. This target was proposed in [114] with the solute H_3BO_3 for use in a predecessor experiment to the Borexino liquid scintillator experiment.

With regard to the second category, as early as 1969, experiments [110] showed that NaCl and $Cd(NO_3)_2$ dissolved in water increased the number of neutrons recorded in a water Cherenkov detector.

Other potential neutrophage candidates are ^{10}B and ^{6}Li since both of these nuclei have high thermal neutron cross sections (3837b and 940.3b respectively). In fact, neutron absorption cross section experiments were performed as early as 1954 for Boron salts dissolved in water [115]. Unfortunately, of these two solutes, only Boron produces a de-excitation gamma and its energy is only 0.48 MeV. Such a low energy is not useful for a water Cherenkov detector. [1]

Another potential neutrophage chemical in water is Chlorine. During the "Salt" phase of SNO, 2 tons of NaCl were added to the heavy water, D_2O, to increase detector sensitivity to the neutral current reaction $\nu_x + D \rightarrow \nu_x + p + n$ via neutron capture on ^{35}Cl. This increased the neutron detection efficiency by about a factor of three compared to pure heavy water [118] via an energetic gamma cascade with a total energy of 8.6 MeV released upon the de-excitation of ^{36}Cl. In addition, it is known that NaCl in even large concentrations ($\sim$ 10%) does not significantly affect water transparency at visible wavelengths [119].

Chlorine has a neutron cross section of about 44 barns. This is over 100 times the neutron cross section of hydrogen. Although this increases the neutron capture efficiency to 40-50%, a quick calculation indicates that it would take $3 \times M_{water}/50$ where M_{water} is the mass of the water in the detector to get 50% of the neutrons to capture on the Cl [120]. This equates to about 6 % NaCl by weight, an amount which is clearly impractical except for small detectors.

3.3.2 Gadolinium as a Dopant

In recent years, gadolinium has become inexpensive to obtain ($\sim$ \$10 per kilogram) in the form of the compound gadolinium trichloride, $GdCl_3$, which is used as a contrasting agent

---

[1] It should be noted that the use of ^{10}B and ^{6}Li in liquid scintillators to increase the direction measurement of antineutrinos has been proposed [116] and that ^{6}Li loaded to 0.15% in 600 l of organic scintillator in the Bugey experiment [117] was used to absorb neutrons to yield ^{3}He and ^{4}He. The He scintillation signal was subsequently extracted with Pulse Shape Discrimination analysis.

for medical NMR scans [121]. Unlike many rare earth compounds, $GdCl_3$ is non-toxic [122] [123] and highly soluble in water [124].

The Gd isotopes each have different cross-sections (shown in Table 3.2 along with the associated natural abundances and half-lives). The most efficient isotope at capturing neutrons is ^{157}Gd which has a cross-section of σ = 192,000 b, followed by ^{155}Gd which has σ = 45,500 b. For natural Gd, the cross section for thermal neutron capture is $\approx$ 49,100 barns. Because of their short lifetimes, the ^{153}Gd, ^{159}Gd, ^{161}Gd, and ^{162}Gd isotopes are not present in natural Gadolinium. For comparison, the thermal cross section for hydrogen is 0.33 b.

Table 3.2: Properties of the Gadolinium isotopes. Cross sections are taken from the BNL nuclear data base [127].

Isotope	**Nat. Abund. (%)**	**$t_{1/2}$**	**Thermal Neutron Capture (b)**
^{152}**Gd**	0.2	1.08 $\times 10^{14}$ y	934
^{153}**Gd**	-	241.6 d	$\approx$ 50000
^{154}**Gd**	2.18	∞	75
^{155}**Gd**	14.8	∞	45500
^{156}**Gd**	20.47	∞	1.9
^{157}**Gd**	15.65	∞	192000
^{158}**Gd**	24.84	∞	2.2
^{159}**Gd**	-	18.48 hrs	$\approx$ 200
^{160}**Gd**	21.86	∞	0.7
^{161}**Gd**	-	3.66 m	
^{162}**Gd**	-	8.4m	

Neutrons in water produced during the inverse beta reaction are thermalized in a few microseconds after about 12 collisions with the water's free protons. Additionally, using σ = 49100 barns and

$$\frac{1}{\lambda_{total}} = \frac{1}{\lambda_H} + \frac{1}{\lambda_{Gd}} = n_H \sigma_H + n_{Gd} \sigma_{Gd} \tag{3.3.14}$$

at 0.2% $GdCl_3$ by weight, capture on Gd is about 90% and λ = 4cm where λ is the mean free path. Thus because of its high cross section, even at low concentrations ($\sim$ 0.2% by weight) neutron capture can be dominated by gadolinium (Figure 3.4).

The absorption of thermal neutrons on gadolinium is described via the reaction: $^{155(157)}$Gd + n $\rightarrow$ $^{155(157)}$Gd* $\rightarrow$ $^{156(158)}$Gd+γ's where Gd* is the excited state of the Gd nucleus. The

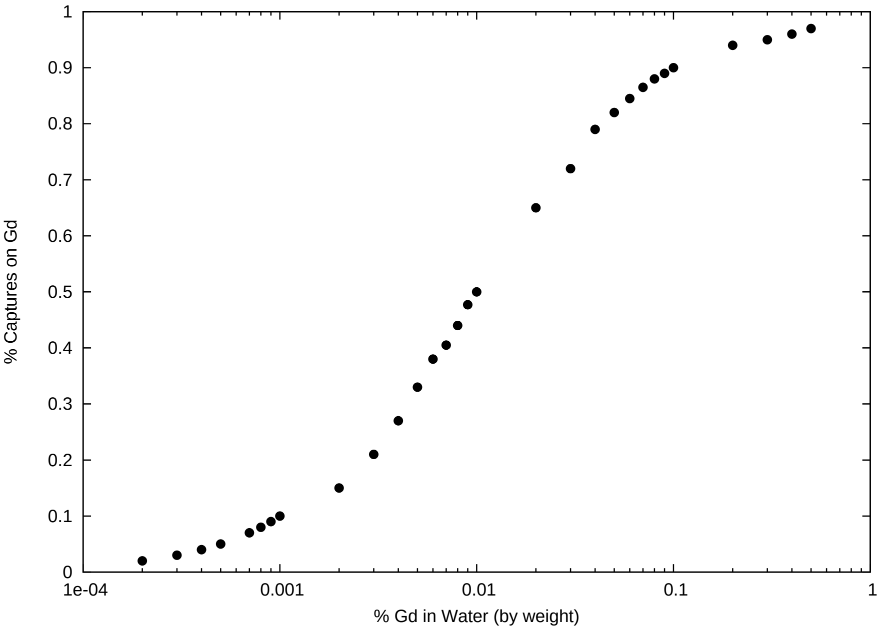

Figure 3.4: The fraction of captures on Gd compared to increased Gd concentration.

neutron binding energy of ^{156}Gd is 8.53 MeV while for ^{158}Gd it is 7.93 MeV. Neutron capture is followed by the emission on average of 3 to 4 gammas with a summed energy of $\sim$ 8 MeV. In a Cherenkov detector, these captures are detected via the Compton scattering process whereby the gamma from the neutron capture event scatters off the nearly free electrons inside the water detector and accelerates these electrons above the Cherenkov threshold.

In consideration of the above, several past and current reactor experiments (Chooz, Palo-Verde, Double-Chooz and Daya-Bay) have used or are using gadolinium as a solvent in liquid scintillator. For example, Gd-loaded scintillator is used in the SONGS reactor monitoring scintillator detector that will be discussed in Chapter 5 and in the KARMEN short-baseline accelerator experiment. Since liquid scintillators are made of aromatic organic solvents, it is difficult to add inorganic salts of Gd into the organic liquid scintillator. The only solution to this problem is to form organometallic complexes of Gd with organic ligands that are soluble in the organic liquid scintillator. The different experiments have used different methods to solve this problem with varying success [2] [126].

---

[2] It should be noted that organic liquid scintillators containing gadolinium are commercially available (e.g. [125]).

In 2004, Beacom and Vagins [99] specifically proposed the use of $GdCl_3$ in the Super-Kamiokande water Cherenkov detector. The physics potential of a Super-Kamiokande-sized detector sensitive to antineutrinos from relic supernovae, galactic supernovae, as well as terrestrial, reactor, solar and accelerator neutrinos was immediately recognized and it was Beacom and Vagin's proposal which provided the impetus for much of the work in this thesis. The potential application of neutron-absorbing materials in water Cherenkov detectors for possible nuclear security applications was the other prime motivator for this thesis. But before either of these two potential applications can be investigated, the effects on detector components of adding $GdCl_3$ to water must be determined. The first tests performed addressed material compatibility. In these tests materials were soaked in a $GdCl_3$ water solution. The results are described in the following section.

3.3.3 Long-Term Soak Testing of Water Cherenkov Detector Materials in a 2% $GdCl_3$ Aqueous Solution

Although the advantages of using Gd are potentially great, the introduction of Gd^{+3} and Cl^{-} ions to a water Cherenkov detector could create deleterious effects. For example, the added ions could react with other detector materials or the electronics, and photomultiplier tubes. Potential problems are increased galvanic corrosion, surface pitting, stress-induced cracking, and chemical reactivity.

In an effort to answer these questions, materials typical of water Cherenkov detectors (specifically, materials used in the Super-Kamiokande detector) were soaked at room temperature in a 2% solution of $GdCl_3$ - about ten times the concentration required for 90% capture on Gd - to accelerate corrosion processes associated with ion concentration.

In addition to the $GdCl_3$ soak sample, every material was also soaked in a control solution of deionized water from the same source used to make the $GdCl_3$ sample solution. Thus each sample could be compared with a sample soaked under identical conditions but without $GdCl_3$. Both samples were then tested with an Hitachi S-3600N variable pressure Scanning Electron Microscope (SEM) or by visual inspection and/or mechanical strength testing.

Testing on the stainless steel components was of particular interest since it is one of the most commonly used water Cherenkov detector materials. Since the Super-Kamiokande detector stainless steel is almost exclusively series 304 (18-25% Cr, 8-20% Ni and low carbon) only this type of steel was tested.

Stainless steel metals are subject to "oxygen pitting" whereby oxygen in water preferentially attacks an area of surface metal already damaged in some way. Although the water in most water Cherenkov detectors is de-oxygenated to make pitting less of a problem, the samples tested were not de-oxygenated in order to provide a more conservative examination.

Stress Cracking Corrosion (SCC) is another type of corrosion which occurs in stainless steels. It occurs at grain boundaries under tensile stress and propagates along both intergranular or trans-granular paths. This type of corrosion is of primary importance since it occurs when 300 series stainless steel is exposed to tensile stress in a corrosive environment.

Some materials (plastic, fiber-reinforced-plastic, rubber and glass) did not lend themselves to SEM scanning. For these materials, visual inspection of the $GdCl_3$ soaked samples and the pure water samples for discoloration, evidence of chemical deterioration, cracking and pitting, and precipitates was performed.

In addition, for plastic materials, a mechanical strength test was performed as a test of chemical changes. In this test, a uniform thin strip of the material roughly 2 mm in width was clamped hanging vertically. A series of weights were then added in 100 g increments until the strip broke allowing before/after comparison.

A complete description of the samples, test procedures, an SEM library of every metal sample at ×100, ×400, and ×1000 magnificaation and results of all materials testing can be found in [128]. With few exceptions, almost all the materials tested showed no effect from exposure to 2% $GdCl_3$ over this period by visible inspection. A representative sub-sample of steel components was imaged by SEM for direct comparison of surfaces. While no $GdCl_3$ related deterioration was seen in these images, the images of the water soak tank steel and PMT steel frame did show more general corrosion effects than those of the $GdCl_3$ sample which was unrelated to soak damage. Some of the steel samples also showed some tendency for water discoloration to be higher in the $GdCl_3$ soak samples than the water soak samples but this was not considered a serious problem since the amount of discoloration was very small and the surface to volume ratio in the sample jar was many times that of typical detectors.

No part of the PMT materials tested (glass, plastic base cover, cable) showed signs of deterioration, water discoloration, pitting, or cracking due to $GdCl_3$. Thus the PMTs seem to be in no danger from concentrations as high as 2% over many years.

Only one component showed significant corrosive effects both in water and in the $GdCl_3$ solution. This was the PMT clamping ring buckle and was due to serious corrosion around screw heads (that appeared to be tap welded) and pins that hold the buckle in a cylindrical shape. Although corrosion occurred in pure water, the problem is worse by perhaps a factor of two in the 2% $GdCl_3$ soak sample.

To summarize the results of all testing done at LSU of water Cherenkov detector materials, no component seemed likely to fail mechanically from the addition of 0.2% $GdCl_3$ to a water Cherenkov detector. However, based on visual inspection of water discoloration, there was some indications that some steel samples (detector tank steel used in Super-Kamiokande) added corrosion products to the water slightly faster in 2% and 20% $GdCl_3$ than pure water [128].

3.3.4 The Effect on Transparency from Using $GdCl_3$

While the results of these early material compatibility tests were encouraging, an equally important test of $GdCl_3$'s potential for use in water is it's effect on transparency.

Pure water has a 'transparency window' with attenuation lengths greater than 50 m in the spectral region from about 320 to 480 nm. This is well-matched to the Cherenkov spectrum and the sensitivity of borosilicate photomultiplier tubes.

Unfortunately, water from typical public potable water supplies has a much shorter attenuation length in the UV, often 5-10 meters or less. The reason for this is not well-understood. Nevertheless, standard water purification systems that remove dissolved solids have empirically been found to solve this problem. Thus all operating water Cherenkov neutrino detectors (WCD's) have an associated water treatment plant. This component is normally a significant percentage of the construction expense. In addition, it is found that the water in the detector will deteriorate in transparency - even in a sealed stainless steel or high density polyethylene tank. Thus the water treatment plant must be run continuously to maintain detector water quality and stability and this can be a large part of the operational expense of WCD's.

Experiments were conducted at Lawrence Livermore National Laboratory (LLNL) to determine the effect on light transparency resulting from the addition of $GdCl_3$. The experiment incorporated a long light transmission arm ($\sim$ 20 m) constructed of stainless steel, measurements at multiple wavelengths over several days and using pure, filtered and degassified water. The experimental procedure and results of the LLNL testing are described in the following chapter.

Chapter 4

Transparency Testing of $GdCl_3$-Doped Water in a Stainless Steel Light Transmission Arm

This chapter addresses experiments conducted at Lawrence Livermore National Laboratory (LLNL) to determine the effect on light transparency resulting from the addition of $GdCl_3$.

4.1 Theoretical Background of Light Extinction

Maxwell's equations and experimental constitutive relations are the theoretical starting point for considering light extinction in water. Applied to an infinite, homogeneous, linear, isotropic, magnetic, conductive medium which is free of net electric charge, the Maxwell equations yield the wave equations

$$(\nabla^2 - \frac{4\pi\mu\sigma}{c^2}\frac{\partial}{\partial t} - \frac{\mu\epsilon}{c^2}\frac{\partial^2}{\partial t^2})\psi = 0 \tag{4.1.1}$$

where ψ is a component of the electric field, $\vec{E}$, or the magnetic field intensity, $\vec{H}$, c is the speed of light in a vacuum, μ is the relative magnetic permeability, ϵ is the dielectric function, σ is the electrical conductivity and $\omega = \frac{2\pi c}{\lambda}$ is the angular frequency. The plane wave solutions to Equation 4.1.1 are

$$\vec{E} = \vec{E}\exp[i(\vec{\kappa} \cdot \vec{r} - \omega t)], \tag{4.1.2}$$

$$\vec{H} = c(\vec{\kappa} \times \vec{E})/\mu\omega, \tag{4.1.3}$$

$$\kappa = \frac{\mu\omega^2}{c^2} + i4\pi\frac{\mu\epsilon\omega}{c^2}, \tag{4.1.4}$$

$$\kappa_r = [\frac{\gamma + (\gamma^2 + \delta^2)^{1/2}}{2}]^{1/2}, \tag{4.1.5}$$

$$\kappa_i = [\frac{-\gamma + (\gamma^2 + \delta^2)^{1/2}}{2}]^{1/2}, \tag{4.1.6}$$

$$\gamma = [\omega^2(\mu_r\epsilon_r - \mu_i\epsilon_i) - 4\pi\omega(\mu_i\sigma_r + \mu_r\sigma_i)]/c^2, \tag{4.1.7}$$

$$\delta = [\omega^2(\mu_i\epsilon_r - \mu_r\epsilon_i) - 4\pi\omega(\mu_r\epsilon_r + \mu_i\sigma_i)]/c^2, \tag{4.1.8}$$

where the subscripts r, i denote the real and imaginary parts, respectively. One can define a complex refractive index $N = n + ik$ of a material medium as the ratio of c ($\epsilon = 1$, $\mu = 1$, $\sigma = 0$ for all ω), to the phase velocity $v_p = \frac{\omega}{\kappa}$ in the medium:

$$n + ik = c(\kappa_r + i\kappa_i)/\omega, \tag{4.1.9}$$

The absorption of electromagnetic flux moving in the $+z$ direction from the origin (z_0) is

$$I = I_0\text{exp}[-\alpha_a(z - z_0)], \tag{4.1.10}$$

where $\alpha_a = 2\kappa_i$ and I and I_0 are the radiant intensities at z and z_0.

Absorption and scattering depend on parameters such as chemical composition, size, shape and orientation of the particles, the surrounding medium, the number of particles and the polarization and frequency of the incident beam. The measured attenuation of electromagnetic radiation by water is described by

$$I = I_0\text{exp}[-(\alpha_a + \alpha_s)(z - z_0)] \tag{4.1.11}$$

where α_a is the absorption coefficient of Equation 4.1.10 and α_s is the scattering coefficient which is comprised of the sum of two contributions

$$\alpha_s = \alpha_p + \alpha_m \tag{4.1.12}$$

where α_p is the scattering from microscopic particles and α_m is due to molecular scattering (Rayleigh)[1].

The coefficient α_m for molecular scattering may be calculated by using the Einstein-Smoluchowski equation [131]

$$\alpha(\omega)_m = \frac{kT\beta}{6\pi}\left(\frac{\omega}{c}\right)^4 [\frac{(\epsilon(\omega)-1)(\epsilon(\omega)+2)}{3}]^2 \tag{4.1.13}$$

where k is the Boltzmann constant, T is the absolute temperature, and $\beta = 4.508 \times 10^{-11} cm^2$/dyne is the isothermal compressibility of water.

In the Einstein-Smoluchowski theory, the scattering of light is attributed to fluctuations in the dielectric constant, caused by the random motion of molecules.[2]

Since $\epsilon(\omega) = n^2(\omega)$

$$\alpha(\omega)_m = \frac{kT\beta}{6\pi}\left(\frac{\omega}{c}\right)^4 [\frac{(n^2(\omega)-1)(n^2(\omega)+2)}{3}]^2. \tag{4.1.14}$$

Calculated values for molecular scattering in pure water have been determined by Morel [132] and the values for UV wavelengths are shown in Table 4.1.

Table 4.1: Scattering coefficient for pure water as a function of wavelength.

Wavelength	**Scattering Coeff** $\alpha_m(10^{-4}\text{m}^{-1})$
350	1.035
375	0.768
400	0.581
425	0.447
450	0.349

In the case of solutions, molecular scattering theory is modified to include terms representing concentration fluctuations. Assuming reasonable values for salinity and concentration

---

[1] Strictly speaking, the scattering theory described by Rayleigh applies only to independent scattering particles and can be applied to liquids only with the assumption that the interaction effects between water molecules is negligible [130].

[2] Accordingly, this theory is also known as ‘fluctuation’ theory.

fluctuations, Morel [132] roughly calculated that the scattering in seawater was 1.3 times that of scattering in pure water.

In very pure waters, molecular scattering dominates the particulate scattering which is the α_s term in Equation 4.1.15.

The treatment employed by Mie to describe the scattering due to the perturbation of a plane monochromatic wave by spherical non-absorbing particles is described in [133]. Mie theory is based on the assumption that the scattered light has the same wavelength as the incident light and that the particles are independent and of a size comparable to the wavelength of light. In Mie theory the scattering coefficient, α_p, is given by

$$\alpha_p = \pi r^2 Q(a,m)N, \text{ or}$$

$$\alpha_{ext} = \pi \int_{r_1}^{r_2} r^2 Q(a,m)N(r)\,dr,$$

where a is the size parameter $2\pi\text{r}/\lambda$, r is the particle radius, λ is the wavelength of incident light, m is the particle refractive index, N is the number of particles per unit volume and Q is the scattering efficiency factor defined as the ratio of the scattering cross section to the planar cross sectional area of the particle.

In Rayleigh scattering forward and backward scattering are equally probable while Mie scattering shows predominantly forward scattering. With increasing particle size, Q increases rapidly, passes a maximum for sizes of the same order of the wavelength and tends to a constant value of 2 [133].

In summary, attenuation of the intensity of a collimated, monochromatic beam of light traversing a collection of spherical particles dispersed in an otherwise uniform medium is due to both absorption and scattering. For pure water, Table 4.2 indicates the relative importance of each and Figure 4.1 shows the total attenuation coefficient (α) plotted against wavelength for purified and de-ionized water contained in the 50K ton Super-Kamiokande neutrino detector.

With respect to the specific light attenuation testing required for determining the loss of light transparency resulting from the addition of $GdCl_3$ to water, there are two related

Table 4.2: Pure water absorption and scattering coefficients at 20^o C, a = absorption coefficient (m^{-1}), A = absorption increment due to temperature (m^{-1} C^{-1} and b = scattering coefficient (m^{-1}). The temperature effect below 400 nm are not included in this table but are known to be negligible. [134].

Wavelength	**a**	**A**	**b**
324	0.0191	-	0.0126
328	0.0170	-	0.0120
332	0.0154	-	0.0114
336	0.0134	-	0.0109
340	0.0119	-	0.0104
344	0.0107	-	0.0099
348	0.0096	-	0.0094
352	0.0086	-	0.0090
356	0.0078	-	0.0086
360	0.0071	-	0.0082
364	0.0066	-	0.0078
368	0.0062	-	0.0075
372	0.0058	-	0.0071
376	0.0056	-	0.0068
380	0.0054	-	0.0065
384	0.0053	-	0.0063
388	0.0054	-	0.0060
392	0.0054	-	0.0058
396	0.0055	-	0.0055
400	0.0058	0.0009	0.0053
404	0.0061	0.0014	0.0051
408	0.0065	0.0015	0.0049
412	0.0069	0.0013	0.0047
416	0.0074	0.0015	0.0045
420	0.0079	0.0015	0.0043
424	0.0084	0.0015	0.0042
428	0.0089	0.0015	0.0040

issues. First, most common devices that measure light attenuation do not consider scattering. Because timing information is important in the process of differentiating antineutrino events from background, light which detours from it's original path, changing it's time of flight to the detector, is of limited use for event reconstruction in a large-scale neutrino detector. Second, most common devices measure light attenuation over light paths no larger than a few cm. But the optimal path length for such measurements (assuming an absorption coefficient of approximately 0.02 m^{-1}) is roughly 50 meters. Therefore, most measurements of water

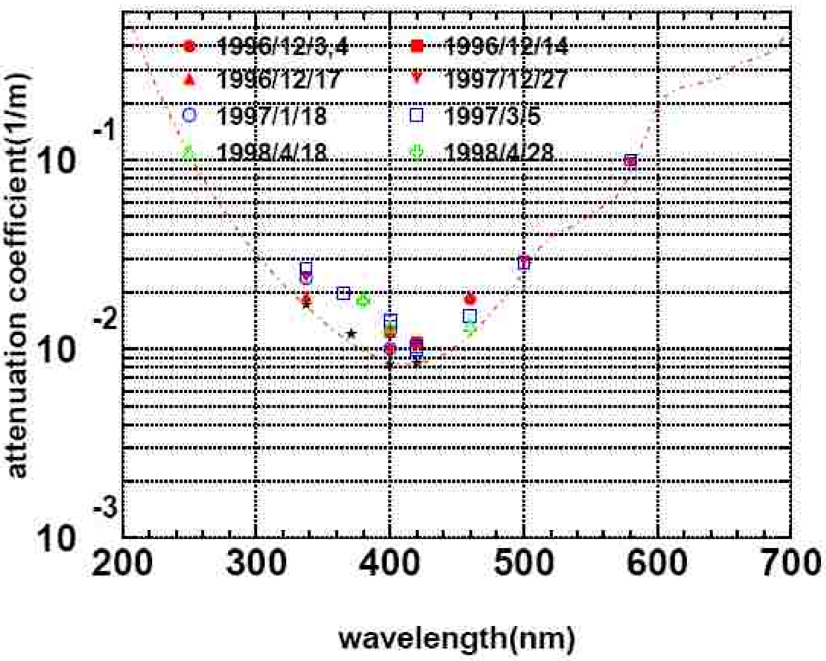

Figure 4.1: Water attenuation coefficient (α) plotted as a function of wavelength together with the prediction model used in the Super-Kamiokande Monte Carlo simulation (dashed-dotted lines) [135]

transparency have been made at transmission lengths three orders of magnitude less than optimum. To get around this fact, an apparatus with a much larger path length is required in order to obtain accurate measurements.

4.2 Experiment Description

4.2.1 Experimental Apparatus

In order to test water transparency and material compatibility of typical detector components upon addition of $GdCl_3$ to pure water, a test facility was designed and built at Lawrence Livermore National Laboratory in Livermore, California. The test facility included a water purification system and mixing tank, a Light Transmission measurement Arm (LTA), a waste storage tank, and a material exposure test tank. Figure 4.2 is a schematic of the complete LLNL Water Cherenkov Transmission Facility (WCTF). The transfer piping was

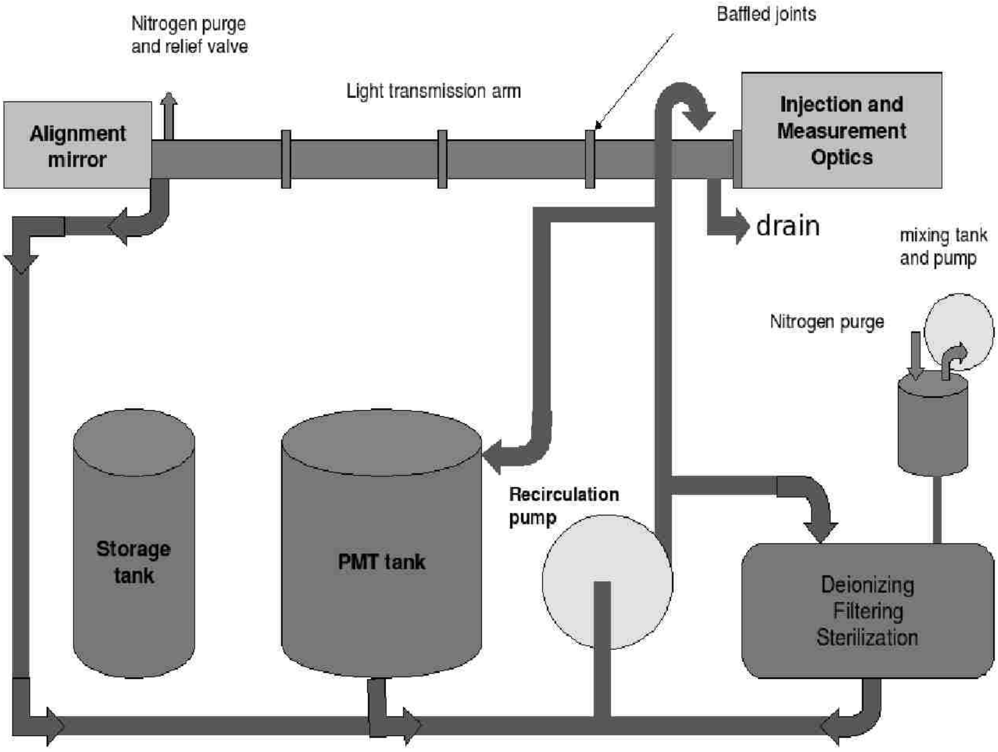

Figure 4.2: The LLNL Water Cherenkov Transmission Facility. The system can produce ultra−pure water and inject $GdCl_3$ via a mixing tank. The water is also circulated through 5 and 0.2 micron filters and an ultraviolet sterilizer to suppress bacterial growth. The water system services both the light transmission arm and the materials test tank, containing two 50 cm diameter PMTs on loan from Super-Kamiokande.

either polypropylene or 1.27 cm diameter 304L grade stainless steel. This piping was used to fill the LTA (Figure 4.3) which was a 9.6 m long, 20.3 cm diameter 304L stainless steel pipe filled with pure or doped water. During the process of mixing the $GdCl_3$, nitrogen gas is bubbled through the mixing tank to reduce the dissolved oxygen content in the system.

Our system included a water purification system that was capable of providing Type I high purity water (Resistivity > 18.0 MΩ cm at 25^o C where the theoretically pure-water limit is 18.2 MΩcm.) to the stainless steel LTA at a flow rate of 5.7−11.4 lpm. In practice, the water actually delivered to the LTA was between 5.0 MΩcm and 17.5 MΩcm[3]. These resistivity values correspond to total dissolved solids of $\lesssim 140$ ppb and $\lesssim 40$ ppb respectively.

However, high resistivity alone does not guarantee optically pure water since even high

---

[3] Resistivity is the inverse of conductivity. Conventionally, conductivity is used to report water ionic content above 1 μS/cm and resistivity is used for conductivity values below 1 μS/cm.

Figure 4.3: The LTA and associated optical benches. The laser beam is injected at the far end, traverses the arm, is reflected from a flat mirror in the mirror enclosure, and returns to the injection enclosure. The effective length is 20.08 meters

resistivity water may contain concentrations of neutral organic contaminants which may adversely affect transparency, especially in the ultraviolet region. To remove these organic and microbial contaminants, our purification system also included a UV lamp and a 5.0 μm and a 0.22 μm ultra-filter (typical sizes of bacteria are 0.2 - 10 μm). While helping to remove organic contaminants, these purification steps also reduced the resistivity of our water somewhat since the end product of organic molecule photocatalytic oxidation is carbon dioxide which dissolves in the water to produce charged ions that increase conductivity [136].

The first step in obtaining pure water for our measurements was to fill the mixing tank with tap-water (0.01 MΩcm) after it had passed through a three-stage pre-treatment de-ionizer unit. Entering the mixing tank the resistivity of the water was $>$ 1.0 MΩ cm as measured by a hand-held conductivity meter. After storage in the mixing tank, the water is pumped from the tank into a mixed-bed polishing de-ionizer then into a Sterilight S5Q-Gold ultraviolet disinfection system which delivers UV light at 254 nm to provide a 99.99% reduction in bacteria, virus and protozoan cysts [137]. The final process is the passage of the water through the filters. The final 0.22 μm membrane filter removes any particles and bacteria greater than 0.22 μm. A resistivity meter was included in the system to make resistivity read-out convenient, however, a Total Oxygen Content (TOC) monitor was not installed.

Figure 4.4: The water purification system used to provide optically pure water to the LTA for light transmission testing.

The water system components were obtained commercially from South Coast Water, Inc and installed in a temporary hut erected outside Building 194 at LLNL in a dedicated shed. For containment reasons, the entire system was placed in a 770 gallon secondary containment berm (Figures 4.4 and 4.5).

The mixing tank, LTA and transfer piping contain a total of about 570 liters and the turn−over time (at a typical flow rate of 9.5 lpm) is approximately one hour.

Since attenuation measurements relative to a pure water baseline was all that was required to determine the desirability of using $GdCl_3$, a relative split-pulse laser method was used to determine the change in the attenuation constant α. The use of this split-pulse technique eliminated many problems that normally arise in conventional light attenuation and absorption measurements such as the need to account for changes in PMT gain variation and laser brightness fluctuations.

A wavelength tunable dye laser was used as the radiant source to assure proper collimation and to eliminate stray light from other types of light sources. The laser used was an L.S.I. VSL-337ND-S pulsed nitrogen laser which produced a 337 nm direct beam. In addition, the 337 nm laser output was used to pump two organic dyes via a DUO-210 Tunable Dye

Figure 4.5: The water hut with the front sliding door in the open position. The purification system, test tank, and portable resin beds all sit inside a secondary containment berm.

Laser attachment. The two dyes used were Stilbene-420 which produced a 420 nm pulse and PPBO which produced a 400 nm pulse respectively. Pulses of the dye laser were of about 4 ns duration, were approximately 0.1 nm in spectral width and had a repetition rate of 2 pps. Tables 4.3 and 4.4 provide the beam output characteristics for the nitrogen laser system and dye-laser attachment [138] [139].

Table 4.3: VSL-337ND-S Nitrogen Laser Output Characteristics.

Wavelength	337 nm
Spectral bandwidth	0.1 nm
Repetition Rate	0-60 Hz
Pulse Width (FWHM)	< 4 ns
Pulse Energy (typical)	> 300 μJ
Pulse-to-pulse Energy stability	< 4 % standard deviation
Peak power	> 75 kW
Avg power (30 Hz)	> 7.2 mW
Polarization	Unpolarized
Beam size (area)	35 mm^2
Beam divergence (full angle)	< 0.3 mrad

Table 4.4: DUO-210 DYE LASER 337210-0001 Laser Output Characteristics.

Spectral Range	360 - 950 nm
Spectral bandwidth	3 - 10 nm
Repetition Rate	1-30 Hz
Pulse Width (FWHM)	$<$ 3 ns
Pulse Energy (typical)	$>$ 90 μJ (500 nm)
Pulse-to-pulse Energy stability	4 % standard deviation
Peak power	$>$ 30 kW (500 nm)
Avg power (30 Hz)	$>$ 1.8 mW
Beam size (area)	1.4 x 2 mm
Beam divergence (full angle)	4 mrad

Light from the laser passed through two collimating apertures of 6.3 mm and 3.0 mm diameter and was then split by a 1-inch UV non-polarizing cube beamsplitter (Newport Optics P.N. 10SC16NP.42). One beam, that transmitted by the beamsplitter, then passed directly into a coated integrating sphere. At the output aperture of the integrating sphere a UV transmitting liquid lightguide (Lumatec Series - 250) was placed to receive this light and transmit it to a reflective rectangular cavity which housed a single mu-metal shielded 2-inch PMT (Hamamatsu H3378-50). The second beam, that reflected by the splitter, then passed through a 5/16 inch thick acrylic UVT window (Acrylite OP-04, 90% transmission) and into the 10 m long LTA which contained the pure water or $GdCl_3$-water solution. This beam exited the LTA through an identically constructed acrylic window as before on the other end of the LTA into a light-tight enclosure which housed a single 5.08 cm diameter UV mirror (Newport Optics BBDS-PM-2037-C). This mirror was aligned to reflect the beam back through the LTA and return it into the laser enclosure at an alignment point at the entrance aperture to a second spherical integrator for the case of the 337 nm measurements.

For the case of the 400 nm and 420 nm measurements, this beam was aligned to a point prior to entrance of an acrylic ‘light-box’ containing a solution of the LUDOX (HS-40, 12 nm diameter colloidal silica) in pure water. The change from the coated integrating sphere to the light-box was made to ensure that all the light from the less intense 400 nm and 420 nm beams was being measured and not lost due to the smaller aperture opening of the integrating sphere.

Similar to the other beam, a second Lumatec liquid lightguide was placed at the output aperture of the spherical integrator or at a fixed location at 90 degrees to the beam entering the LUDOX light-box. The lightguide transmitted the return beam into the rectangular enclosure housing the PMT which was powered by an ORTEC 556 high voltage power-supply. The use of the same PMT to measure both the beams allowed us to ignore gain variations associated with the use of two PMTs. The PMT output was read on a Tektronix DPO 4034 digital oscilloscope.

Figure 4.6 shows the detector optics arrangement used for the conduct of the transparency testing. The optics were arranged on optical tables and enclosed in two light-tight boxes at both ends of the LTA. The LTA is closed at both ends by 0.8 cm thick ultra−violet light transmitting (UVT) acrylic windows. Except for a 3 cm × 20 cm slit, the two acrylic windows at each end of the LTA are covered by black plastic to prevent unwanted external light from entering. The LTA contains four identically sized baffles spaced at intervals in the interior to reduce scattered light.

4.2.2 Description of Measurements

The change in the attenuation length of the $GdCl_3$-water solution can be determined by measuring the change in the ratio of the R laser pulse to the P laser pulse over time, where the R pulse is the pulse transmitted through the LTA and the P pulse is that which is transmitted directly into the integrating sphere.

Let

$$I = I_o \exp(-\alpha L) \tag{4.2.15}$$

where I is the intensity of the pulse at the distance L through the LTA, I_o is the initial intensity and α is the attenuation coefficient in m^{-1}. Assuming that P, R are proportional to I_o and I respectively, then:

$$P = aI_o; R = bI \tag{4.2.16}$$

where I is the intensity of the reflected pulse and a and b are constants of proportionality.

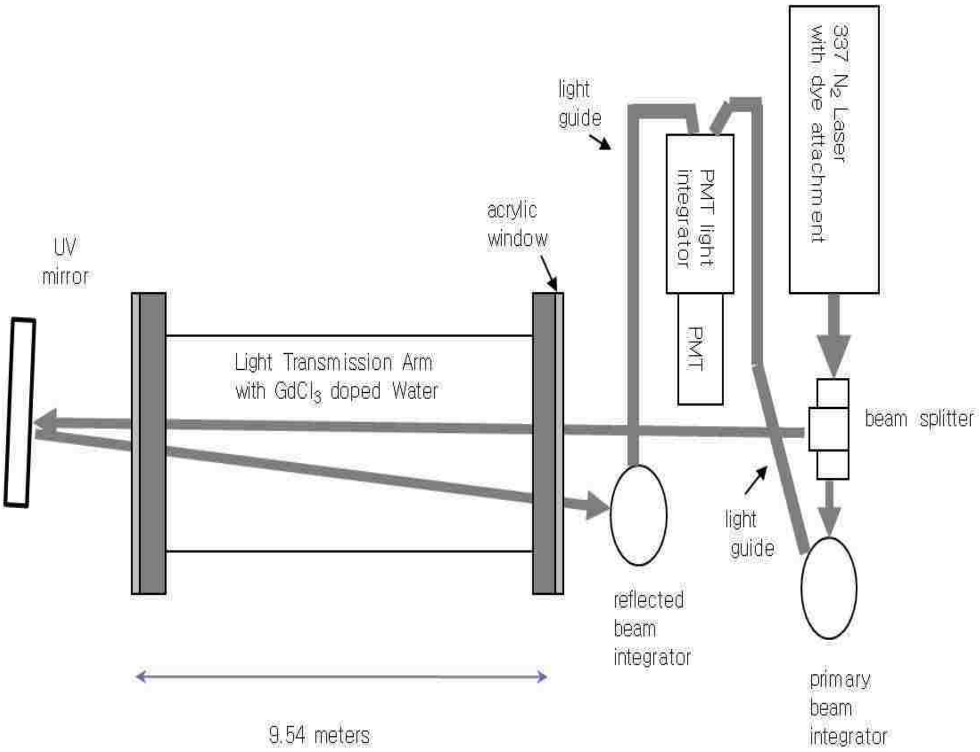

Figure 4.6: Schematic of injection and reflected beam optics. A laser beam is split into two, the primary beam is directed via an integrator to the PMT. The reflected beam traverses the LTA and is reflected into a second integrator, where it is collected and sent to the PMT. Delay time between the primary and reflected is ≈ 90 ns, sufficient to cleanly separate them in time.

We define the ratio:

$$\rho = \frac{R}{P} = \frac{b}{a}\exp(-\alpha L) \tag{4.2.17}$$

Letting ρ_1 be the ratio in pure water and ρ_2 be the ratio after adding $GdCl_3$, then:

$$\Delta\alpha = \alpha_2 - \alpha_1 = \frac{1}{L}\ln\frac{\rho_1}{\rho_2} \tag{4.2.18}$$

where the unknown constants a and b cancel. The uncertainty in $\Delta\alpha$ is then given by:

$$\sigma_{\Delta\alpha} = \sqrt{(\frac{\sigma_{\alpha 1}}{\rho_1})^2 + (\frac{\sigma_{\alpha 2}}{\rho_2})^2} \tag{4.2.19}$$

Typical values for pure water α at UV wavelengths are 0.01 m^{-1} – 0.02 m^{-1}.

4.2.3 Methods

The P and R beams were observed as two pulses well separated by about 90 ns on a Tektronix DPO 4034 digital oscilloscope. Figure 4.7 shows a typical trace for a double pulse at 337 nm. To determine the intensities, we integrate over the area of the single P and R pulses and then calculate the ratio ρ = R / P. To obtain ρ, we find the mean and variance of one-hundred separate pulses taken over a duration of about three minutes. This set of 100 pulses will be referred to as a 'measurement'.

In order to understand the response of the detector to changes in transparency caused by the addition of $GdCl_3$, we conducted a series of 'control' experiments by adding only pure water to the LTA and performing measurements identical to those to be performed with the $GdCl_3$ water solution. Before each measurement, the reflected beam was aligned to the same point at the entrance of the R beam light integrator and re-checked for alignment after completing each measurement. Typically it took about 10 minutes to take all readings between alignment checks. If the beam moved more than about 2 mm from the initial point of alignment, the measurement was discounted and a new measurement was taken after the apparatus had come to equilibrium.

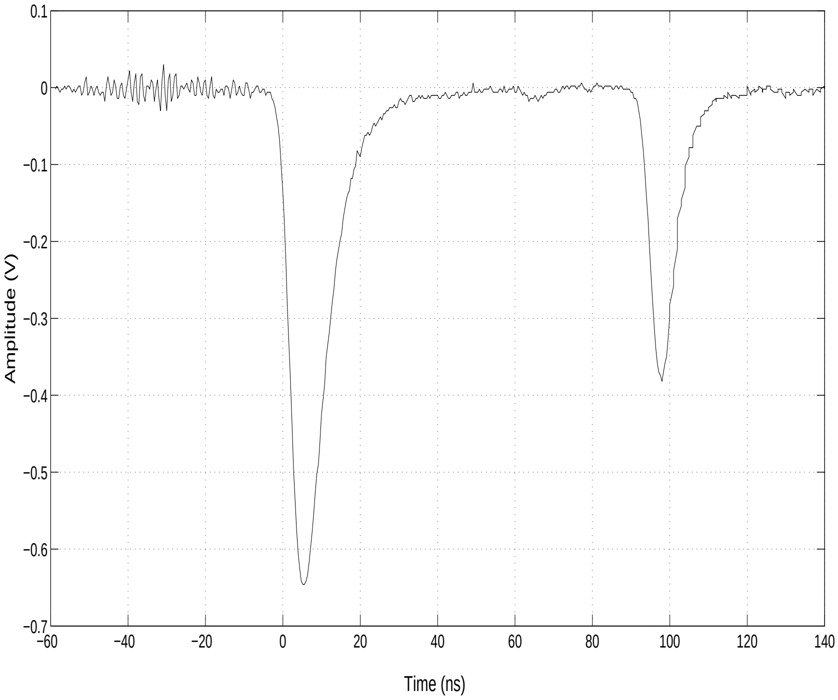

Figure 4.7: Oscilloscope output for a typical P and R pulse at 337 nm in pure water. The left and right pulses are the single PMT responses to the P and R beams respectively. The delay time between the primary and reflected is $\sim$ 90 ns, which is sufficient to cleanly separate the pulses in time. The time separation of the two pulses is due to the extra distance traveled by the R beam in water and air ($\Delta t = (19.25 \text{ m})(\frac{1.34}{3\times10^{8} m/s}) = 86 \text{ ns} + \sim 3 \text{ ns for air}$). The small amount of ripple is due to R.F. pick-up from the laser fire.

To prove the stability of our detector, another control experiment conducted was to circulate pure water through the water purification system and the LTA, stop the recirculation and then take measurements of ρ over a two week period while it remained sitting in the LTA (i.e. no circulation). These measurements are shown as a function of time in Figure 4.8 and indicate a 12.5% decrease in ρ over the period of more than two weeks. While the cause of the loss of transparency is unclear, it is of interest to note that the $\sim$ 1.0% per day fall off in transparency is less than that typically observed in SK with the recirculation turned off, even though the stainless steel surface to volume ratio of our apparatus is almost 200 times larger.

For the 337 nm and 420 nm measurements, the amplitudes of both P and R were approximately equal for the pure water measurements. This condition ensured that the response

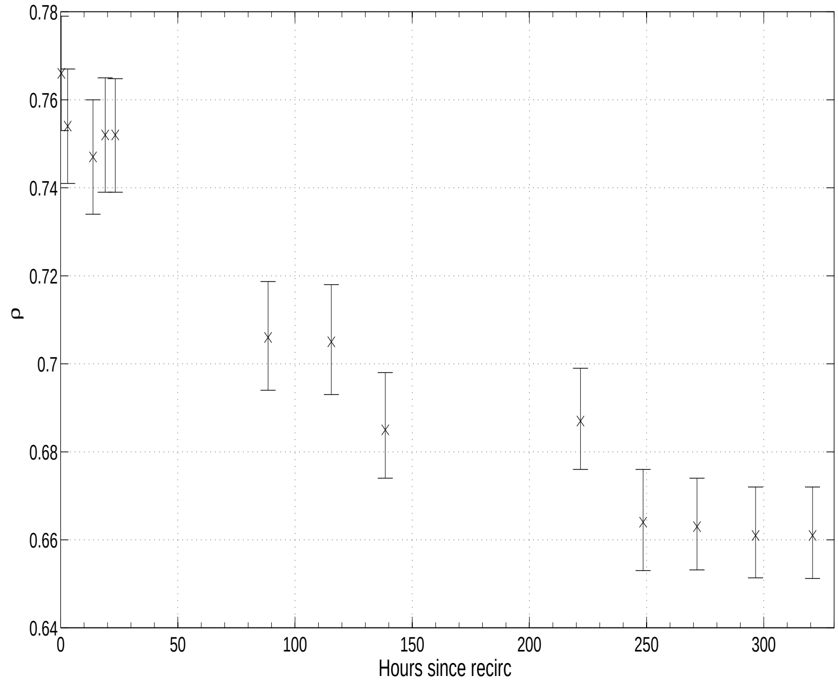

Figure 4.8: ρ of pure water measured over approximately 14 days at 337 nm. Recirculation of the water through the system was turned off at t=0. From this point, the water remained undisturbed in the LTA and ρ decreased at the rate of $\sim$ 1% per day. Errors are based on the variation of the measurements of the pure water baseline prior to circulating the water through the system.

of the detector to both the P and R pulses is the same. However, this condition was not met for the case of the 400 nm measurements due to the poor efficiency of the PBBO dye. Because of this fact, an independent alignment of the optical system at 400 nm was not possible. As a consequence, the alignment uncertainty is greater for 400 nm than the other two wavelengths as discussed in the section on uncertainties.

4.3 Uncertainty

Our measurements are affected by four significant sources of uncertainty. The first of these is associated with the variation in the pulse-to-pulse measurement of ρ over short time intervals due to thermal turbulence in water and the vibrational motion of optical components. To quantify this uncertainty, we take the average of the measured 100 pulse variation at each wavelength for each measurement of ρ in pure water. The values determined are: for 337 nm: ±0.6%; for 400 nm: ±4.4%; and for 420 nm: ±2.0%.

A second uncertainty was associated with reproducibility of the R beam alignment. This uncertainty was quantified by conducting alignments of 10 randomly 'misaligned' beams in rapid succession and obtaining the variations in the measurements of ρ. The beams were 'misaligned' by an independent person who moved the beam off of the alignment point by moving the mirror on the far end of the LTA randomly. The beam were then realigned. Based on these measurements, the following estimates for the uncertainty were obtained: for 337 nm: ±1.0%; and for both 400 nm and 420 nm: ±2.0%.

Another uncertainty is associated with the linearity of the system response to changes in light transparency. In this report no measurement of ρ below 45% were made so only the detector response above this value is addressed. To determine the detector linearity uncertainty, UV transmitting neutral density (ND) filters were inserted between the beam-splitter and the LTA and the measured ρ compared to the expected light transmission. The transmission of each of the ND filters was measured using a calibrated monochromometer to better than 0.5%. Figure 4.9 shows the normalized ρ value plotted against the filter transmittance. In this case, 'normalized' means that the ρ value with no filter present is taken to be 1. The uncertainty in the light transmission linearity is conservatively taken to be the difference in the slope of a fitted line from 1. The corresponding uncertainties are: ±0.8% for 337 nm; ±1.1% for 400 nm and ±1.6% for 420 nm.

Lastly, there was an uncertainty associated with the long−term stability of our detector. This uncertainty was quantified by determining the value of ρ after the $GdCl_3$ had been removed from the LTA and pure water re-added. We were able recover the original pure water baseline to within ±1.0%, ±2.5% and ±2.0% for 337 nm, 400 nm and 420 nm wavelengths, respectively. These values are taken as conservative estimates of the long-term drift. Table 4.5 lists the estimated uncertainties for our measurements at each wavelength.

Table 4.5: Estimated uncertainties associated with the measurement of ρ.

Percent Uncertainty	Wavelength		
	337nm	**400nm**	**420nm**
Short−Term Stability	0.6	4.4	2.0
Alignment	1.0	2.0	2.0
Long−Term Stability	1.0	2.5	2.0
Linearity	0.8	1.1	1.6
Total	**1.7** %	**5.6** %	**3.8** %

4.4 Results

4.4.1 The Addition of $GdCl_3$ to Pure Water

To ensure instrument stability and determine the long−term uncertainty as described in Section 3, a pure-water baseline from which to measure the relative change in transparency was obtained prior to adding the $GdCl_3$.

To ensure that this procedure did not effect transparency, we established a baseline to demonstrate that the mixing procedure itself did not introduce bias by mixing pure water from the mixing tank through the 0.22μm and 5μm filters, and the UV sterilizer. The pure water was not sent through the de-ionizer since after the $GdCl_3$ is mixed with water this

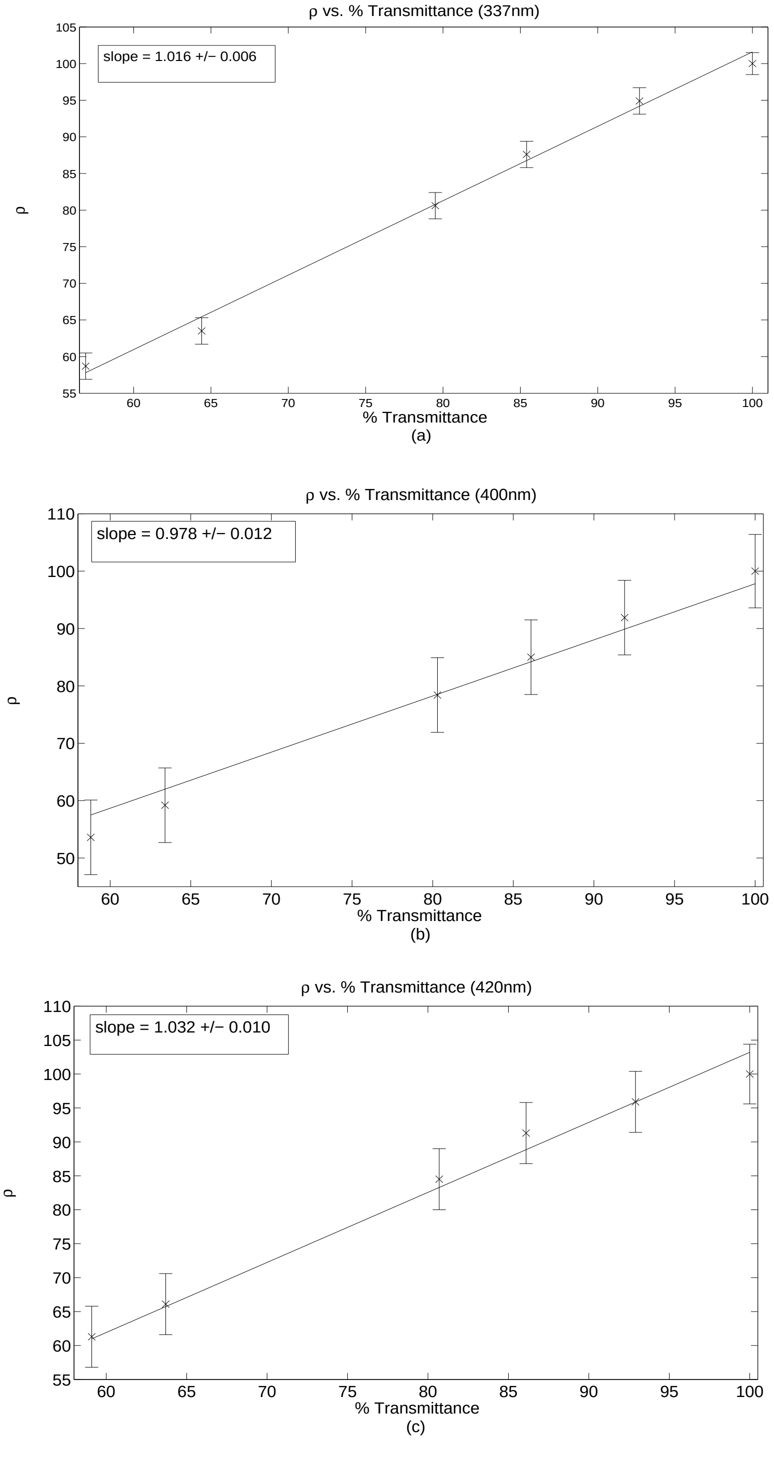

Figure 4.9: Measurements of light transmission linearity calculated by determining the change in ρ caused by placing neutral density filters of known light transmission in the laser light path for 337 nm (a), 400 nm (b) and 420 nm (c). Errors are based on the estimated uncertainties from Table 4.5

solution obviously can not pass through the de-ionizer. The pure water was then circulated through the LTA for 3 hours, the same length of time used for mixing the $GdCl_3$ with water. No significant change was observed at any of the three wavelengths as a result of this procedure.

Next, 1.23 kg of $GdCl_3 \cdot 6H_2O$ was added and mixed with 610 l of pure water contained in the mixing tank and stainless steel piping to give a concentration of 0.2% $GdCl_3$ by weight. The procedure for adding the $GdCl_3$ to the LTA was as follows:

1. The $GdCl_3$ was initially mixed in a 1 liter beaker of pure water.
2. The $GdCl_3$ - water solution was then added to the poly-propylene mixing tank and mixed using the stainless steel motor-driven stirrer for 10−15 minutes.
3. The system valve-alignment was changed to by-pass the de-ionizer.
4. The $GdCl_3$ - water solution was circulated from the mixing tank through the 0.22μm and 5μm filters and UV sterilizer.
5. The inlet and outlet valves to the LTA were opened and the $GdCl_3$ - water solution was circulated through the LTA for approximately three hours (roughly 3 turn-over times).
6. The LTA inlet and outlet valves were closed and the water pump was stopped.

The results of measurements obtained after addition of $GdCl_3$ observed for roughly a 2 day period, are shown Figure 4.10. Two results are clear. First, the decrease in ρ over time was consistent with a linear decrease. In fact, since the $GdCl_3$-water solution remains undisturbed in the LTA after it is mixed, this result suggests a proportionality between decreasing transparency and a change in water quality due to increasing the Gd solution's exposure (with time) to the stainless steel LTA surface. This point should be stressed: following the mixing of the $GdCl_3$ with the water, the LTA is isolated. The $GdCl_3$ solution has no contact with anything except the LTA surface, the PVC baffles in the LTA and the acrylic LTA windows.

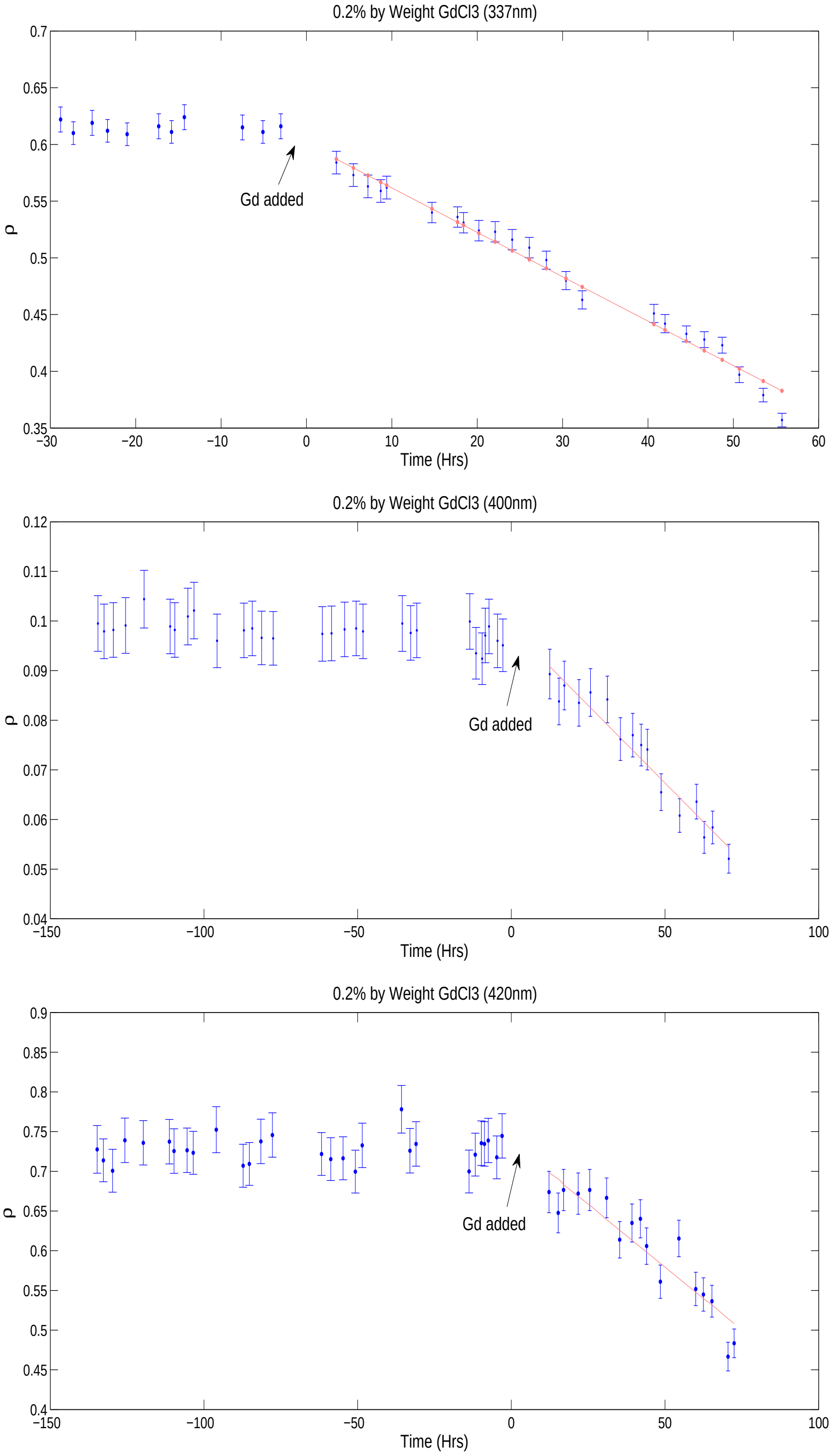

Figure 4.10: Decrease in transparency versus time resulting from addition of 0.2% $GdCl_3$ in pure water for 337 nm (a), 400 nm (b) and 420 nm (c). The red line shows the least squares best fit to the data after addition of the $GdCl_3$.

Table 4.6 provides the fitted slope and the y-intercept ($t = 0$) ρ values for all three wavelengths. The last column of Table 4.6 indicates the level of dissolved oxygen at the time that the $GdCl_3$ was mixed with the pure water. The slope and intercepts in Table 4.6 correspond to the following values for $\Delta\alpha$ at the 90% confidence level: $\Delta\alpha_{337} = 3.4 \pm 28.0$ $\times 10^{-4}$ m^{-1}, $\Delta\alpha_{400} = 5.3 \pm 66.0 \times 10^{-4}$ m^{-1} and $\Delta\alpha_{420} = 1.2 \pm 53.0 \times 10^{-4}$ m^{-1}.

Table 4.6: The Fit parameters (slope and intercept) for the linear decrease in ρ observed after the addition of $GdCl_3$ for the three measured wavelengths.

λ nm	pure water mean	slope $\times 10^{-4}$ (hr^{-1})	intercept	reduced χ^2	O_2 (ppm)
337	0.62	-42.0 ±1.7	0.619 ±0.006	0.60	0.90
400	0.10	-6.2 ±0.4	0.100 ±0.002	0.33	0.15
420	0.73	-30.0 ±2.9	0.744 ±0.019	0.61	0.15

At all three wavelengths, the fitted line intercepts the $t = 0$ axis at a value consistent with the pure water baseline ρ value. This provides strong evidence that the addition of the $GdCl_3$ alone does not instantaneously decrease water transparency. Rather, it suggests that the drop in ρ results from the introduction of impurities into the $GdCl_3$ water solution from it's exposure to the walls of the stainless steel pipe.

4.4.2 Change in Transparency Due to the Presence of Iron in Water

As discussed above, measurement of ρ made after the addition of $GdCl_3$ indicates that the addition alone does not cause a direct loss of transparency and that the loss of transparency over time is linear. These results suggest that exposure of the solution to the surface of the stainless steel LTA may be a source of the decrease in ρ. Clearly, one source of potential contamination is Iron (Fe) since it is a strong absorber of UV.

To investigate the concentrations of iron required to reduce transparency in our apparatus, small amounts $FeCl_3$ were added to pure water in the mixing tank after by-passing the DI and removing the filters in the water purification system. The filters were removed from the system to ensure that any iron in the water would not accumulate on the filters. Table

4.7 shows the change in ρ due to the addition of 14 ppb and 28 ppb of $FeCl_3$ in pure water at a wavelength of 337 nm.

Table 4.7: The change in ρ resulting from the addition of $FeCl_3$ to pure water.

pure water value	14 ppb $FeCl_3$ in water	28 ppb $FeCl_3$ in water
0.901 ± 0.018	0.355 ± 0.018	0.156 ± 0.008

As seen in the table, the change in ρ due to the addition of only 14 ppb of $FeCl_3$ to pure water results in an immediate reduction in ρ to about of 40% of the pure water value while the addition of 28 ppb of $FeCl_3$ to water drops ρ to 16% of the pure water value.

It is clear that the presence of extremely small amounts of $FeCl_3$ significantly reduces water transparency.

4.5 Conclusion and Future Work

We have shown that $GdCl_3$ is problematic for use as a dopant for detectors lined with stainless steel (e.g. Super-Kamiokande) due to it's effects on water transparency. At concentrations of 0.2% by weight, the transparency of the $GdCl_3$ doped water decreases rapidly over time scales of a few days for all three UV wavelengths tested. However, since the addition of $GdCl_3$ by itself does not reduce transparency, it may be suitable for detectors made of non-corrosive materials.

Chapter 5

Nuclear Reactor Monitoring with Antineutrinos and the SONGS Water Cherenkov Detector

5.1 Introduction

The proliferation of nuclear weapons and nuclear technology is a main global security concern. The current programs put in place by safeguards agencies like the IAEA (International Atomic Energy Agency) to prevent the diversion of material from nuclear power reactor programs into weapons programs rely primarily on operator accounting, reporting and onsite verification of the content of spent fuel pools.

Yet because nuclear reactors are a prodigious source of antineutrinos, which are impossible to shield, several research groups are involved in attempts to apply antineutrino detection as a new technology in what is called the “Safeguards Regime” for the prevention of nuclear weapons proliferation. Such an application would provide a method to independently verify operating conditions and reactor isotopic content without disrupting reactor operations.

The concept of using antineutrinos to monitor reactors was first proposed by Mikaelian [150] and several research groups are currently investigating this potential application of neutrino physics. These include a Russian research group at the Rovno nuclear complex in the Ukraine and a collaboration of Sandia National Laboratories (SNL) and Lawrence Livermore National Laboratory (LLNL) groups as well as groups in France (Double Chooz and Nucifer) [151] [152], Japan [153] and Brazil [154].

The SNL/LLNL collaboration has been involved in this area of research for almost a decade. This group has developed three prototype antineutrino detectors (plastic scintillator, liquid scintillator and water Cherenkov), and installed and operated them at the San Onofre Nuclear Generating Station (SONGS) in San Onofre, CA. The SNL/LLNL SONGS I liquid scintillator detector [145] was operated at the SONGS site between 2003 and 2006. The active volume of this detector comprised 0.64 tons of Gd-doped liquid scintillator contained in stainless steel cells which were surrounded by a water/polyethylene neutron-gamma shield and plastic scintillator muon veto. Both the ability of the detector to track changes in reactor thermal power over as little as 5 hrs with 99% confidence and to track fuel burnup [147] by increasing the averaging time to 30 days were demonstrated (Figure 5.3)

In this chapter a description of the key features of the SONGS Water Cherenkov Detector experiment will be presented. This detector uses Gd-doped water produced by the apparatus described in the previous chapter as the detection medium.

5.2 The Production of Antineutrinos in Nuclear Reactors

The most common type of nuclear reactor is the Light Water Reactor (LWR) fueled with Low Enriched Uranium (LEU). In this section, a summary of the antineutrino signal from this type of reactor will be described.

When a nucleus undergoes fission, the majority of unstable products are neutron rich nuclei which predominantly beta-decay and emit antineutrinos. The underlying process is the conversion of a neutron into a proton, electron and antineutrino:

$$n \rightarrow p + e^{-} + \overline{\nu_e} \tag{5.2.1}$$

On average, about 5 to 6 antineutrinos are emitted per fission, although not instantaneously since each of the fission products has a finite life-time. However, once the reactor has reached steady state, this time variation is not a factor. A typical power reactor has a thermal power output of about 3 GW, and the energy release per fission is about 200 MeV.

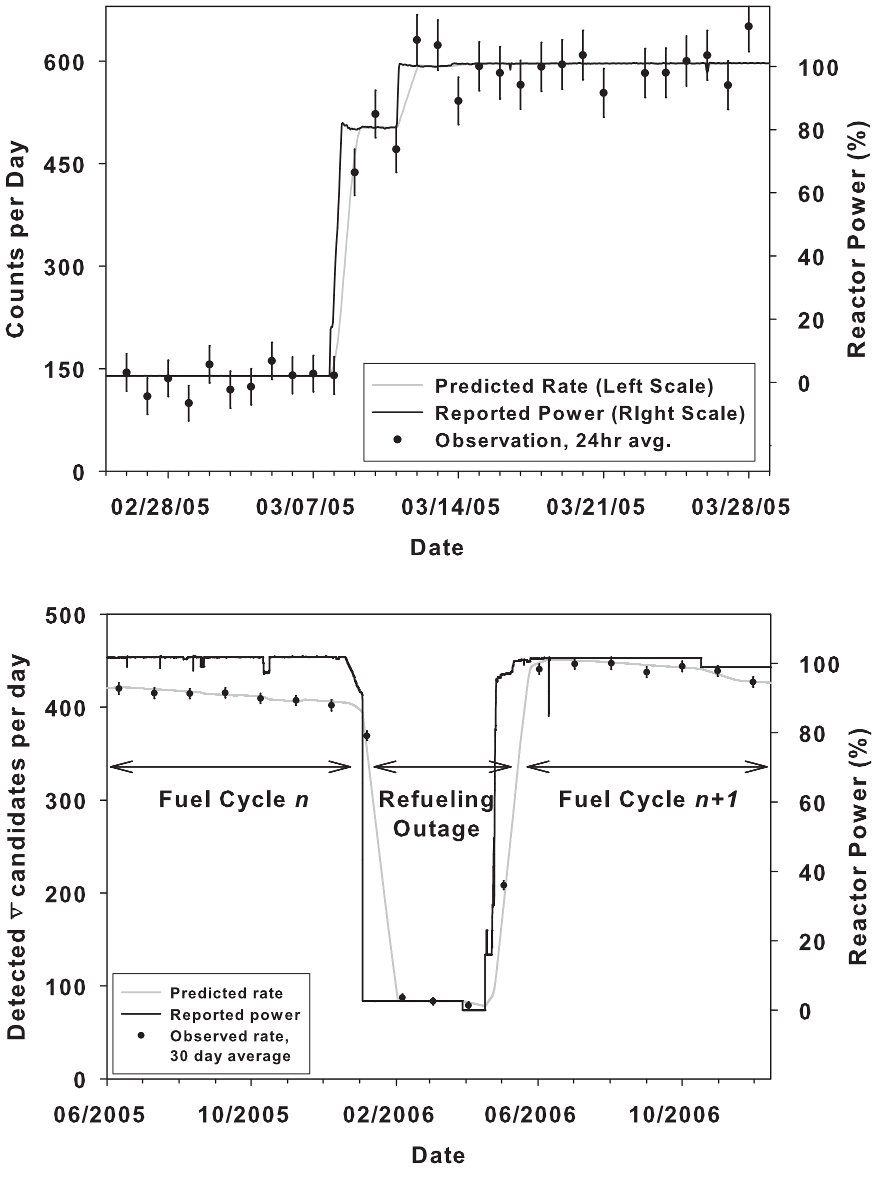

Figure 5.1: Top: The SONGS1 Unit 2 Reactor ramping from zero to full power over the course of several days. Bottom: Antineutrino rate measurements before, during, and after a reactor refueling outage indicating the decrease in antineutrino detection as the fuel evolves. These figures were taken from [155].

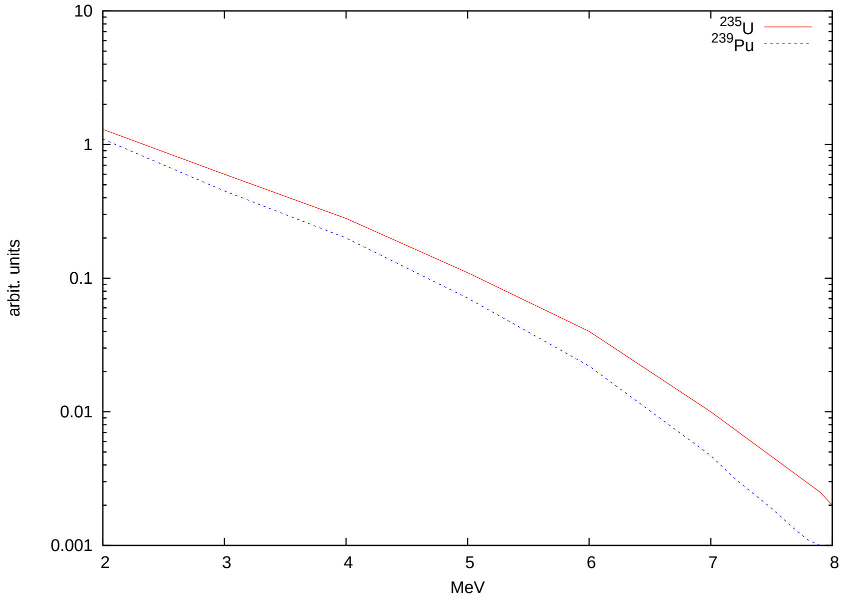

Figure 5.2: The relative energy spectra of the antineutrinos from the fission of the two most important fissile elements ^{235}U and ^{239}Pu [140]. The y axis is in arbitrary units.

So approximately 10^{21} antineutrinos per second are emitted isotropically from the core of the reactor. The energy of the antineutrinos range from zero to about 15 MeV. Only a small fraction of the antineutrinos have energies above 8 MeV and the average energy is about 3 MeV. Figure 5.2 shows the relative energy spectra of the antineutrinos from the fission of ^{235}U and ^{239}Pu.

The energy distribution of the antineutrinos contain spectral contributions from numerous fission daughters and the distributions have been derived from beta spectrometry measurements [141][142] [143]. The differences in the fission products lead to differences in the magnitude and the shape of the respective spectra.

5.2.1 Reactor Burnup

As can be seen in Figure 5.2, the average number of antineutrinos produced per fission is different for ^{235}U and ^{239}Pu. As the core evolves, the relative mass fractions and fission rates of these isotopes change. This results in a change in the measured neutrino flux. The relation between the fissile mass fractions and antineutrino flux is known as the burnup effect. The dependence of the antineutrino rate on the individual isotopic fission rate can be written as[144]

$$N_{\overline{\nu_e}} = \frac{N_p W \epsilon}{4\pi R^2} \times \frac{\sigma_5 \left(1 + \sum\limits_i \alpha_i (\frac{\sigma_i}{\sigma_5} - 1)\right)}{E_5 \left(1 + \sum\limits_i \alpha_i (\frac{E_i}{E_5} - 1)\right)} \tag{5.2.2}$$

where N_p is the number of target protons, W is the thermal power, R is the detector distance, ϵ is the detection efficiency, σ_i is the cross section for the inverse beta decay reaction averaged over all energies, where $i = 5, 8, 9, 1$ represents ^{235}U,^{238}U, ^{239}Pu, ^{241}Pu respectively, α_i is the fractional contribution of each of these isotopes to the total fission rate with the constraint that $\sum\limits_i \alpha_i = 1$, and E_i is the energy release per fission of the ith isotope.[1] For example, σ_5 and E$_5$ are the cross section and energy for ^{235}U.

The relation between reactor thermal power, the fuel burnup, and the antineutrino detection rate can be rewritten as [145]:

$$N_{\overline{\nu_e}} = \gamma(1 + k(t))W(t), \tag{5.2.3}$$

where γ is a constant encompassing all non-varying terms (N_p, R, ϵ, E$_5$ and σ_5), W$_{th}$ is the reactor thermal power, and $k(t)$ describes the change in the antineutrino flux due to changes in the reactor fuel composition. Note that even for the case of constant thermal power, the parameter $k(t)$ changes by about 10-12% over the course of a reactor cycle as ^{235}U is consumed and ^{239}Pu is both produced and consumed in the core.

5.2.2 Rate Based Measurements

In reactor antineutrino oscillation experiments, Equation 5.2.3 is used to predict the antineutrino rate based on thermal power measurements obtained from the reactor operators and on simulations of the fissile isotopic content of the core as a function of time. These predicted antineutrino rates are used to compare with measurements to determine oscillation behavior. However, for reactor monitoring, one inverts the process in order to estimate the

---

[1] A factor which accounts for neutrino oscillations multiplies Equation 5.2.2, but it is unity for reactor antineutrino detection distances of less than about 500 m.

fissile content by using a measurement of $N_{\overline{\nu_e}}$. But it is important to note that as long as the flux alone is used this estimate depends on knowledge of the reactor operational information such as thermal power, initial enrichment and isotopic content and the predicted isotopic evolution. On the other hand, in the context of a safeguards, a measurement made relative to an initial reference start up condition may be sufficient.

To simply determine the operational status of a reactor on a daily or weekly basis, one requires that the change in the antineutrino detection rate be several standard deviations above background within the observation period. Even with modest suppression of backgrounds, the SNL/LLNL group and the Russian group at Rovno have shown that this is easily achievable at detectors located ∼10-100 meters from the reactor[145][146][147][148]. Detectable antineutrino rates of 100-1000 events per day per ton resulted in signal to square root of background of ∼10-50.

For the purpose of weekly power or burn-up monitoring in a rate-based measurement, sufficient events are required so that statistical uncertainty does not dominate the $\approx 0.5\%$ change per month due to burnup. This requires an event detection capability of about 10000 events per month, or about 300 events/day.

5.2.3 Measurements of the Antineutrino Spectrum

In comparison to a rate based measurement, a measurement of the antineutrino spectrum would require little outside information from reactor operators. To see this, Figure 5.3 shows the spectra in Figure 5.2 after they are convoluted with the energy dependent inverse beta decay cross section,

$$\overline{\nu_e} + p \rightarrow n + e^{+}. \tag{5.2.4}$$

This reaction is the most commonly used and practical method for detecting reactor antineutrinos and is the reaction used in the reactor experiments described here.

Note from Figure 5.2 that the detected spectra differ by more than 50% at high energies. Such spectrum based measurements are capable of measuring the changing isotopic composition of the reactor core. Specifically, plutonium and uranium isotopic content and

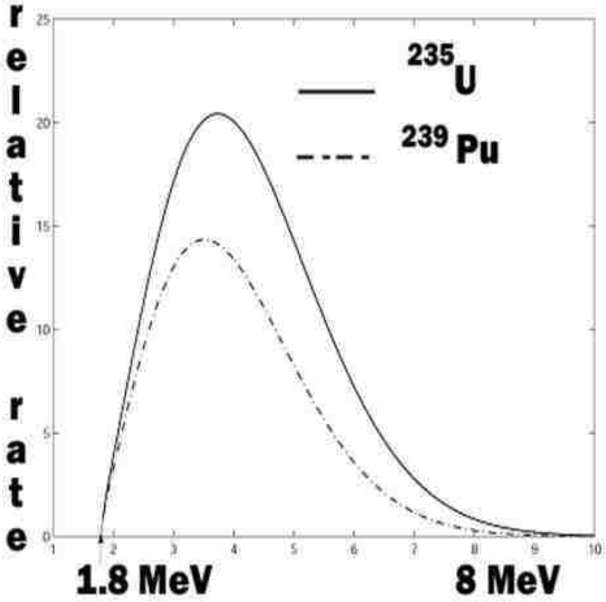

Figure 5.3: The spectra of Figure 5.2 convoluted with the inverse beta decay cross section.

power can be derived from a fit to the integral antineutrino energy spectrum, taking the unknown fission fractions α_i and the thermal power, W, as free parameters. In this manner, the Pu content in an LWR reactor in an equilibrium cycle can be estimated to within 10% [149]. This equates to about 40 kg of Pu. Reduction of the theoretical uncertainties on the antineutrino flux of only a factor of 3 would allow for a 20 kg estimate of the total fissile Pu content.

5.3 The SONGS Water Cherenkov Antineutrino Detector

While the SONGS1 experiment was very successful, some concern among the safeguards community focused on the use of flammable liquid scintillator and the associated safety compliance efforts required of reactor operators. After Beacom and Vagins published their paper [99], the SNL/LLNL collaboration determined to undertake an investigation of the use of Gd-doped water as an antineutrino detector for the purpose of determining the potential of this type of detector for safeguards monitoring.

5.3.1 Detector Description

The detector [156] consisted of two separate acrylic tanks: one small tank atop a large tank separated by an O-ring seal. The lower tank (1 m×0.5m×0.5m) contained ultra pure sterilized water doped with 0.2% $GdCl_3$ produced in the LLNL Water Cherenkov Test Facility [2]. This tank formed the main 250 l active target volume of the detector and was fitted with a small expansion volume to keep the target volume full and optically coupled to the top tank. The walls of the tank were made from $3/8''$ UVT acrylic.

The top tank contained ultra-pure, sterilized and de-ionized water without the Gd dopant and 8 downward facing 8 inch ETL 9354kb PMTs separated by 1 inch spacing. These PMTs have a relatively high quantum efficiency at short wavelengths ($\approx$30%). The PMTs faced downward into the lower tank and were individually shielded from magnetic field effects by 8 inch diameter cylinders of mu-metal. The PMT and target volumes were separated to prevent exposure to the $GdCl_3$ doped water.

Figure 5.4 shows a schematic of the inner detector. A top 1 cm Delrin flange forms the lid of the upper small tank and a lower flange formed the barrier between the small tank containing the undoped pure water and the target volume. The top tank was filled to about 10 cm. The PMTs fit snugly inside the mu-metal shields which were inserted into the top tank with the basis penetrating the top of the detector. The top and bottom tanks are wrapped externally with reflective 1073B Tyvek (a white paper-like material, about $\sim$ 200 μm thick, made of pressed polyethylene fibers) on four sides and five sides respectively.

The two water tanks were surrounded by a five sided plastic scintillator muon veto. The purpose of the veto was to time-stamp muons passing through the inner detector to allow rejection of muon-related backgrounds.

Figure 5.5 shows the architecture of the data acquisition and trigger. The eight ETL 9354kb PMTs in the inner detector used positive HV. The anode was AC coupled and the signals extracted were fed straight into custom preamplifiers built into the bases. The preamplifiers produced tail pulses (pulses that exponentially decay back to 0) that were sent to a CAEN N568B 16-channel spectroscopy amplifier for shaping. Two signals exited the spec-

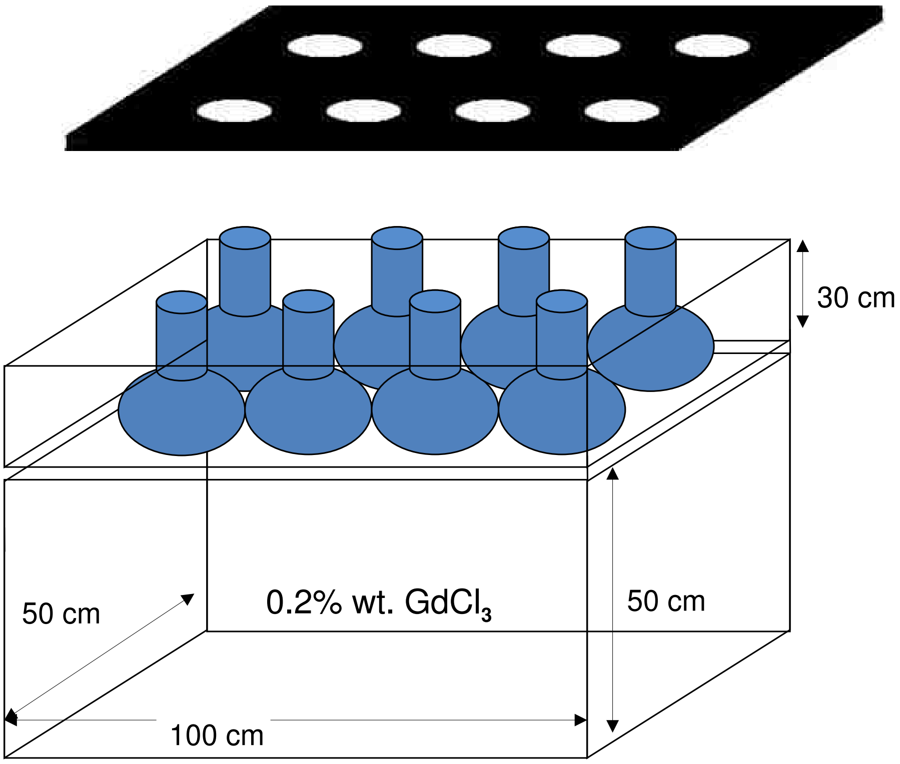

Figure 5.4: Schematic of the SONGS water Cherenkov detector showing the two tanks, the Delrin top cover with opening for the PMT bases, and the location of the PMTs.

troscopy amplifier for every one entering. One was amplified, shaped into a positive Gaussian pulse and sent directly to a peak sensing 12 bit CAEN V785 Analog-to-Digital-Converter (ADC). The other signal was fast amplified and sent to a low threshold 16 channel discriminator (CAEN V814). Digital signals from the discriminator were sent to the CAEN V1495 FPGA module, which issued a global trigger when any four channels trigger simultaneously and no muon veto signal had occurred within 20 μs. A non-retriggerable logic pulse of about 3 microseconds duration was produced at this stage since this was the approximate duration of the shaped output of the N568 spectroscopy amplifier. Accepting events with shorter separation would have resulted in pulse pileup at the ADC's. Note that for this reason a 10 μs lower limit on the interevent time interval is set in the next chapter. At the issue of a global trigger all 8 ADC channels were read out to a disk together with the time since last trigger and time since last muon veto trigger.

The muon veto was read out by ten 2-inch diameter PMTs attached to seven plastic scintillator panels. Four side panels were read out by one PMT each, while the top and two end panels each had two PMTs. The signals from all ten PMTs were sent directly into a CAEN V812 Constant Fraction Discriminator (CFD). Digital pulses from the discriminator were sent to the FPGA to apply the 20 μs veto.

To repeat, an event that caused four inner detector PMTs to fire in coincidence, at least 20 microseconds after the passage of the last muon and 3 microseconds after the last coincidence signal resulted in one of the ADCs being gated. Gates were generated for each ADC in turn, so that while one ADC was digitizing (digitization time was approximately 6 microseconds) the other could accept another event. Gates were generated until the 32 event buffer on each ADC was full. Once these buffers had been emptied, the flip flop generating the alternating gates was reset so that it could be known which ADC received the first trigger. This allowed subsequent events to be formed into correctly ordered pairs in later analysis.

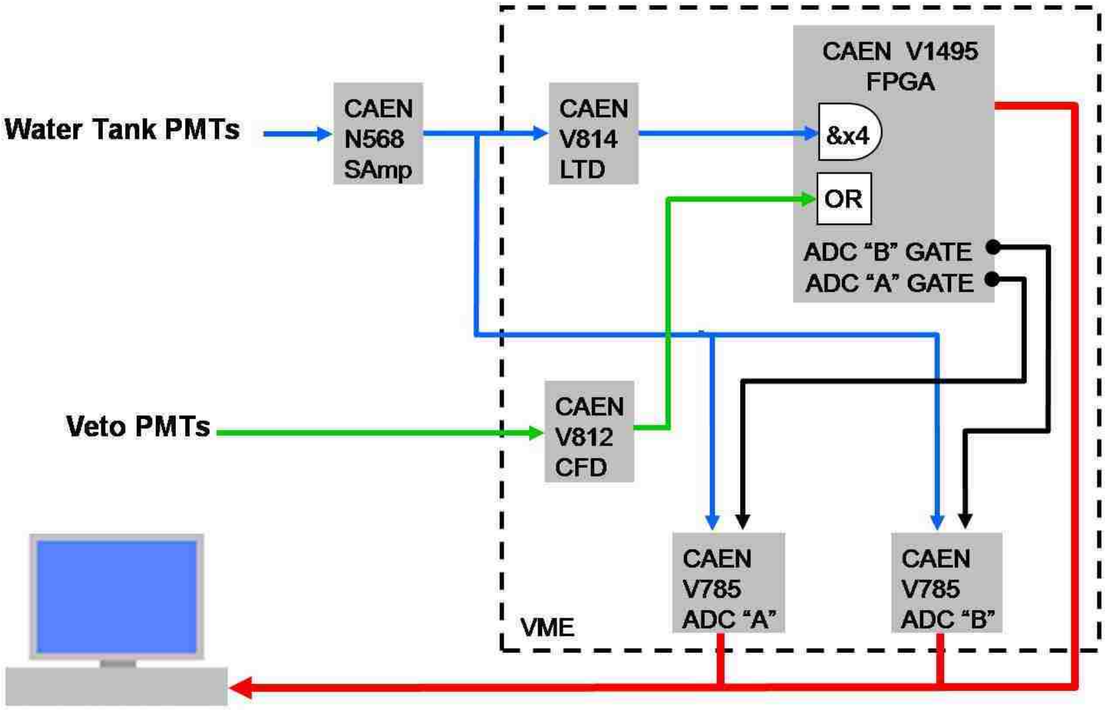

Figure 5.5: The data acquisition system and trigger logic for the SONGS WCD.

An installed telephone modem was used to automatically retrieve the data as well as detector health indicators and allowed for remote monitoring of detector operation.

5.3.2 Pre-Deployment Testing

Prior to installation at SONGS, the ability of the detector to detect high energy and neutron capture gammas was tested at LLNL [156]. A fission source (^{252}Cf) was placed approximately 1 m from the detector behind a two inch lead wall. The neutron yield for this source was about 2.4×10^5 neutrons/s. For (^{252}Cf), the neutron energy is peaked between 0.5 and 1 MeV, although a significant number of neutrons have energies as high as 8 or 10 MeV [159].

As a result, the raw event rate of the detector increased from 700 Hz to 7 kHz and the summed PMT response from all 8 PMTS indicated that the ^{252}Cf did in fact change the spectral shape relative to background. In addition, the interevent time signal between consecutive events indicated a correlated component which could be fit by an exponential corresponding to a mean interevent time of 29 μs. This component of the interevent time distribution agreed well with the mean interevent capture time in water or liquid scintillator for a gadolinium concentration of 0.1% (0.2% $GdCl_3$ concentration by weight). This correlated component is due to either the detection of a prompt gamma followed by a delayed neutron capture or two neutron captures where both neutrons are emitted in the same fission event. A smaller correlated neutron capture signal was also detected when no ^{252}Cf source was present. This was assumed to be due to spallation caused by the passage of muons near the detector and muon capture nearby. Both of these can result in gammas and neutrons or multiple neutrons due to the same muon and hence produce a correlation. One other important feature of the detector was determined during this testing: The spectral shape of the neutron only capture events in the presence of the ^{252}Cf was extracted. The resulting spectrum looked similar to the neutron/gamma spectrum in the presence of the neutron source and indicated that the detector was not able to distinguish on an event-by-event basis between high energy fission gammas and the 8MeV capture gamma cascade on the basis of energy alone.

5.3.3 Backgrounds

The main expected backgrounds for "shallow" neutrino experiments are:

1. Neutron-neutron events whereby two neutrons from the same parent muon fake the prompt-delayed pair;
2. Accidental gammas originating from outside the detector which "fake" the prompt signal followed by the capture of a neutron which "fakes" the delayed event;
3. ^{9}Li events, where the spallation product ^{9}Li decays as $^{9}\mathrm{Li} \rightarrow 2\alpha + n + \beta^{-}$ and the electron and neutron "fake" the prompt and delayed pair. In this case, the ^{9}Li are produced from spallation of carbon or other nuclei in the surrounding materials by cosmic-ray muons [158].

As discussed previously, events in which elastic scattering of a fast neutron on a proton yields the prompt signal and the capture of that neutron on another proton yields the delayed signal will not induce backgrounds in the SONGS WCD since the energy threshold for proton recoils is very high (> 1.5 GeV).

5.3.4 Characteristics of the SONGS Site

The SONGS water Cherenkov detector was deployed at the San Onofre Nuclear Generating Station (SONGS). Two operational reactors (Units 2 and 3) are located at this site. Both are pressurized water reactors designed by Combustion Engineering in the 1970s and have maximum thermal (electric) power of 3.4 GW_{th} (1.1 GW_{elec}).

The detector is located in the tendon gallery of Unit 2 (Figure 5.6). The tendon gallery is an annular concrete hall that lies beneath the wall of the reactor containment structure. It is a feature of many commercial reactors and is used to inspect and adjust the tension in reinforcing steel cables which extend throughout the concrete of the containment structure. The tendon gallery is located about 10 m below the surface, providing approximately 25 meters of water equivalent (mwe) overburden. The temperature in the tendon gallery is not actively controlled. Due to the underground location diurnal temperature variations at the detector are small ($< 0.1^o$ C), but there is a slow seasonal variation of up to 5^o C [157].

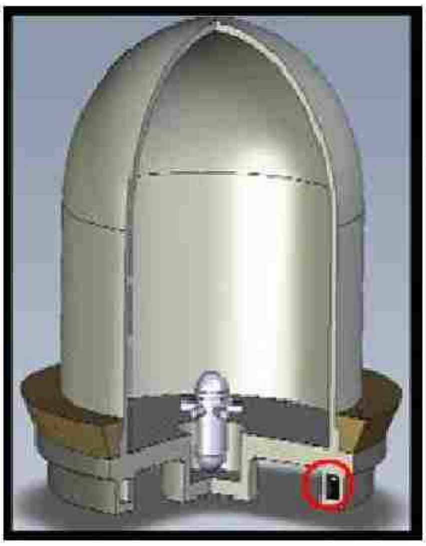

Figure 5.6: The location of the SONGS 1 liquid scintillator detector in the tendon gallery in relation to the SONGS reactor core. The tendon gallery is the annular concrete hall lying directly beneath the reactor containment structure.

The detector was located 24.5 ± 1.0 m from the Unit 2 reactor core and 149 ± 3 m from that of Unit 3. Because the antineutrino flux generated by each core is isotropic, 97% of the reactor antineutrinos reaching the detector originate from Unit 2. With Unit 2 at full power the antineutrino flux at the SONGS1 location is $\approx 10^{17}\mathrm{m}^{-2}\mathrm{s}^{-1}$.

Chapter 6

SONGS Water Cherenkov Detector Data Analysis

The main feature and area of original research associated with the SONGS WCD is the addition of Gd to the water to enable the use of coincidence detection to reduce backgrounds and make low energy antineutrino detection possible. A primary goal of the experiment is to verify that a relatively inexpensive, small and easily constructed technology can be used for tagging neutrons to enable the detection of reactor antineutrinos.

In this chapter, the method of analyzing the SONGS WCD data will be described. Specifically, the procedure to determine the number of potential reactor antineutrino events from the distribution of interevent times between prompt and delayed PMT signals will be explained and the results of this analysis will be presented.

6.1 Brief Description of the Data

The analysis ultimately seeks to identify events characterized by two energy depositions arising from the positron and neutron interactions in close time coincidence occurring within the detector. These events result from the inverse beta decay reaction initiated by reactor antineutrinos.

The first step of the analysis is to form candidate event pairs from the raw singles data. For each pair of sequential events, the first is designated a “prompt event” and the second event is designated a “delayed” event. In addition to the PMT charges, two time intervals are also recorded. The first of these is the time interval between the prompt event and the most recent muon veto. The second recorded time interval is the time between the prompt and delayed events in an event pair. This time interval is termed the "interevent time" in the analysis that follows.

Detector event files are comprised of the following elements:

- **t12**: the interevent time between the sequentially ordered pairs of prompt and delayed events.
- **tmu-p; tmu-d**: the time from the last muon to the prompt and delayed event respectively.
- **tmu-nv-p; tmu-nv-d**: the time from the last muon to the prompt and delayed event respectively under the condition that the system is not vetoed.
- **p1 p2 p3 p4 p5 p6 p7 p8**: the charge recorded by the Analog-to-Digital Converters (ADCs) for each PMT (1 through 8) for the prompt event in each event pair.
- **d1 d2 d3 d4 d5 d6 d7 d8**: the charge recorded by the Analog-to-Digital Converters (ADCs) for each PMT (1 through 8) for the delayed event in each event pair.
- **padc; dadc**: the record of which of two ADCs was gated for the prompt and delayed events respectively for each single event.
- **eob**: 0 or 1 indicating that the file being written to was accepting data.

Data summary ASCII files are uploaded continuously to a secure website. These files contain the data elements described above as well as trigger and state of health data for all the electronic systems in the detector, including the PMTs, high voltage power supplies, the logic processing crates and the data acquisition computer. Events are written sequentially and are streamed to a disk after they are recorded. The fundamental units of data analysis are 24 chained event files containing events corresponding to one hour of data. One complete hour of data normally comprises $\approx 2\times10^6$ prompt/delayed event pairs and is contained in a 175-200Mb data file.

Prior to further analysis, the data sets comprising a single days worth of hourly files are chained together and two simple energy cuts are made to reduce the total file size so that it can be processed by PAW[1][160]. These two cuts are:

- A cut to require that each individual prompt and delayed PMT signal be less than ADC value 3840. Signals exceeding ADC value of 3840 are classified as "saturated[2]". This cut is implemented to remove events with a muon component.
- A cut to require that the sum of all prompt PMT signals *and* also the sum of all delayed PMT signals are each greater than ADC value 1500. This cut was established based on the fact that background rates below this threshold value are very high and would swamp any correlated signal.

6.2 Gain Correction

The pedestal values (i.e. the ADC values corresponding to triggers without emission of photoelectrons) were determined off-line by histogramming the hourly spectra and locating the lowest value peak in the distribution. Figure 6.1 shows the raw non-pedestal-subtracted and pedestal-subtracted spectra for PMT 1 obtained for a 48 hour period.

Dark box measurements were performed prior to placing the PMTs in the detector on site at SONGS in order to obtain the single photoelectron (spe) peak. To match the gains of each individual PMT, the voltage was varied to achieve the desired peak location. These voltages were then used to pre-set the PMT power supplies for gross equalization of the PMT gains prior to beginning data acquisition.

The design of our detector did not allow for the periodic checking of individual PMT fine gain correction factors from a calibrated light source nor from a single photoelectron distribution. Furthermore, because water Cherenkov produces so few photons, a complete energy calibration is not possible. Fortunately, the SONGS WCD experiment was primarily a

---

[1] The Physics Analysis Workstation (PAW) is based on several components of the CERN Program Library and provides interactive graphical presentation, mathematical and statistical analysis tools. PAW usage and redistribution is granted under GNU Generic Public License.

[2] The 12 bit CAEN V785 peak sensing ADC saturates at an ADC value of 3840

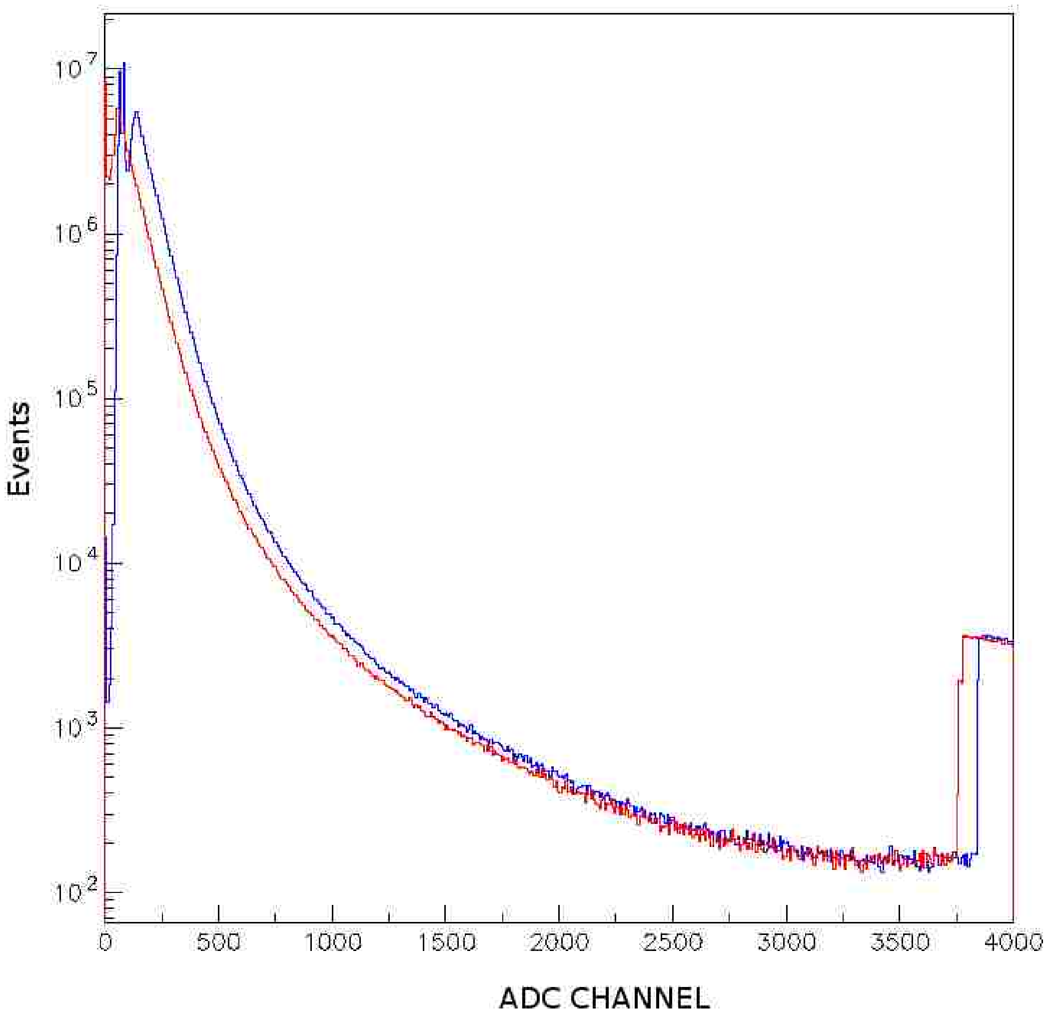

Figure 6.1: The non-pedestal-subtracted spectra (blue) from PMT 1 taken over a 48 hour period. The pedestal is determined by finding the first peak in the first 200 bins. This noise component is then subtracted from the spectra to obtain the pedestal-subtracted spectra (red). The spectra is histogrammed into 500 bins from ADC channel 0 to ADC channel 4000.

counting experiment and a precise energy calibration was not required. Instead, background events were used to ensure detector stability over time.

To accomplish this, a comparison of each individual PMT spectra to the daily average spectra was conducted and then the daily average spectra was compared to a "global" average spectrum. This procedure is described below.

Both ADC A and ADC B pedestal and gain values were calculated for each PMT on a daily basis. This was done by comparison of the individual PMT daily ADC spectrum to the average one from all PMT's on that day. The gain correction factor was determined by minimizing the χ^2 between the average spectrum to that of the individual PMT over the relevant fit interval 1200-1600. This procedure is referred to as the "first stage gain correction."

As an example of this procedure, Figure 6.2 shows the results of the first-stage gain correction for one PMT for data taken on 14 November, 2007. From the figure, one can observe that the original pedestal-subtracted but non-gain-corrected spectra are gain-corrected to the average of all eight spectra. As expected, the correction is best over the interval for which the minimization procedure is carried out. A graph of the first-stage gain correction factors over the approximately 6 month experiment is presented in Figure 6.3. As shown, the corrections range from ≈ 0.8 for PMT 4 to ≈ 1.5 for PMT 7.

To equalize the detector response over the lifetime of the experiment and to correct the difference between ADC A and ADC B, a second stage gain correction was also performed. In this procedure, each summed prompt spectra was compared to the "global" average summed prompt spectra. The "global" average spectra was determined by taking the average of all daily summed prompt spectra for the 115 days of data.

This correction factor is the factor which multiplies the first stage gain correction factors to minimize the χ^2 in each days total prompt spectra with respect to the number of events in the "global" average total prompt spectra over the selected fit range (ADC value 3600 to ADC value 4000). Figure 6.4 shows an example of the resulting spectra following the second stage gain correction procedure for 14 November 2007. In the figure, the average daily spectrum (blue) was initially lower than the average "global" spectra (black). However, when multiplied by a gain correction factor of 1.045, the 'global' and the second-stage corrected spectra (red) match well over the fit interval. Figure 6.5 is the graph of all second-stage gain correction factors. As expected, the average of the gain correction factors is almost unity.

Unless otherwise state, all analysis was conducted with pedestal-subtracted and gain-corrected data.

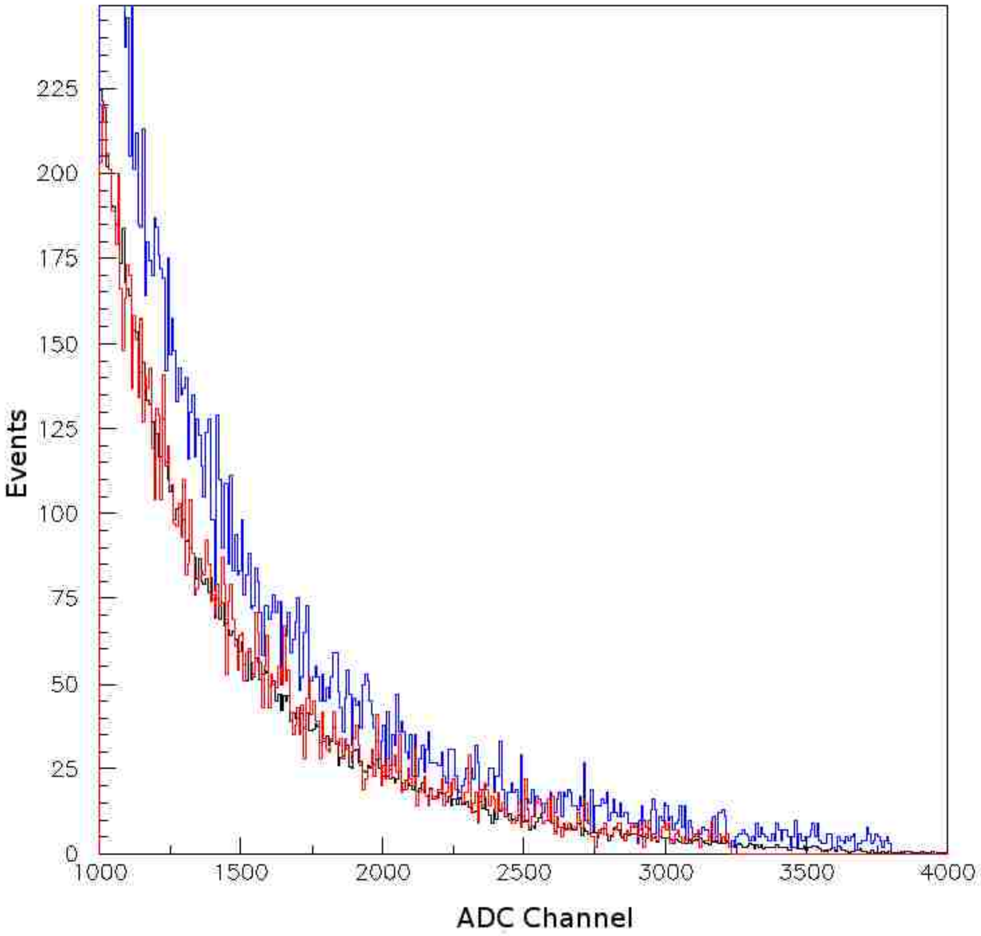

Figure 6.2: Histogram showing the result of the first-stage gain correction procedure for 14 November, 2007 for PMT 4. The non-gain-corrected pedestal-subtracted prompt ADC A spectra are shown in blue. The average spectra of all eight pedestal-subtracted prompt ADC A spectra are shown in black. The first-stage gain corrected spectra are shown in red.

6.3 The Interevent Time Distributions

After the pedestal subtraction and gain correction procedures are performed on each of the daily spectra, additional cuts are applied to further reduce the data. These cuts are:

- Events with any individual PMT having very low ADC values (<10) are not used.
- To further reduce muon events, any event pair where the *summed* prompt and/or delayed PMT ADC values are very high (>13000) is eliminated.

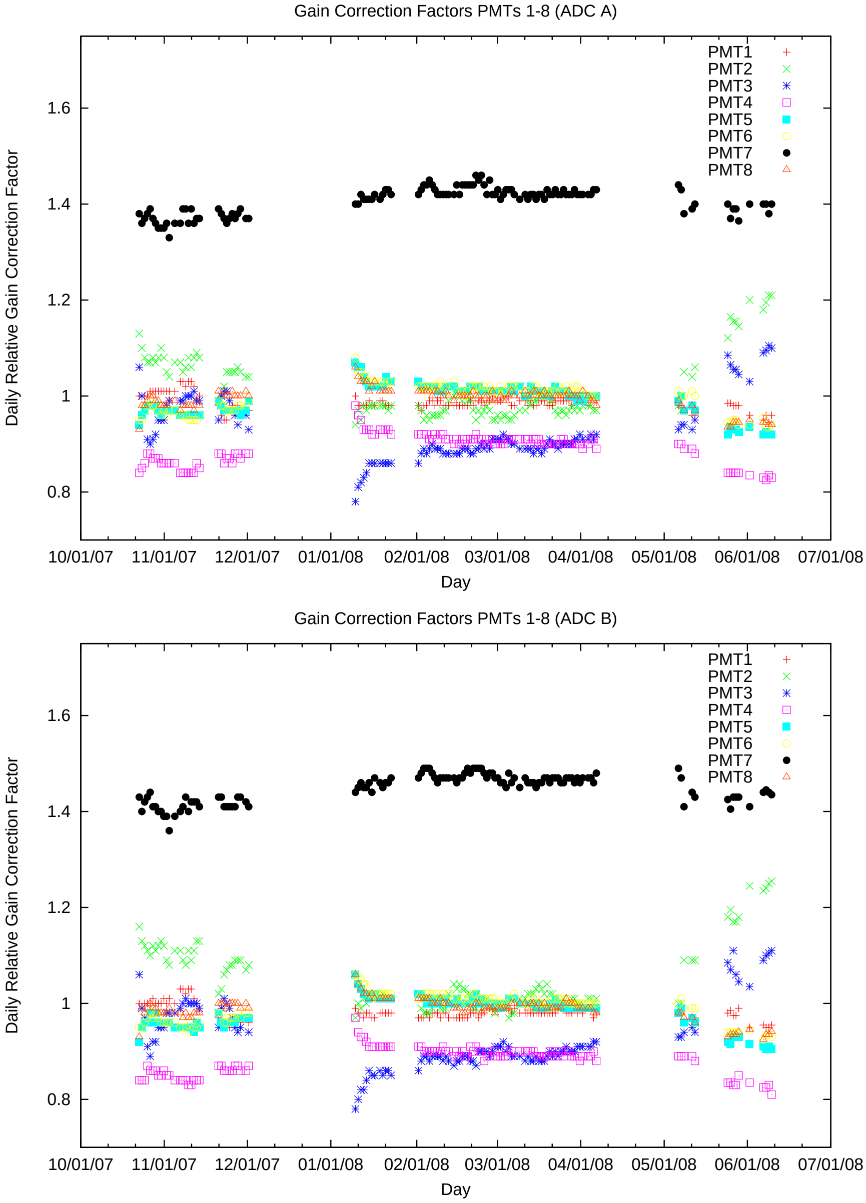

Figure 6.3: The first stage gain-correction factors for PMTs 1-8 for the prompt ADC A signals (top) and the for the prompt ADC B signals (bottom).

- Events occurring with tmu-p less than 100 μs are eliminated in order to be certain that events correlated with muon hits in the veto are not considered in the interevent spectra.
- Events with an uneven PMT light distribution are eliminated. This is done by defining a ‘charge-balance’ parameter which measures how evenly light is distributed among the

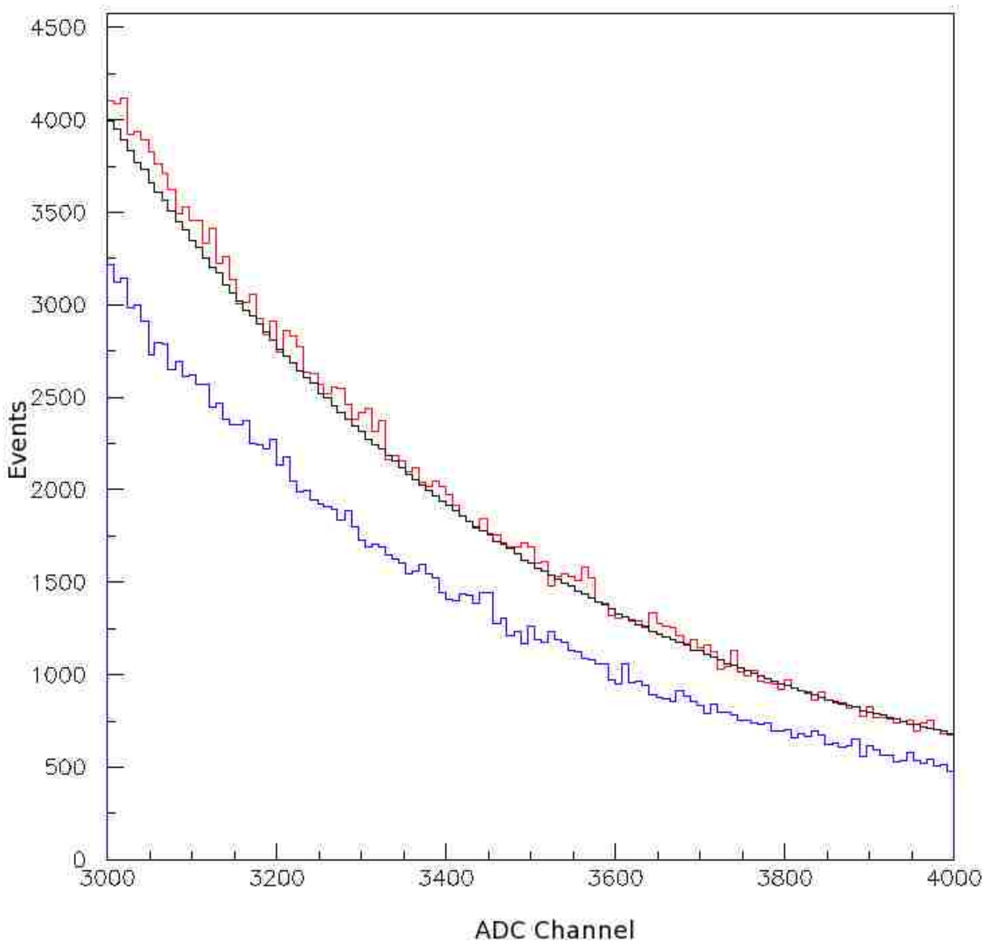

Figure 6.4: The first-stage gain corrected average summed prompt spectra (blue), the first stage gain corrected summed prompt spectra averaged over all 115 days of data (black), and the resulting summed prompt spectra after performing the second-stage gain correction (red) for 14 November, 2007.

8 PMTs. The equation which defines this parameter is:

$$\sqrt{\frac{\sum_i p_i^2}{(\sum_i p_i)^2} - 0.125}$$

where $p1$, $p2$ ... etc. are the prompt PMT signals. The charge balance is 0 for a perfectly uniform light distribution and increases as the light distribution becomes less uniform. In this analysis, events with ‘charge balance’ greater than 0.4 are eliminated.

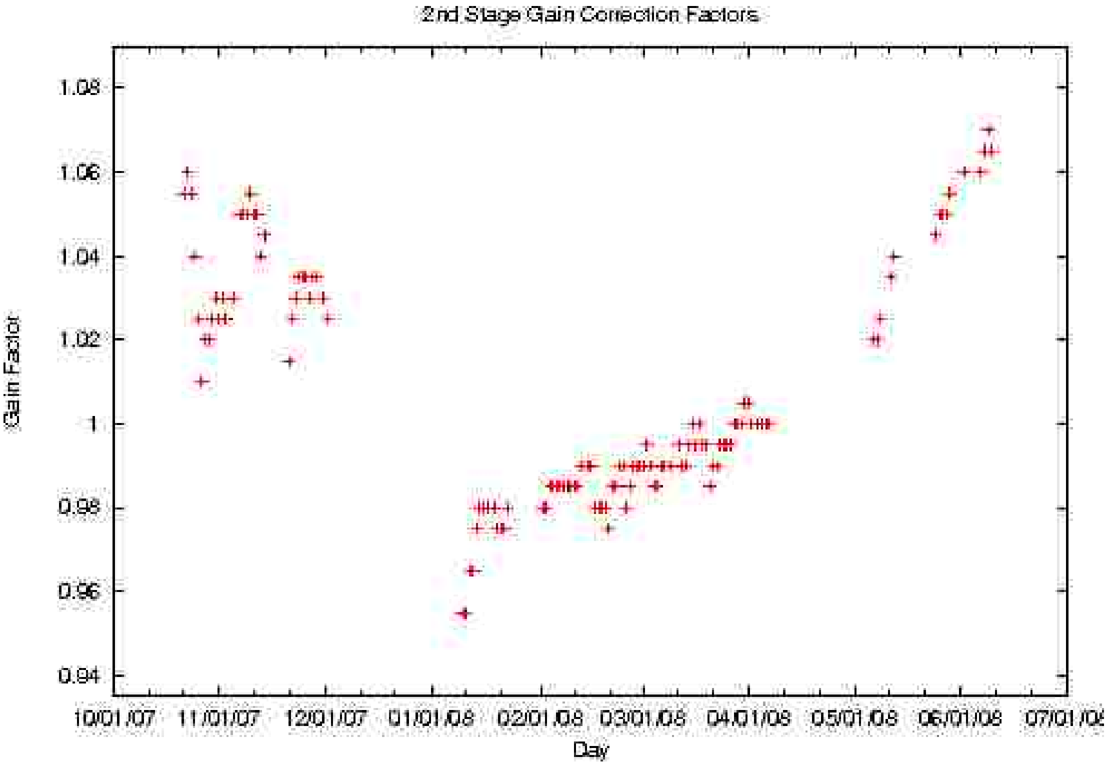

Figure 6.5: The second stage gain-correction factors over the course of the experiment.

- Threshold energy (ADC) cuts for the summed prompt and delayed PMT spectra are applied to optimize the signal to background ratio. The specific ADC cuts implemented will be discussed in detail in Section 6.5.

The interevent time distributions are expected to contain two clear exponential features[157]. The first exponential is due to correlated pairs of events which may be due to antineutrino events or correlated neutrons or correlated gamma rays and neutrons. As described previously, these are a prompt energy deposition followed by the capture of a neutron on a Gd nucleus. This time should be approximately 30 μs. The second exponential which dominates the interevent time distribution at long interevent times (> 100 μs) is due to random coincidences of sequential events. The time constant of this exponential is equal to the inverse of the acquisition trigger rate.

This second exponential can be used to determine the detector hourly livetime and to normalize the daily interevent time distributions. The livetime is calculated by multiplying the total number of events during an hour by the inverse of the hourly trigger rate, i.e.

the uncorrelated time constant. Figure 6.6 shows the histogram of calculated livetimes determined for each of the approximately 2800 hours analyzed. The average hourly detector livetime was 93.8 ± 0.4%. Ten hours had livetimes of less than 90.0% and one hour had a livetime greater than 95.5%. These hours were considered outliers and were not included in the analysis.

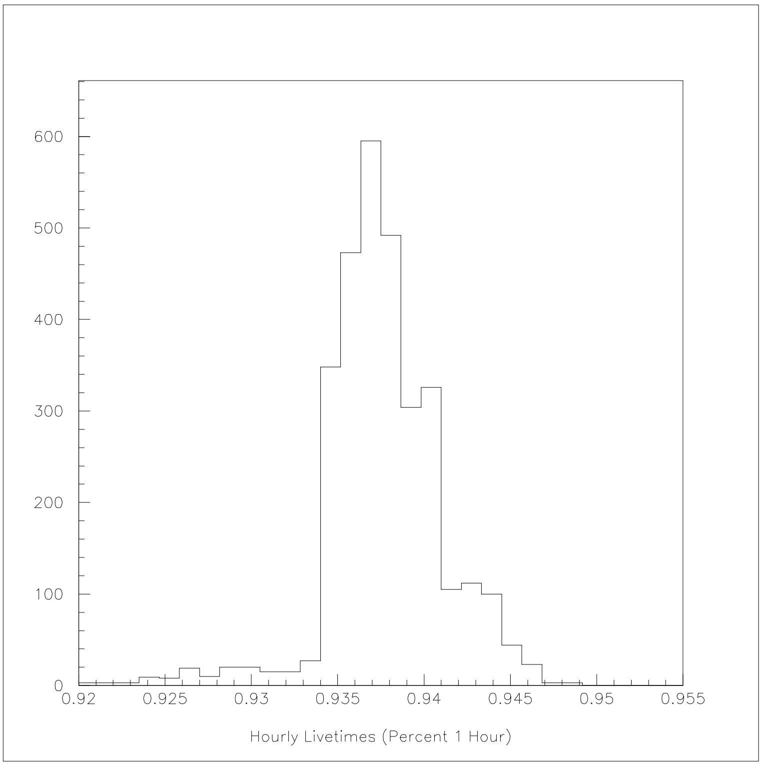

Figure 6.6: Hourly livetimes for 2760 hours.

Using the hourly livetimes, the average livetimes for each day were calculated for comparison and for normalization of the daily interevent time distributions. Figure 6.7 shows the evolution of the daily livetimes over the entire data taking period.

6.4 Detector Stability

The measurement undertaken here is a count of antineutrino events and it does not rely on an absolute determination of the energy spectrum. The only requirement is that the detector response be stable over time. To check that the result of the two stage gain correction

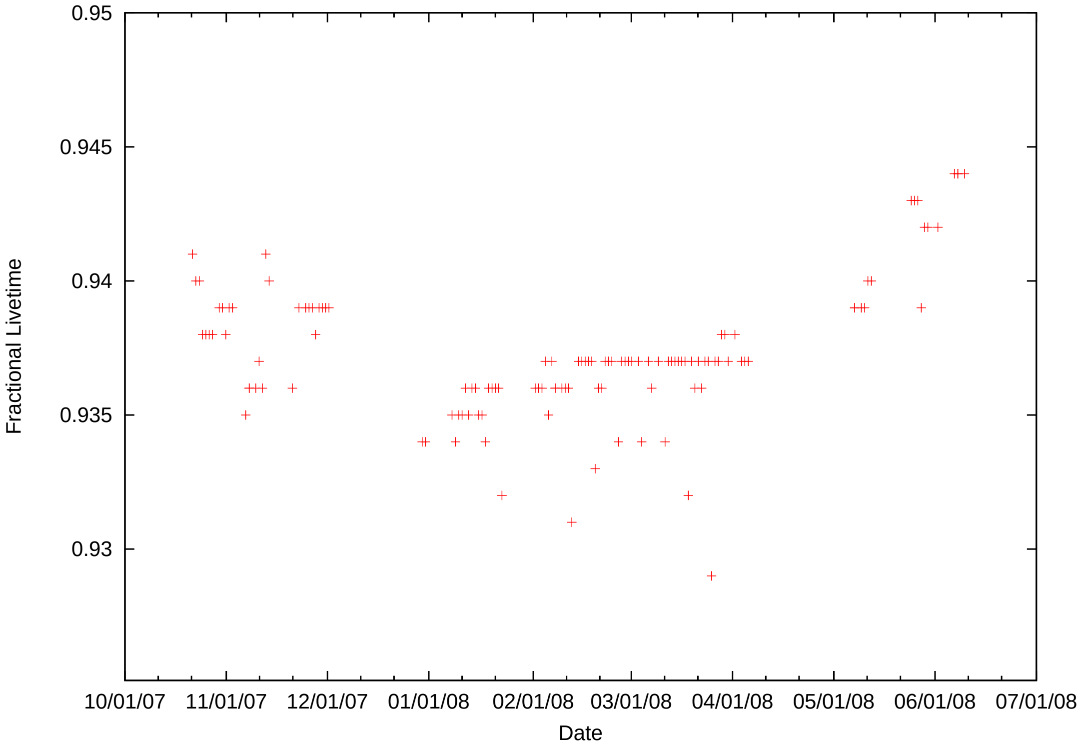

Figure 6.7: Hourly livetimes (fraction of 1 day) over the duration of the experiment. Note: The plot does not include two days of data for which the livetime was less than 0.90. These days were not included in the analysis.

procedure results in a relatively flat detector response, the number of events passing a given threshold criteria was determined for each day over the duration of the experiment. The results are shown in Figure 6.8. The assumption is that the background level should be constant. The points shown in blue are the events passing the stated thresholds after the first stage gain correction and the data shown in red are the events passing the thresholds after the performing both stages of gain correction.

Two features in Figure 6.8 are obvious. First, the first stage gain correction alone is not sufficient to flatten the detector response. Second, there are three periods of significant gain change. However, scalar data recorded during this period indicates no significant change in the recorded detector singles rate. Furthermore, no physical changes in the detector configuration were recorded during this period.

However, from Figure 6.8 it is also clear that performing the second stage gain correction flattens the detector response significantly and improves both the day to day variation in

Table 6.1: Columns 1-4 show the mean and standard deviation of the number of events at each threshold for the entire 233 day data-taking period, and the mean number of events over each of the three time intervals for which the events passing the threshold criteria observed in Figure 6.9 vary significantly. The last column indicates the corresponding systematic error associated with detector stability.

	Mean Number of Events in Interval				
Threshold	233 Day Mean (Std.Dev.)	10/22/07 - 12/02/07	12/30/07 - 04/06/08	05/08/08 - 06/10/08	% Error
1500/1650	8047 (217)	8191 (156)	7954 (188)	8047 (217)	3.6%
1750/1650	3234 (106)	3291 (86)	3189 (86)	3362 (84)	5.4%
1850/1650	2405 (81)	2443 (69)	2373 (66)	2496 (75)	5.1%
2000/1650	1702 (72)	1730 (53)	1670 (52)	1819 (49)	8.8%

the number of events passing the threshold criteria and also ameliorates the discontinuity occurring during the SONGS shut-down.

To check this result at other thresholds and to quantify the extent to which the second stage gain correction procedure flattens the detector response, the events passing four other threshold combinations were determined. The results are provided in Figure 6.9. Linear fits to each data set reveal that the curves are relatively flat (slopes consistent with zero) from Day 1 (22 Oct, 2007) to Day 233 (10 June 2008), the last day of data considered in the analysis[3]

However, despite the gain correction, there still remain three distinct periods of data discernible in the Figure 6.9. These correspond to the periods 22 October - 02 Dec 2007, 20 December 2007 - 06 April 2008, and 08 May -10 June 2008. As presented in Table 6.1, distinctly different mean values for the events passing threshold criteria are associated with each of these three data taking periods. A measure of the systematic error associated with system stability can be determined by calculating the variation in the event rate for these three periods. The difference of the smallest mean value and largest mean value is divided by the mean value for all 233 days. The results are provided in Table 6.1. From the table, it is seen that the systematic error is smallest for the smallest thresholds.

---

[3] As seen from the figure, there were periods when no data were recorded.

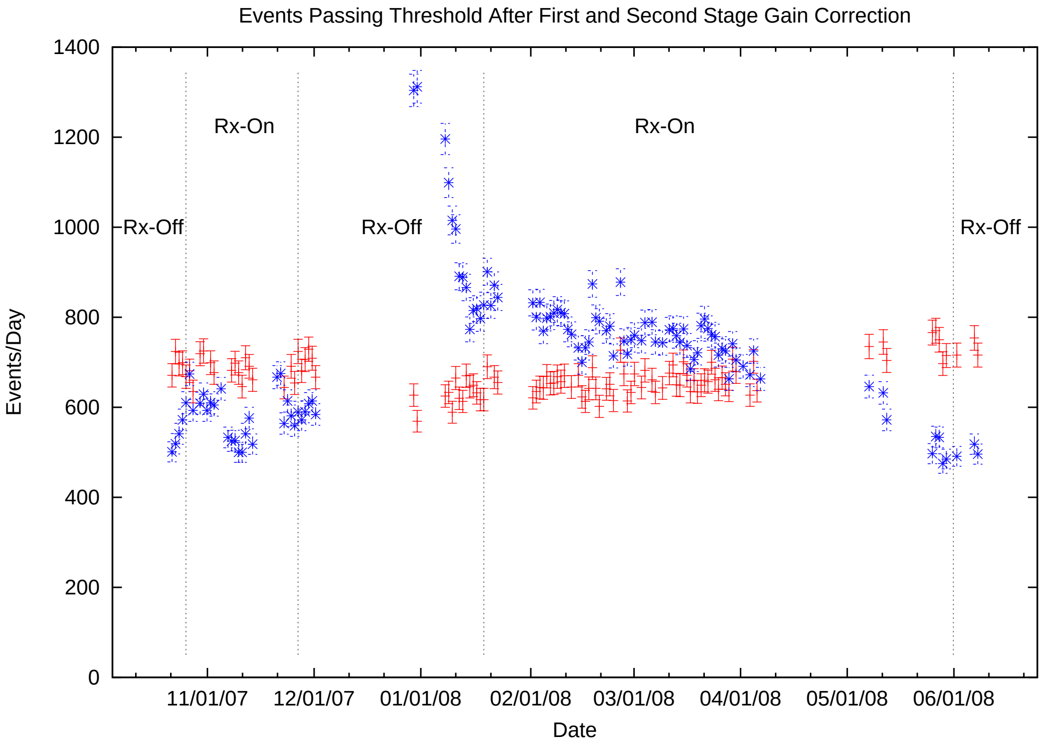

Figure 6.8: For threshold prompt 2000/delay 2000, no saturation, and tmu $> 100\mu$s, the first stage gain corrected events per day passing threshold (blue) and the second-stage gain corrected events per day passing threshold (red). The second stage gain correction is done to the average spectra for 115 days.

6.5 Selection of Optimum Threshold Cuts

A two-part strategy was used to determine the best ADC threshold cuts. First, two features in the ADC spectrum (Figure 6.10) were identified. The peak is due mostly to background gammas from 2.6 MeV ^{208}Tl and 1.4 MeV ^{40}K. Below the knee in the spectra, the events are mostly from cosmic rays, Michel electrons and neutron capture events. These are the events to which the detector must be sensitive. The optimum prompt threshold cut is at a point in the spectra just above where the ^{208}Tl and ^{40}K events begin to die out.

Except for the thresholds described in Section 3 of this chapter which restrict outlier events, no upper thresholds are applied since no physical consideration in the data supports doing so absent an energy calibration[4].

---

[4] With energy calibration an upper threshold of 9 MeV could have been chosen for the prompt events since there are expected to be very few energy depositions due to reactor antineutrinos with energy greater than this. For the delayed event, an upper threshold of around 8 MeV could have been applied based on the

A handle on the best prompt threshold to use can be obtained by investigating the average number of events per day passing ADC threshold criteria. To accomplish this, the average number of events passing threshold were determined for several fixed delay threshold values as the prompt threshold was allowed to vary. Figure 6.11 shows the results. For each fixed delay ADC threshold, the figure indicates a "knee" below which (i.e. at greater prompt threshold values) the rate of change of events passing the threshold criteria per change in prompt threshold is markedly reduced. This value occurs at approximately ADC value 1850 for all four thresholds. Therefore, the prompt ADC threshold cut was set to this value.

To determine the optimum delay cut, the threshold which maximizes the ability to detect neutrons is chosen. The number of correlated and uncorrelated events was determined by performing an integration over the interevent-time distributions at the prompt ADC thresh-

---

maximum energy released by neutron capture on Gd.

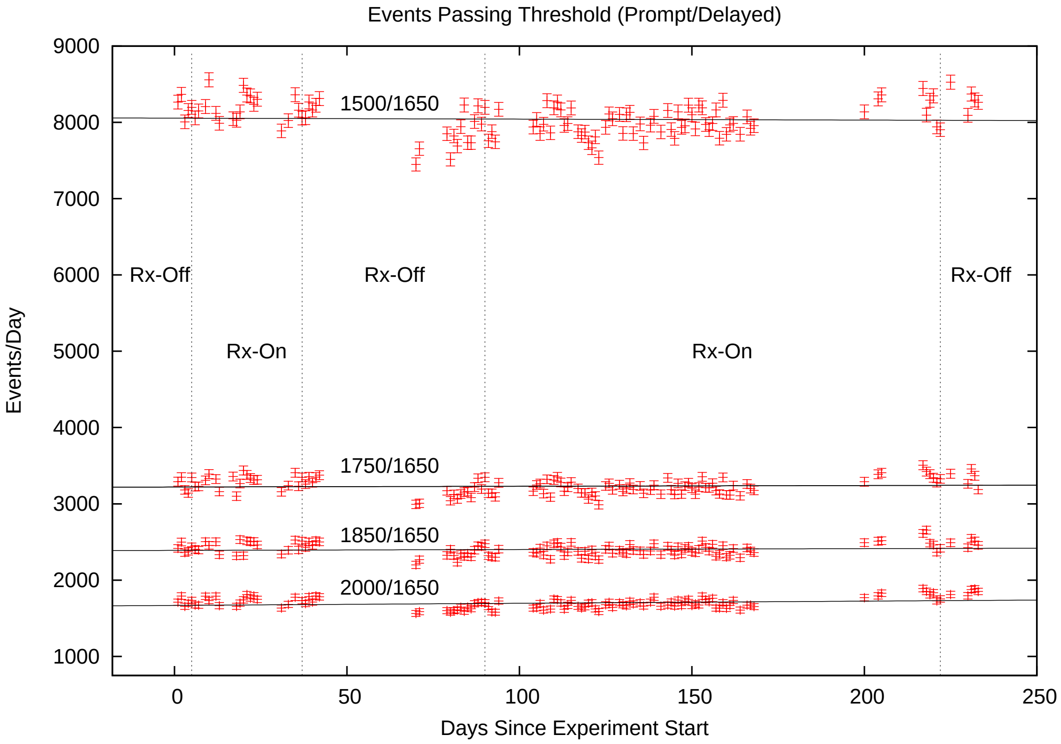

Figure 6.9: For each of the four threshold combinations (the stated ADC prompt/delay threshold with no saturation, and tmu $> 100\mu$s), the second-stage gain corrected events per day passing threshold. Linear fits result in the following slopes (events/day/day): 1500/1650: -0.12 ± 0.32; 1750/1650: 0.10 ± 0.16; 1850/1650: 0.12 ± 0.12; 2000/1650: 0.28 ± 0.10.

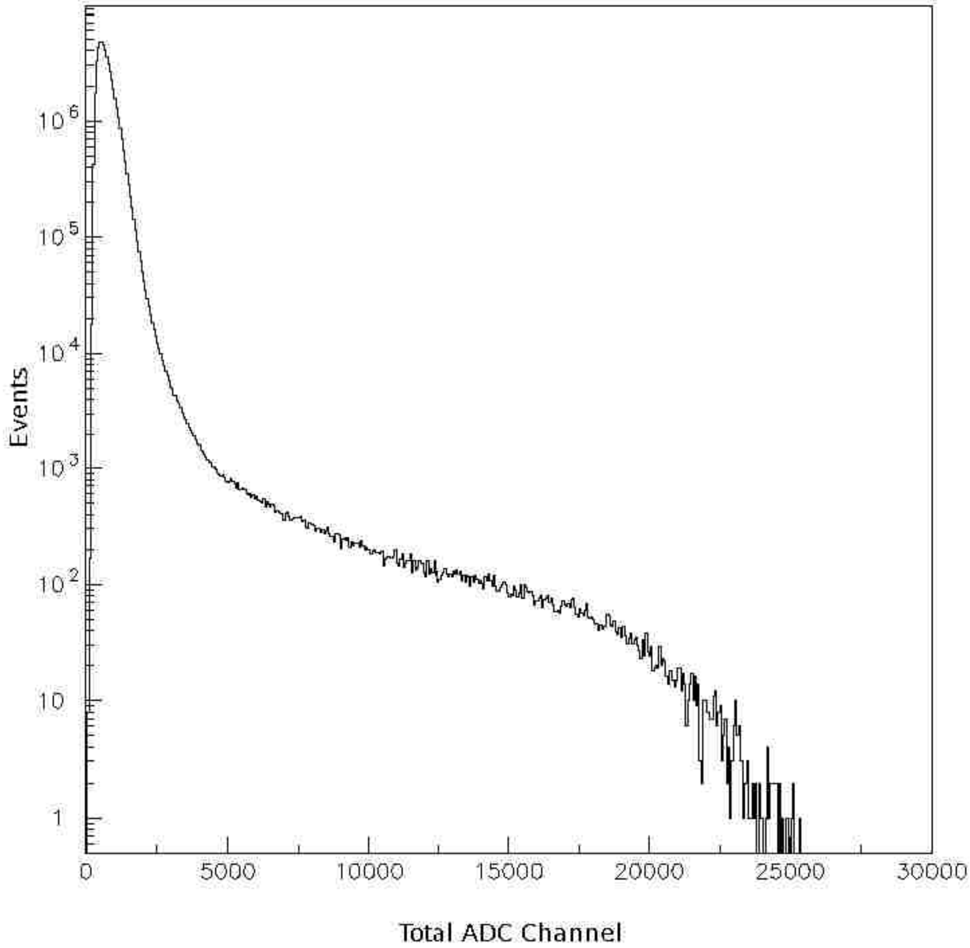

Figure 6.10: The summed prompt ADC spectra.

old established in the previous paragraphs: 1850, and at six equally spaced delay ADC thresholds: 1550, 1650, 1750, 1850, 1950, 2050. To perform the integration, the decay constant (and uncertainty) of the accidental coincidences of the interevent time distribution was determined by fitting a nine day sub-sample of the reactor-on data to a single exponential over the interval 250-4500 μs for each ADC threshold combination.

This interevent time interval can be well fit by an exponential over the lifetime of the experiment and should not change. This was verified to be the case by comparing the uncorrelated decay constant for both the 88 days of reactor-on data and for the 27 days of reactor-off data. These values are consistent with the value determined for all 115 days of

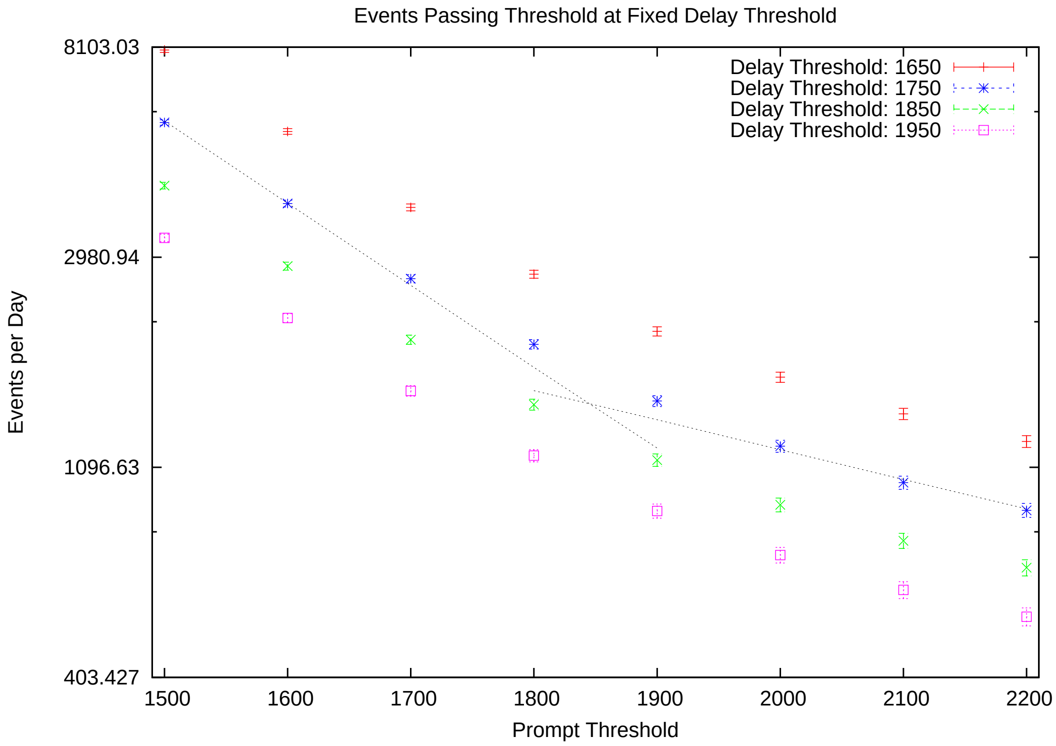

Figure 6.11: The average events/passing threshold for fixed delay threshold for ADC values 1650 (red), 1750 (blue), 1850 (green) and 1950 (purple).

data ($6.324 \pm 0.003 \times 10^{-4}$ μs) to within the uncertainty in the fit. The fit was performed using the CERN MINUIT[163] package interfaced with PAW.

With the decay constant for the accidental coincidences thus fixed, the total interevent time distribution was fit at each of the listed threshold combinations to the sum of 2 exponentials using three free parameters, i.e.

$$f(t) = Ae^{-bt} + Ce^{-dt}, \tag{6.5.1}$$

where A, b, and C are allowed to vary.

From the fit, the fit parameters $\mathrm{A} \pm \sigma_{\mathrm{A}}$, $\mathrm{b} \pm \sigma_{\mathrm{b}}$ and $\mathrm{C} \pm \sigma_{\mathrm{C}}$ are obtained. The number of correlated, n_s, and uncorrelated, n_b, events are calculated by integrating the first exponent and second exponent respectively in f(t) over the interval 10-100μs where

$$n_s = \int_{10\mu s}^{100\mu s} Ae^{-bt}dt = \frac{A}{b}(e^{-b*10\mu s} - e^{-b*100\mu s}) \tag{6.5.2}$$

$$n_b = \int_{10\mu s}^{100\mu s} Ce^{-dt} dt = \frac{C}{d}(e^{-b*10\mu s} - e^{-d*100\mu s}). \tag{6.5.3}$$

With estimates for the number of correlated and uncorrelated events thus obtained, the signal significance,

$$\frac{n_s}{\sqrt{n_s + n_b}}, \tag{6.5.4}$$

can be examined to find the delay threshold which optimizes the detection of correlated events.

Table 6.2 lists the signal significance for the six threshold combinations at the prompt threshold ADC value of 1850 for the nine day sub-sample of reactor-on data. As can be seen, the significance is higher for the lower delay ADC values which suggests that more correlated events are observed at the lower delay ADC values even at the price of increased background. Specifically, the significance peaks for the threshold values prompt:1850/delay:1650. For this reason, a delay ADC threshold cut of 1650 was established.

Table 6.2: The signal significance, $n_s/\sqrt{n_s + n_b}$, for the nine days sub-sample data at 6 ADC threshold combinations.

Signal Significance (9 Days sub-sample Data)						
Prompt Threshold	Delay Threshold					
	1550	**1650**	**1750**	**1850**	**1950**	**2050**
1850	18.7σ	20.2σ	17.6σ	17.5σ	17.1σ	16.6σ

6.6 Determination of the Correlated Signal

Experiments which impose selection criteria, i.e. cuts, are especially prone to the introduction of unintentional bias. To avoid "tuning" the analysis, only a small sample of the reactor-on data was used to determine the cut criteria. Neither the remaining reactor-on data nor the reactor-off "data-box" was opened until the thresholds were established and the method of analysis had been determined. Additionally, two separate analyses, designated the Parametric Fit Method and the Counting Method in the descriptions that follow, were performed to determine the correlated signal. Each of these methods have different associated systematic errors, advantages and disadvantages. As will be shown, the advantage of the Parametric Fit Method is that it is not very sensitive to the parameters used in the analysis. The major disadvantage of this method is that it assumes the shape of the signal. On the other hand, the Counting Method does not assume a shape in the signal but can be sensitive to the imposed time cut.

6.6.1 The Parametric Fit

Figure 12 shows the interevent time for the 79 days of reactor-on data not used in determining the delay ADC threshold. The two expected exponential features are clearly seen.

It is impossible in this detector to distinguish random coincidences from true correlated event pairs on an event-by-event basis, rather, a statistical separation of random coincidences and correlated pairs was performed to determine the correlated (antineutrino-like) event rate. This is achieved by fitting the spectrum displayed in Figure 6.12 to the sum of two exponentials. The time constants of the exponentials are determined in advance. The uncorrelated rate was measured using the whole 115 day data set (after the thresholds were fixed) by fitting an exponential over the interval 250-4500 μs as previously described. With the uncorrelated decay constant thus fixed, the correlated decay constant, the reciprocal of the neutron capture time, was determined by fitting the total interevent time distribution for all 115 days of data over the interval 10-4500 μs using Equation 6.5.1 with *three* free parameters as in the determination of the delay ADC threshold. The value for the correlated time constant from the fit was $0.032 \pm .001$ μs^{-1} which corresponds to a neutron capture time of 31.3 ± 0.9 μs. This is consistent with the ≈ 30 μs capture time of thermalized neutrons obtained by SONGS I for liquid scintillator doped to the level of 0.1% Gd (0.2% $GdCl_3$) [157].

With both decay constants fixed, we need only fit for two parameters, the amplitude of each exponential. Simple integrals,

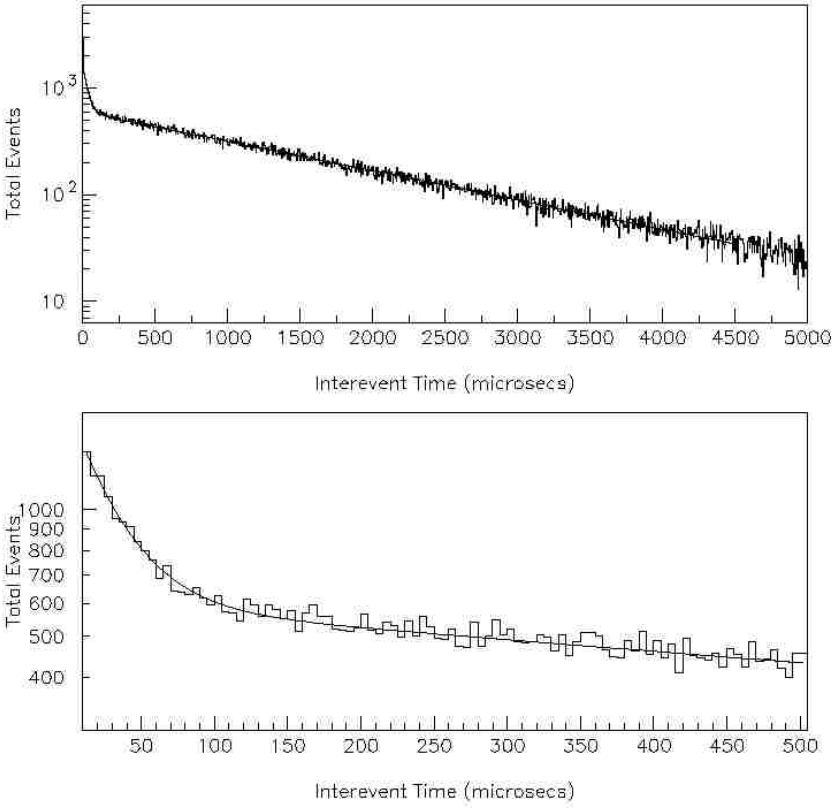

Figure 6.12: The interevent time distribution at prompt/delay threshold 1850/1650 for all 79 days reactor-on data considered in determination of the reactor-on correlated events. The solid fitted line is to the sum of two exponentials with two free parameters. The correlated and uncorrelated decay constants are fixed to 0.032 μs^{-1} and 6.32×10^{-4} μs^{-1} respectively.

$$N_{\text{corr}} = \int_{10\mu s}^{x} Ae^{-bt}. \tag{6.6.5}$$

$$N_{\text{uncorr}} = \int_{10\mu s}^{x} Ce^{-dt}. \tag{6.6.6}$$

then yield the number of event pairs that fall into each class over the interevent time interval 10-x μs.

To investigate the validity of the parameter uncertainties returned by the fitting routine, 100 distributions were constructed by sampling the double exponential distribution with the fit parameters from the 9 day reactor-on sub-sample. Each of the 100 distributions contained about 21,000 event pairs; the same as the distribution for the 9 days of reactor-on data. The generated interevent time distributions were then fit using the sum of two exponentials (Equation 6.5.1) with both decay constants fixed. Three of these generated distributions are shown in Figure 6.13.

Additionally, Figure 6.14 shows the results of the one hundred measurements of the number of correlated events from the generated distributions. The values are determined from Equation 6.6.5 using the amplitudes from the two free parameter double exponential fits. Here, the endpoint of the interevent time interval, x, has been set to 65 μs[5]. As expected, the figure shows that the mean of the number of correlated events calculated from the 100 generated interevent time distributions is approximately centered on the value for the number of correlated events calculated from the 9 day reactor-on sub-sample used to produce these distributions. More importantly, the standard deviation of the 100 measurements of the number of correlated events is about 5% which is consistent with the uncertainty calculated for the 9 day reactor-on data (of about 6%). This verifies that the uncertainty in the number of correlated events calculated by using the MINUIT fitted amplitudes really does represent the uncertainty in the number of events.

• Detection of Excess Reactor-On Correlated Events

It is impossible to determine which reactor-on correlated events are due to antineutrinos and which are due to correlated backgrounds. Instead, use must be made of the fact that periodically the antineutrino source, the SONGS Unit 2 reactor, is turned off. There were three such periods comprising 27 full days of data where the reactor was off during the course of the experiment[6]. During these periods the detector counted only correlated background events and a small number of antineutrino interactions from the relatively distant Unit 3 reactor.

---

[5] This interval is chosen for comparison with the results of the 'Counting Method' analysis which will be discussed in the following section.

[6] There were of course additional hours when the reactor was off but when no data was taken. There were also periods when the detector was operating but during which the reactor was ramping up or down and was not at full power. These hours are not included in the analysis.

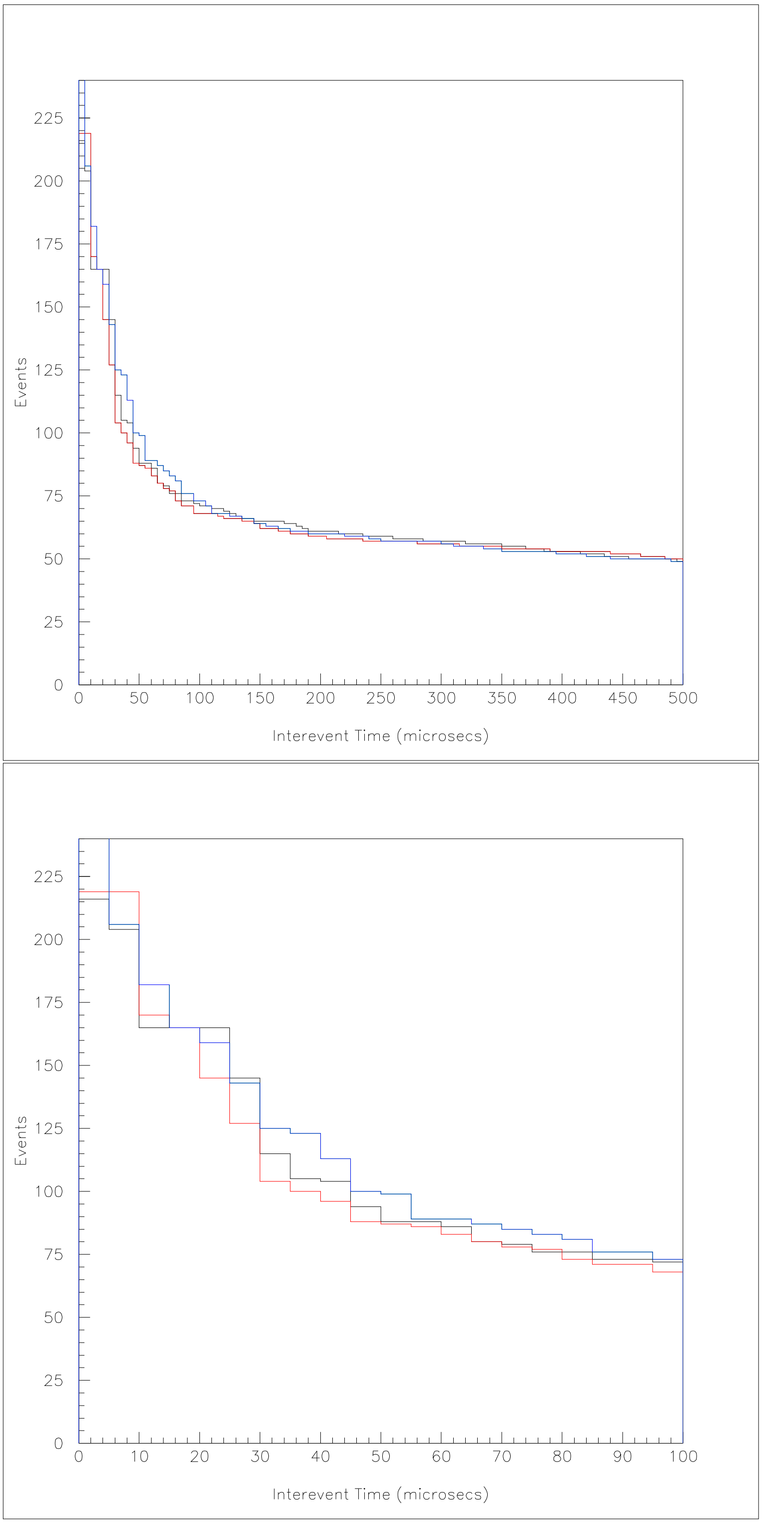

Figure 6.13: Top: Three sample interevent time distributions generated by a toy Monte Carlo from an underlying double exponential function with amplitudes and decay constants taken from the fit of the 9 day reactor-on sub-sample data. Bottom: The same sample interevent time distributions over the interevent time interval 0-100μs.

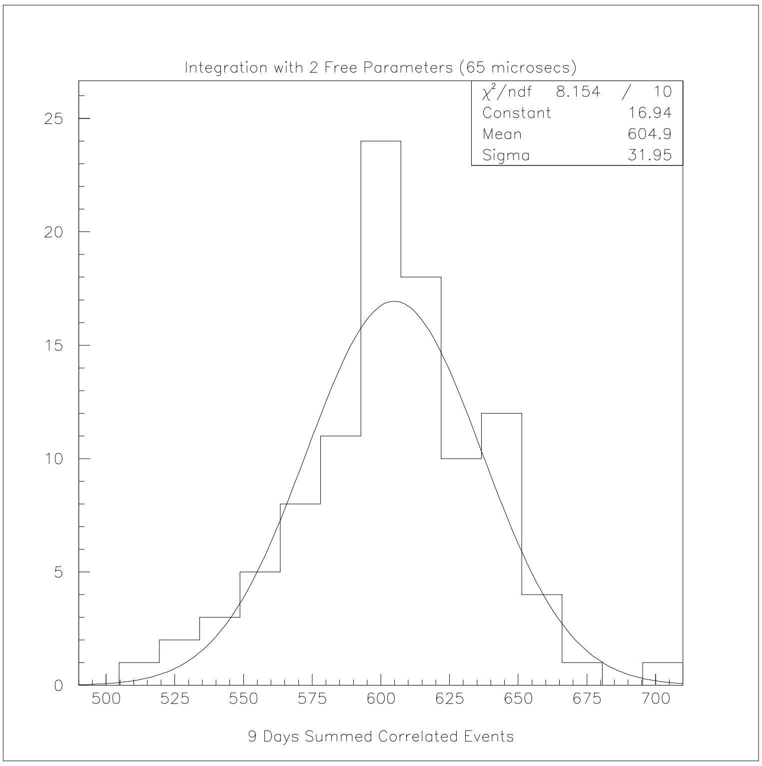

Figure 6.14: One hundred measurements of the number of correlated events calculated via the integration method. The one hundred samples are taken from an underlying double exponential function with amplitudes and decay constants taken from the fit of the 9 day reactor-on sub-sample data. The correlated events are calculated over the interevent time interval 10-65 μs.

Figure 6.15 displays the interevent time distributions normalized per day for 27 days reactor-off and 79 days reactor-on (88 full days total reactor-on data minus the 9 days of sub-sample data). These interevent time distributions represent the data over the entire duration of the experiment. The reactor-off data was taken during periods when Unit 2 was at zero power for scheduled and unscheduled maintenance as verified via SONGS operating logs. Likewise, the reactor-on data represents periods when the reactor was operating at full power.

Fitting the interevent time distributions to the sum of two exponentials with the time constants fixed as described in the previous section and calculating the correlated events passing the selection criteria results in a value of about 67.0 ± 1.5 correlated events/day for the case with the reactor on and 58.5 ± 2.5 correlated events/day for the case of reactor-off

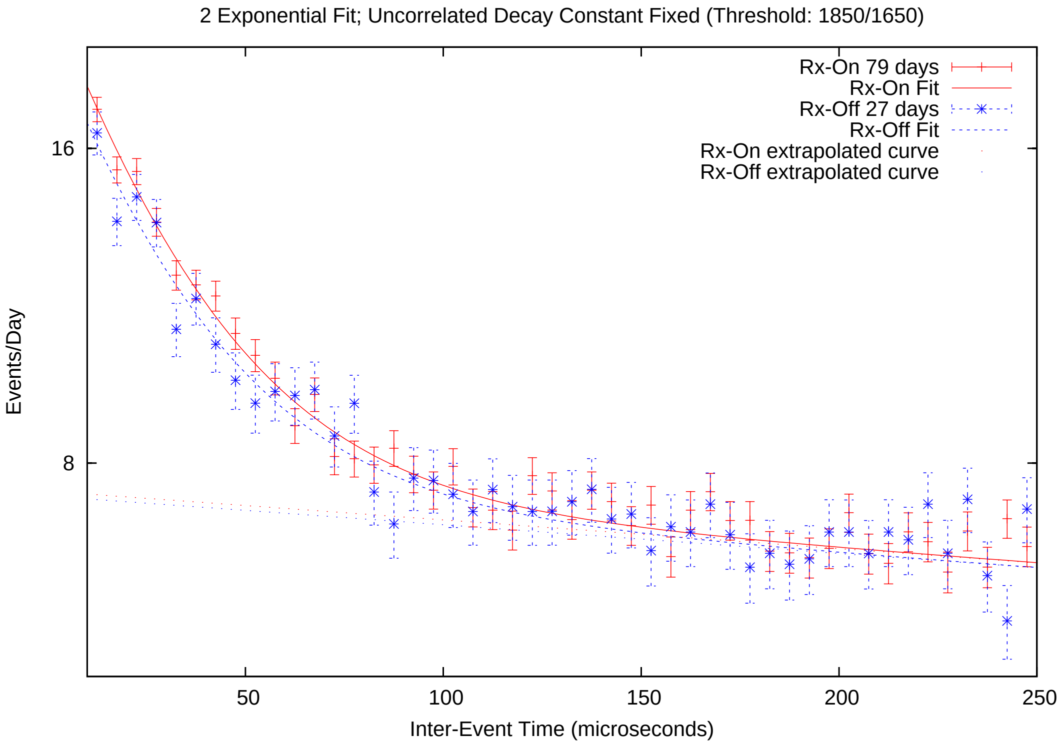

Figure 6.15: The interevent time distributions for reactor-on and reactor-off data at the ADC prompt/delay threshold combination 1850/1650 normalized per day over the interevent time interval 10-250 μs. The bin interval is 5 μs. The fit is performed using the PAW interface to MINUIT to the sum of two exponentials with the decay constants fixed at 0.032 μs^{-1} and 6.32×10^{-4} μs^{-1} and the fit interval is from 10-4500 μs.

over the interevent time interval 10 μs-∞[7]. This is good evidence of more correlated events when the reactor is operating than when the reactor is shut-down. Note also, that the uncorrelated portion of the interevent time spectrum is only slightly altered by the change in reactor state. Table 6.3 provides the fit parameters associated with the sum of the two exponential fit to the reactor-on and reactor-off interevent time distributions and the number of correlated and uncorrelated events per day contained in the spectra.

- **Results of Varying the Fixed Correlated Decay Constant**

The correlated decay constant, which was fixed in the procedure used to obtain the correlated event rate for both cases of reactor on and reactor off, was obtained from the three free

---

[7] The reason the upper limit on the integral is ∞ is because the counting is performed by integrating the exponential.

Table 6.3: From Figure 6.14, the fit parameters of the function $f(t) = Ae^{-bt} + Ce^{-dt}$ fitted separately to 79 days reactor-on data and 27 days reactor-off data where b and d are fixed to .032 μs^{-1} and .000632 μs^{-1} respectively. The resulting integral values for the number of correlated and uncorrelated events over the interevent time interval 10μs-∞. The errors are statistical only.

Comparison of Correlated Event Rates Evaluated over the interval: 0-∞			
Parameter	Reactor-On	Reactor-Off	**On minus Off**
A	1162.6 (26.3)	348.3 (14.9)	-
Corr. Evnts./day	66.8 (1.3)	58.5 (2.5)	**8.3 (2.8)**
C	593.8 (1.5)	200.8 (0.8)	-
Uncorr. Evnts./day	1725.8 (4.2)	1707.7 (7.2)	**18.2 (8.3)**
χ^2 per d.o.f.	1.13	1.09	-

parameter fit of Equation 6.5.1 to the interevent time spectrum for *all data*, reactor-on and reactor-off as this was the highest statistic data set available with a fit uncertainty of only about 3%. However, some effort was taken to determine the neutron capture time directly from the data and fix it in the analysis before opening the data box.

First, an attempt was made to determine this value from a fit to the interevent distribution of *five hours* data resulting from the placement of an Americium-Beryllium gamma-neutron source near the detector. The source was placed approximately 1.5 meters away in order to prevent the increased singles rate from overwhelming the DAQ. Unfortunately at this distance, the chances of obtaining a gamma correlated with a neutron in the detector were relatively small. Nevertheless, even with only five hours of neutron source data, a fit to the interevent time distributions yielded a neutron capture time of the expected magnitude. Fits were performed at several energies (prompt/delay ADC values), however large uncertainties (Table 6.4) were associated with the returned fit values and the neutron capture constant could not be fixed by this method.

An effort was also made to ascertain the neutron capture constant by determining the effect of increased delay thresholds. Since the detector muon veto was not perfectly efficient, unvetoed high energy muons could create multiple neutrons in the detector in close time proximity. The expected effect of these multiple neutrons in the detector would be

Table 6.4: The neutron capture constants resulting from a fit to the sum of a two exponentials for 5 hours of data taken with an AmBe source placed approximately 1.5m from the SONGS detector. Note, these values of the neutron capture constant are not statistically independent.

Neutron Capture Constant from AmBe Fit (μs)	
Threshold (prompt/delay)	**Decay Constant**
1000/1000	32.1 ± 4.4
1000/1750	32.4 ± 6.1
1000/2000	34.2 ± 7.0
1250/1250	35.2 ± 4.3
1250/2000	33.8 ± 7.6
1500/1500	32.3 ± 5.4
1500/1750	29.8 ± 6.3
1750/1750	30.2 ± 6.9
1750/2000	32.6 ± 7.7
2000/1500	27.5 ± 6.6
2000/1750	28.7 ± 7.9
2000/2000	37.8 ± 10.2

to artificially lower the measured interevent time obtained from a fit of the interevent time distribution to Equation 6.5.1. One expects that as one increases the delay threshold, the coincidence detections caused by multiple neutrons will decrease since the probability that all capture on Gd and produce enough light to pass threshold decreases. At sufficiently high delay threshold one expects that neutron decay constant obtained from the fit to yield a consistent value. Figure 6.16 shows the results of this measurement for the prompt threshold ADC value 2000. It is suggestive evidence, although not conclusive proof, of the expected behavior. Note also that the value obtained via this plot (about 31 ± 2 μs) is consistent with the value of 31 μs used in the determination of the correlated signal via the Parametric Fit method.

Finally, to check the sensitivity of the difference in the rate of reactor-on minus reactor-off correlated events to the use of different decay constants, the correlated event rate and significance were obtained using different values. The results of varying this parameter by about 10% are shown in Table 6.5. Clearly, the correlated reactor-on minus reactor-off event rate and the significance of this quantity vary only slightly over this range. That the

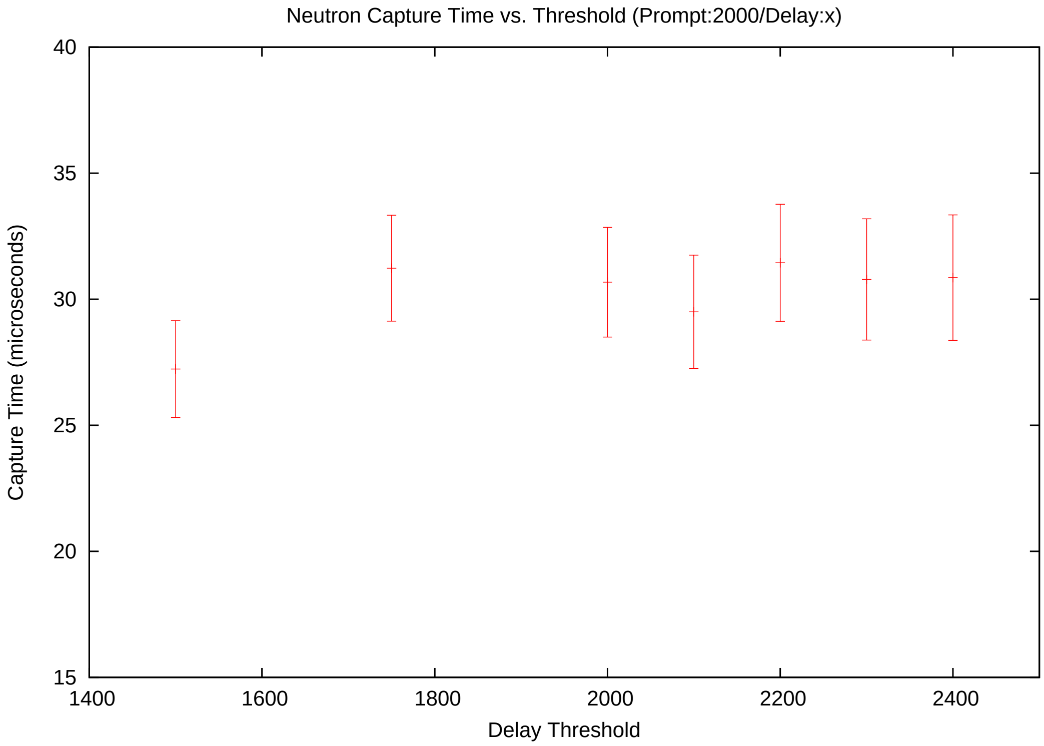

Figure 6.16: The neutron capture time calculated from exponential fits of the correlated component of the interevent time distribution for several prompt threshold equal 2000 and delay threshold given by the x-axis.

final answer is not sensitive to the value chosen for the correlated decay constant[8] provides increased confidence in this method.

6.6.2 The Counting Method

A second analysis to determine the reactor-on minus reactor-off correlated event rate was performed by directly counting the number of correlated events per day after subtracting the non-correlated component from the total interevent time distributions and comparing the reactor-on and reactor-off rates.

The cuts used to generate the interevent time distributions for this analysis are the same as previously described. Specifically, the only ADC thresholds considered were for the ADC values prompt 1850/delay 1650 and also with the cuts stated in Sections 6.1 and 6.3.

---

[8] Values of the decay constant below approximately .020 μs^{-1} and above approximately .045 μs^{-1} begin to show clearly bad fits.

Table 6.5: The reactor-on minus reactor-off correlated events per day calculated from Equation 6.5.1 with a two free parameter PAW fit to the respective interevent time distributions. The uncorrelated decay constant is fixed to the previously obtained value ($6.32 \times 10^{-4}\ \mu s^{-1}$) and correlated decay constant is fixed at the values listed in the table. The interevent time interval over which the integral is calculated is 10μs-∞.

Reactor-On minus Reactor-Off Significance vs. Fixed Correlated Decay Constant	
Fixed Correlated Decay Constant Constant (μs^{-1})	**Correlated Event Rate (Events per Day)**
0.029	$8.5 \pm 3.0\ (2.8\sigma)$
0.030	$8.4 \pm 3.0\ (2.8\sigma)$
0.031	$8.3 \pm 3.0\ (2.8\sigma)$
0.032	$8.3 \pm 2.9\ (2.8\sigma)$
0.033	$8.2 \pm 2.9\ (2.8\sigma)$
0.034	$8.1 \pm 2.9\ (2.8\sigma)$
0.035	$8.0 \pm 2.8\ (2.8\sigma)$

For the subtraction, the amplitude for the exponential corresponding to uncorrelated portion of the spectra, i.e. $Ce^{\text{-dt}}$, was obtained from the two free parameter fit of the total interevent time distribution for the case of reactor-on and reactor-off. Using this value for the amplitude and the fixed uncorrelated decay constant obtained from the fit of all 115 days data at long interevent times ($> 250\ \mu$s), the uncorrelated portions of the spectra were extrapolated into the short interevent time region and subtracted from the total interevent time distributions bin-by-bin. Figure 6.17 shows the resulting distribution of the correlated event reactor-on and reactor-off interevent times.

The errors in the subtraction are treated as follows. The counts in each 5μs bin of the reactor-on and reactor-off interevent time distributions are assumed to be Poissonian, so the uncertainties in each bin of the reactor-on, n_{on}, and reactor-off, n_{off}, interevent time distribution are taken to be the square root of the total number of events (correlated plus uncorrelated) in that bin. The uncertainty of the exponential created to extrapolate the uncorrelated events to short interevent times can be obtained by propagating the uncertainties in the fit parameters which are used to create the function. Since the decay constant is fixed, the uncertainty in the function is only due to the error in the amplitude. From Table 6.6, these uncertainties are 0.3% for reactor-on and 0.4% for reactor-off. These are small in comparison with the uncertainty of n_{on} and n_{off}.

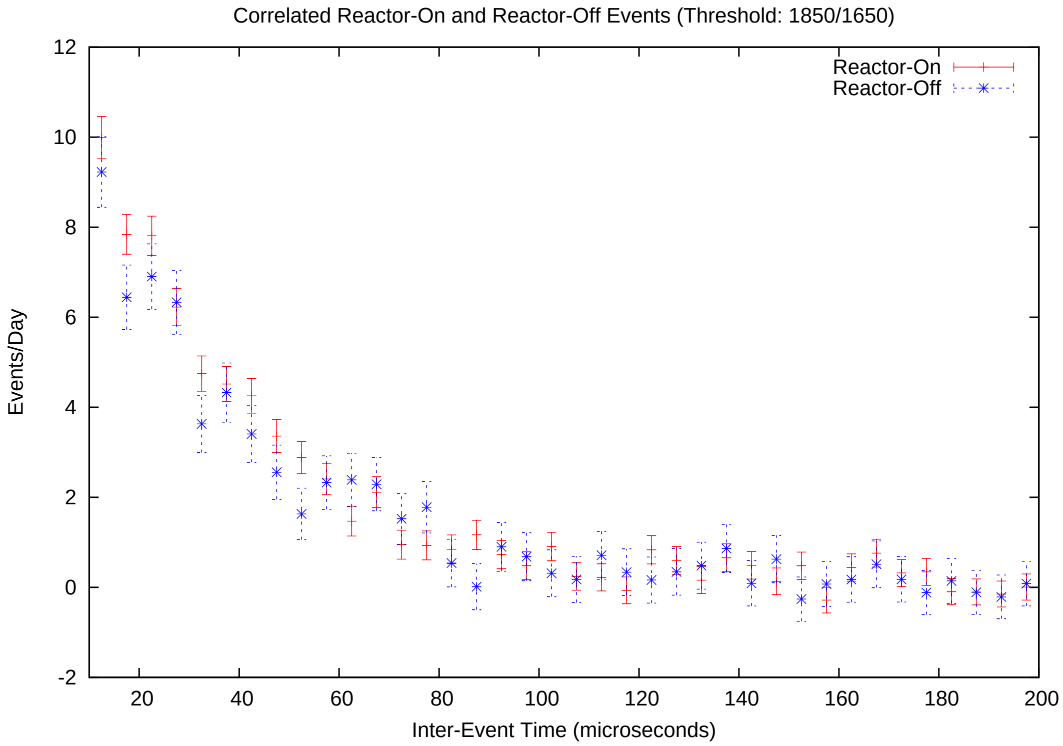

Figure 6.17: For ADC threshold 1850/1650, the reactor-on and reactor-off correlated event interevent time distributions resulting from subtracting the accidental coincidences from the total interevent time distributions. Specifically, the function $200.76 \times e^{(-6.32 \times 10^{-4} t)}$ has been subtracted from the total reactor-off interevent distribution and the function $593.8 \times e^{(-6.32 \times 10^{-4} t)}$ has been subtracted from the reactor-on interevent distribution.

If now, the number of reactor-off correlated events is subtracted from the number of reactor-on correlated events over some time interval, a direct determination of the reactor-on minus reactor-off correlated event rate can be obtained. Before this can be accomplished however, an interevent time cut must be applied. That is, one must decide what interevent time interval gives the best conditions for determining the signal. This cut was not needed in the previous analysis because in that case the area under the exponential was obtained. For the counting method this cut is crucial.

- **Determination of the Interevent Time Cut**

To get a handle on the question of the best interevent time cut to use, the signal significance can be calculated for several interevent time intervals to find the time interval at which the correlated event signal significance is greatest. However, an easier way to find the optimum interval at which to implement a time cut which maximizes sensitivity to the correlated event rate is to use a computational software program like Mathematica.

One can integrate Equation 6.5.1 to obtain the number of correlated and uncorrelated events over a specified interevent time interval. From these values, one can then calculate an expression for the signal significance (SS), $\frac{n_s}{\sqrt{n_s+n_b}}, SS = \frac{A(0.7-e^{-bt})}{\sqrt{A(0.7-e^{-bt})+C(1-e^{-dt})}}$, (6.6.7)where $A = 4864.9$, $b = 0.037\ \mu s^{-1}$, $C = 101201.8$ and $d = 6.32 \times 10^{-4}\ \mu s^{-1}$ are the values for amplitude and decay constants from the 9 days reactor-on data. One can then simply find the value that maximizes this expression. Figure 6.19 shows a plot of the function described by Equation 6.6.7. The interevent time value that maximizes Equation 6.6.7 is 65 μs. Accordingly, this time cut was established prior to examining the 27 days reactor-off data.

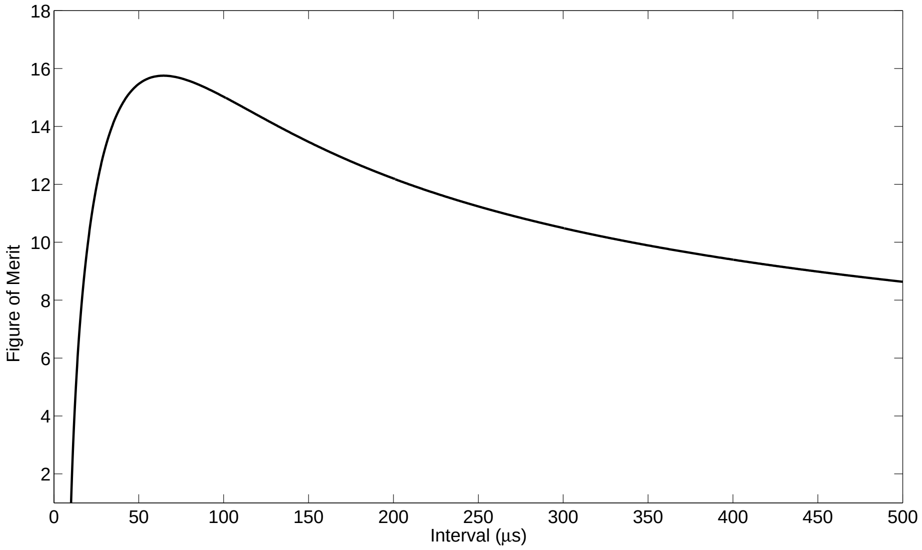

Figure 6.18: Correlated Event Detection vs. Interevent Time Cut

Using this time cut, the 100 distributions of interevent times which were previously generated from the 9 days of reactor-on sub-sample data using a toy Monte Carlo for the purpose of verifying the errors on the amplitude (Sec.6) were also investigated using the counting method. From the generated interevent time distributions, a count of the number of reactor-on correlated events for each interevent distribution was made after subtracting

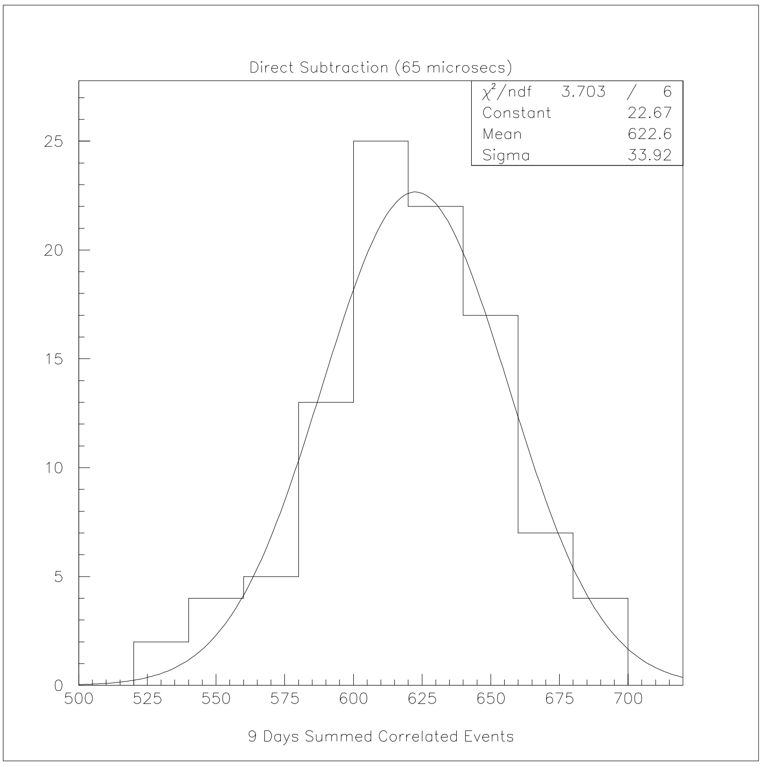

Figure 6.19: This figure shows the result of the counting method performed on the 100 interevent time distributions generated from the interevent time distribution taken from the 9 days of sequestered data. Each interevent time distribution is fit at long interevent times to a single exponential with a decay constant of 6.32×10^{-4} μs^{-1}. The amplitude is determined from the fit and the exponential is extrapolated to short interevent times and the subtracted from the original distribution over the interval 10-65 μs.

the accidental coincidences following the procedure described above. Figure 6.18 shows the results of one hundred direct counts of the correlated events per day after subtracting the accidental coincidences from the total interevent time distributions. From the figure it is seen that the mean number and standard deviation of the number of correlated events obtained via the direct count (622.9 ± 33.9) are consistent with the number obtained using the Parametric Fit Method over the same interevent time interval (604.9 ± 32.0). This suggests that the counting method with a time cut of 65μs should be approximately as sensitive to determining correlated events as the exponential fit method.

Once the reactor-off data was opened, the correlated reactor-on (79 days) minus reactor-off (27 days) event rate determined via the counting method was determined. The result is **7.1 ± 2.5 events/day**. Table 6.6 provides the correlated reactor-on event rate, the

Table 6.6: Bin-for-Bin subtracted reactor-on minus reactor-off correlated events. The errors are statistical only.

interval(μs	$\mathrm{r_{on}}$/day (δr_{on})	$\mathrm{r_{off}}$ (δr_{off}/day)	$\mathrm{r_{on\text{-}off}}$/day ($\delta\mathrm{r_{on\text{-}off}}$)
10-15	9.98 (0.47)	9.17 (0.78)	0.81 (0.91)
15-20	7.83 (0.44)	6.27 (0.71)	1.56 (0.84)
20-25	7.8 (0.44)	7.05 (0.73)	0.75 (0.85)
25-30	6.22 (0.42)	6.28 (0.71)	-0.07 (0.82)
30-35	4.74 (0.39)	3.46 (0.63)	1.28 (0.74)
35-40	4.51 (0.39)	4.23 (0.65)	0.27 (0.76)
40-45	4.24 (0.38)	3.15 (0.62)	1.09 (0.73)
45-50	3.35 (0.37)	2.38 (0.60)	0.97 (0.70)
50-55	2.87 (0.36)	1.93 (0.58)	0.94 (0.68)
55-60	2.4 (0.35)	2.19 (0.59)	0.2 (0.69)
60-65	1.46 (0.33)	2.13 (0.59)	-0.67 (0.67)

correlated reactor-off event rate and the correlated reactor-on minus reactor-off event rate for each bin included in the count of the signal.

The sensitivity of the reactor-on minus reactor-off signal significance to the time cut was also examined by performing the counting procedure on the 79 days reactor-on and the 27 days of reactor-off data for several time intervals. The results are tabulated in Table 6.7. The significance of the reactor-on minus reactor-off correlated event rates peak over the interval 10-55 μs and then fall off over the next 25 μs. This behavior is in general agreement with Figure 6.18 and confirms a smooth variation of the significance around the interval chosen for the time cut.

6.7 Systematic Errors

The systematic uncertainty has contributions from detector stability, the selection cuts and from the specific parameters used to calculate the correlated event rate. The systematic error associated with detector stability was treated in Section 6.4 and is estimated to be 5.1% for the ADC threshold cut prompt:1850/delay:1650.

In Section 6.6.1, it was shown that varying the correlated decay constant alone has very little effect on the significance of the correlated event rate; a 10% change results in an

Table 6.7: The excess reactor-on minus reactor-off correlated events for 79 days reactor-on data and 27 days reactor-off data summed for the interevent time intervals shown in the left column. The errors are statistical only.

Correlated Event Signal Significance (79 Days Reactor-On/ 27 Days Reactor-Off)		
Time Interval (μs)	**Rx-On minus Rx-Off**	Significance
10-40	4.61 (2.02)	2.29σ
10-45	5.70 (2.14)	2.66σ
10-50	6.67 (2.26)	2.96σ
10-55	7.61 (2.36)	3.23σ
10-60	7.81 (2.46)	3.18σ
10-65	7.14 (2.55)	2.80σ
10-70	6.96 (2.64)	2.64σ
10-75	6.51 (2.71)	2.43σ
10-80	5.39 (2.80)	1.93σ
10-85	5.78 (2.86)	2.02σ

approximately 6% change in the final answer for the event rate and almost no change in the signal significance. Also, it was noted that the decay constant associated with the accidental coincidences was the same for reactor-on and reactor-off to within uncertainty. This fact was used to fix this parameter in subsequent analysis. An estimate of the error associated with this assumption can be obtained by making a 1σ change in the input value for both decay constants in Equation 6.6.5 and determining the impact on the final correlated event rate. The error associated with the choices of decay constants used in the Parametric Fit Method is estimated to be 2.0%.

Another systematic error associated with the Parametric Fit Method results from the fact that the number of accidental coincidences for reactor-on and reactor-off are not identical. Over the interval 10-65 μs, the difference is about 0.6 events/day. This equates to a systematic error of about 6.5% of the correlated event rate over this period. For the Counting Method, there is an error associated with the choice of the time cut of 65μs. To quantify this error, the best time cut is determined after performing a 1σ change to the input values in Equation 6.6.7, then the event rates are calculated at these time cuts (10-60 μs and 10-70 μs). The estimated error is 9.1%.

The individual contributions are shown in Table 6.8 and were added in quadrature to obtain the total systematic error for each analysis method.

Table 6.8: Contributions to the systematic error of the "Parametric Fit" and "Counting Method" analyses.

Source	"Parametric Fit" (%)	"Counting Method" (%)
Detector Stability	5.1	5.1
Decay Constants	2.0	N/A
Uncorr. Events	6.5	N/A
Time Cut	N/A	9.1
Total	**8.5**	**10.4**

6.8 Summary

The results of the analysis indicate good evidence that a 250 l water Cherenkov detector doped with a relatively small quantity of Gd can determine the difference in the reactor-on correlated event rate over that measured when the reactor is shut-down.

Two analyses were performed to obtain the difference in the reactor-on minus reactor-off correlated event rates. The first was a modified form of the analysis conducted for the SONGS I liquid scintillator detector experiment[157]. This analysis used statistical separation of the random coincidences and the true correlated event pairs. Correlated and uncorrelated event rates were calculated by separately fitting the reactor-on and reactor-off interevent time distributions to the sum of two exponentials and then using the fit values to integrate the total events. The final result for the reactor-on minus reactor-off correlated events per day via this method is: **8.3 ± 2.8(stat) ± 0.7(syst)**. The second procedure used in the analysis was a direct determination of the reactor-on and reactor-off correlated event rate after subtracting the accidental coincidences. A time cut of 10-65 μs was imposed for this analysis as it was the time cut which provided the optimum statistical significance. The final difference in correlated event rates between reactor-on and reactor-off is: **7.1 ± 2.5(stat) ± 0.7(syst)**. This value is in good agreement with the value obtained by the exponential fit method if one adjusts for the 10-65 μs interval.

Chapter 7

Conclusion

Two areas of original research were presented in this thesis.

The focus of the first area was the determination of the effect on transparency of adding $GdCl_3$ to water. If it could be shown that this neutron capture compound could be added to water without adverse effect on transparency or detector materials, this could dramatically improve the performance of water Cherenkov detectors and enable them to be used for a wide range of important physics and nuclear security applications. To help answer this question, a test facility was constructed at Lawrence Livermore National Laboratory to produce highly purified de-ionized water to which GdCl3 could be added. Additionally, a stainless steel Light Transmission measurement Arm (LTA) was constructed, and a laser and optics system were built and installed. Transparency measurements relative to a pure water baseline were made after adding the 0.2% by weight $GdCl_3$.

The major results of this testing indicate the following:

1. Pure water in stainless steel slowly looses transparency at 337, 400, and 420 nm. This is true for both the case of water exposed to oxygen and to water de-oxygenated via nitrogen bubbling to levels of 2% oxygen as compared to air.

2. The addition of $GdCl_3$ makes the transparency of water exposed to stainless steel decrease by as much as 15 times faster. This occurs at all three wavelengths tested.

3. Water stored in a polypropylene tank over the same time interval shows no or little loss of transparency.

4. The loss of transparency of water in stainless steel due to the addition of $GdCl_3$ does not appear to be *directly* from the GdC_3. This conclusion is based on the result that the degree of transparency loss is proportional to exposure time and intercepts the pure water baseline at time zero (i.e. when the $GdCl_3$ was added.).

The over-arching conclusion is that while $GdCl_3$ may be suitable for some detectors, it is **not** a suitable additive for detectors where the $GdCl_3$ comes in contact with steel walls.

Research on the possibility of adding other Gd compounds to water in stainless steel continues. Specifically, $Gd_2(SO_4)_3$ and $Gd(NO_3)_3$ have been recently tested. Soak testing of sample detector materials indicate no apparent damage [164] in each case. However, $Gd(NO_3)_3$ was seen to be strongly absorbing at wavelengths below 350 nm [165] and so $Gd_2(SO_4)_3$ appears to be the best choice. In addition, UC Irvine [166] is working on a water filtration system that will selectively filter non-Gd and non-(SO_4) impurities.

Although it would probably be cost prohibitive for large detectors, another potential area of research might include investigation into the application of coatings or liners to the steel. Should this be practical, the effects of $GdCl_3$ on the coatings and liners chosen would need to be investigated.

The second area of original research presented in this thesis involves the analysis of data from the SONGS water Cherenkov detector (WCD), a small volume (250 l) detector installed approximately 25 m from the SONGS Unit 2 nuclear reactor. A previous experiment using liquid scintillator successfully demonstrated the detection of reactor antineutrinos and the ability to track burnup and changes in reactor power over time-scales of a few hours [147]. The purpose of the SONGS WCD experiment was to determine if a WCD detector doped with Gd could also observe antineutrino events.

An off-line gain correction procedure was used to verify stable detector performance as measured by events passing specific energy thresholds per day. Once detector stability had been shown, two techniques were used to determine the difference in the correlated event rate when the reactor was operating versus when it was shut-down.

In the first technique, the interevent time distribution of correlated event pairs, a prompt event followed by a delayed event, was fit to a two exponential function. By fixing the decay constants in the function, one was able to determine the difference in amplitudes for the correlated portion of the interevent spectrum and compare them for the case of reactor-on and reactor-off. It was determined that the difference in correlated reactor-on minus reactor-off events per day was 8.3 ± 2.8(stat) ± 0.7(syst).

In the second technique, the number of reactor-on and reactor-off correlated events above the accidental uncorrelated background were directly counted over the interevent time interval 10-65 μs. With this method a difference of 7.1 ± 2.5(stat) ± 0.7(syst) events per day was determined.

These values are in agreement and indicate an excess of correlated events over background (reactor-off) with the reactor operating. Unfortunately, the experiment lacked continuous calibration data. The lack of calibration data made both tuning the energy threshold and gain calibration difficult. Thus the only measurement that could be made was the reactor-on versus reactor-off event rate.

The antineutrino event rate of a perfectly efficient equivalently sized detector (1.7×10^{28} protons) is approximately 1000 events per day so that one may estimate the efficiency of our detector as only about 1%, indicating room for improvement in the detector design. The primary reasons for such a low efficiency are the large threshold cuts used in the analysis (necessitated by lack of shielding) and the small size of our detector (which allowed the Gd capture gammas to escape before they had deposited their total energy in the detector). A larger (1 ton) follow-on detector designed from lessons learned from this initial effort is under construction by the LLNL collaboration.

Even so, our experiment provides a hint (at the 2.8σ level) of the first detection of antineutrinos from a gadolinium-doped water Cherenkov detector. It is hoped that our small experiment helped to pave the way for future experiments using this type of detector to achieve their full potential as antineutrino and neutron detectors.

Bibliography

[1] J.F. Beacom and M. R. Vagins, Phys.Rev.Lett **93**, 171101 (2004).

[2] W. Coleman, A. Bernstein, S. Dazeley, R. Svoboda, Nucl.Instrum.Meth. **A595**, 339 (2008).

[3] H. Murayama *"The origin of neutrino mass"*, Physics World, May 2002.

[4] Kenneth S. Krane, *Introductory Nuclear Physics*, John Wiley & Sons Inc., 2nd Ed. 1988, pp. 272-274.

[5] J. Rigden *The Overestimation of Niels Bohr*, The New York Sun, 11 July 2007.

[6] E. Fermi, Ill. Nuevo Cimento Series **11**(1), 1 (1934).

[7] E. Fermi and F.L. Wilson (translator) *Fermi theory of beta decay*, Rev.Mod.Phys. **71**, S96, (1999).

[8] D. Perkins, *Introduction to High Energy Physics*, 4th ed. (Cambridge University Press, Cambridge U.K, 2000).

[9] M.K. Gaillard, P.D. Grannis, F.J. Sciulli, *The Standard Model of Particle Physics*, Rev.Mod.Phys. **71**, S96 (1999).

[10] G. Danby *et al.*, Phys.Rev.Lett. **9**(1), 36, (1962).

[11] M. Perl *et al.*, Phys.Rev.Lett. **35**, 1489 (1958).

[12] K. Kodoma *et al.*, Phys.Lett. **B504**, 218 (2001).

[13] C. Amsler *et al.*, *Neutrino Flavors*, Particle Data Group, PLB667 (2008).

[14] M. Goldhaber, L Grodzins, A.W Sunyar, *Helicity of Neutrinos*, Phys.Rev. **109**, 1015 (1958).

[15] M. Turner, in ASP Conference Proceedings **291**, edited by K. R. Sembach, J. C. Blades, G. D. Illingworth and R. C. Kennicutt, Jr., 253 (2003).

[16] Y. Fukuda *et al.*, Phys.Rev.Lett. **81**, 1562 (1998).

[17] S.F. King, Rep.Prog.Phys. **67**, 107 (2004).

[18] M.Gell-Mann, P.Ramond and R.Slansky, in *Supergravity*, edited by P. Van Nieuwenhuizen and D.Z.Freedman, North Holland, Amsterdam, 1979, p.315.

[19] T.Yanagida, in *Proc. of the Workshop on the Unified Theory and Baryon Number in the Universe*, edited by O.Sawada and A.Sugamoto, KEK Report No.79-18, Tsukuba, Japan, 1979.

[20] S. Sarkar, Proc.IndianNatl.Sci.Acad. **70**A, 163 (2004).

[21] Pijushpani Bhattacharjee, J.Astrophys.Astr. **18**, 263 (1997).

[22] Mark Vagins, PRAMANA, **67**(4), 691 (2006).

[23] F. Mantovani, L. Carmignani, G. Fiorentini, M. Lissia, Phys.Rev. **D69**, 013001, (2004).

[24] T. Araki *et al.*, Nature, **436**, 499 (2005).

[25] V.I. Kopeikin, V.V. Sinev , Particles and Nuclei Letters., **5**(108), 41 (2001).

[26] J. Bahcall, *Neutrino Astrophysics*, paperback ed. (Cambridge University Press, Cambridge U.K., 1989).

[27] John N. Bahcall and Raymond Davis, Jr., *An account of the development of the solar neutrino problem*, in Essays in Nuclear Astrophysics, edited by C A. Barnes, D. D. Clayton, and D. Schramm (Cambridge University Press, 1982), pp. 243-285.

[28] M. Honda, T. Kajita, K. Kasahar, S. Midorkawa, T. Sunuki, Phys.Rev. **D73**, 043006 (2007).

[29] T. Sunuki textitet al. *Atmospheric neutrino and muon fluxes*, in 29th International Cosmic Ray Conference, Pune, (2005) pp. 101-104.

[30] M. Schwartz, Phys. Rev. Lett. **4**, 306 (1960).

[31] B. Pontecorvo, J. Exp. Theor. Phys. (U.S.S.R.) **37**, 1751 (1959) [tranlation: Sov. Phys.-JETP **10**, 1236 (1960)].

[32] Sacha Kopp, *Accelerator Neutrino Beams*, Physics Report **439** (3), 101 (2007).

[33] Neuchâtel Particle Physics Group [online], Institut de Physique, Université de Neuchâtel, (http://www.unine.ch/phys/corpus.htm).

[34] B. M. Pontecorvo, Zh. Exp. Teor. Fiz., **53**, 1717 (1967).

[35] L. Wolfenstein, *Lepton Physics and CP Violation*, in Proceedings of the International Workshop on "Neutrino Oscillations in Venice", July 24-26, 2001 Instituto Ventio di Sciencze, Lettere ed Art. (http://neutrino.pd.infn.it/conference2001/proceedings).

[36] L. Wolfenstein, Phys.Rev. **D17**, 2369 (1978).

[37] S.P. Mikeyev and A.Y. Smirnov Sov.Journ.Nucl.Phys. **42**, 913 (1985).

[38] Solar Neutrino Exp.(http://www.sns.ias.edu/ jnb/SNexperiments/experiments.html).

[39] Davis, R., Prog.Part.Nucl.Phys, **32**, 13 (1994).

[40] Q.R. Ahmad *et al.*, Phys.Rev.Lett. **87**, 071301 (2001).

[41] Q.R. Ahmad *et al.*, Phys.Rev.Lett. **89**, 011302 (2002).

[42] S.F. King, *Neutrino Mass* arXiv:0712.1750v1 [pop-ph].

[43] M. Maltoni, T. Schwetz, M. A. Tortola and J.W.F. Valle, New J.Phys., **6**, 122 (2004).

[44] C. Arpesella *et. al.*, Phys.Lett. **B658**, 101 (2008).

[45] Y. Ashie *et al.*, Phys.Rev. **D71**, 112005 (2005).

[46] M.H. Ahn *et al.*, Phys.Rev. **D74**, 072003 (2006).

[47] E. Alio *et al.*, Phys.Rev.Lett. **94** 081802 (2005).

[48] M.H. Ahn *et al.*, Phys.Rev. **D74**, 072003 (2006).

[49] P. Adamson *et. al.*, Phys.Rev. **D77**, 072002m (2008).

[50] M. Apollonio *et al.*, Phys.Lett. **B420**, 397, (1998).

[51] F. Boehm *et al.*, Phys.Rev. **D64**, 112001 2001.

[52] T. Araki *et al.*, Phys.Rev.Lett. **94**, 081801 (2005).

[53] S. Abe *et al.*, Phys.Rev.Lett. **100**, 221803 (2008).

[54] B. Kayser, arXiv 0804.1497v2 [phys-hep].

[55] W. J. Marciano and A. I. Sanda, Phys.Lett. **B67**, 303 (1977).

[56] B. W. Lee and R. E. Shrock, Phys.Rev. **D16**, 1444 (1977).

[57] A.B. Balantekin, arxiv:0601113v1 [phys-hep].

[58] S. Dodelson, G. Gyuk, M.S. Turner, Phys.Rev. **D49**, 5068 (1994).

[59] G.G. Raffelt, Phys.Rev. Lett. **64**, 2856 (1990).

[60] J.M. Lattimer and J. Cooperstein, Phys.Rev. Lett. **61**, 23 (1988).

[61] A.G. Beda *et al.*, Physics of Atomic Nuclei **79**, 1873 (2007).

[62] V. Barger, D. Marfatia, and K. Whisnant, Int.J.Mod.Phys. **E12**, 569 (2003).

[63] M.V. Diwan, arXiv:0211026v1 [hep-ex].

[64] Yuichi Oyama, Talk at International Conference on New Trends in High-Energy Physics (Crimea2005), Yalta, Ukraine, Sep 10-17, 2005, arXiv:0512041v2 [hep-ex].

[65] Kendra Snyder, *NOνA: a neutrino appearance experiment*, Symmetry Magazine 02:10, Dec05/Jan06, pp9-11.

[66] R. Plunkett, Journal of Physics: Conference Series 120, 052044 (2008).

[67] V. Barger, D. Marfatia, and K. Whisnant, Phys.Rev. **D65**, 73023 (2002).

[68] P.Huber, M. Lindner, W. Winter, ed. N. Goot, Nucl.Phys. **B654**, 3 (2003).

[69] P.Huber, M. Lindner, W. Winter, *Neutrino Superbeam Scenarios At the Peak* Proceeding of the APS/DPF/DPB Summer Study on the Future of Particle Physics (Snowmass 2001) ed. N. Goot C010630, E102 (2001).

[70] M. L. Chu, arXiv:0701029v1 [hep-ex].

[71] Charles Lane, *The Double Chooz Experiment* in Proceedings of 34th International Conference on High Energy Physics, Philadeplia PA, Sep 2008.

[72] The Reno Experiment, http://cms.skku.ac.kr/wiki/index.php/RENO.Experiment.in.Korea

[73] E W Otten *et al.*, Rep.Prog.Phys. **71**, 086201 (2008).

[74] P.D.G Review of Particle Physics, Eur.Phys.J. **C3**, 313 (1998).

[75] K. Assamagan *et al*, Phys.Lett. **B335**, 231 (1994).

[76] J. Wolf, arXiv:0810.3281v1 [physics-ins-det].

[77] E. Andreotti *et al.*, Nucl.Instrum.Meth. **A572**, 208 (2007).

[78] H. V. Klapdor-Kleingrothaus, I. Krivosheina, A. Dietz, and O. Chkvorets, Phys. Lett. **B586**, 198 (2004).

[79] S. Schonert *et al.* Nucl.Phys. **B145**, 242 (2005).

[80] E. Fiorini Phys.Rept. **307**, 309 (1998).

[81] C.E. Aalseth *et al. The proposed Majorana* ^{76}*Ge double-beta decay experiment* in Nuclear Physics B - Proceedings Supplements Volume 138, January 2005, pp. 217-220.

[82] M. Danilov textitet al., Phys.Lett. **B480**, 12 (2000).

[83] C. Arnaboldi, Phys.Rev.Lett. **95**, 142501 (2005).

[84] Kai Zuber, *Neutrino Physics*, (IOP Publishing Ltd., 2004), p. 383.

[85] K. Hagiwara *et al.* P.D.G Review of Particle Physics, Phys.Rev. **D66**, 010001 (2002).

[86] J. Lesgourgures and S. Pastor, Phys.Rept. **429**, 307 (2006).

[87] K. Sato, K. Takahashi, and S. Ando, *Supernova Neutrinos and Their Implication for Neutrino Parameters* in Proceedings of the 2002 International Symposium on Cosmology and Particle Astrophysics (COSPA 02) pp 228-242.

[88] W. Hill, J. C. Niemeyer, M. Reinecke, and C. Travaglio, Memorie della Societa Astronomica Italiana **74**, 942 (2003).

[89] R. Svoboda *et. al.*, IAU Circ. 4340, Ed. B.G. Marsden, 1, (1987).

[90] K. Hirata *et al.*, Phys.Rev.Lett. **58**, 1490 (1987).

[91] R.M. Bionta *et al.*, Phys.Rev.Lett. **58**, 1494 (1987).

[92] H.-T. Janka, *What can neutrinos tell about supernova explosions?*, in Astrophysics in Germany, Status and Prospects 2003, Universitat und Forschungszentrum Karlsruhe, 16-18 Sep 2003.

[93] J. F. Beacom, R. N. Boyd and A. Mezzacappa, Phys.Rev.Lett. **85**, 3568 (2000).

[94] G. S. Bisnovatyi-Kogan and Z.F. Seidov, Annals N.Y.Acad.Sci **422**, 319 (1984).

[95] S. Ando and K. Sato, NewJ.Phys. **6**, 170 (2004).

[96] G.L. Fogli, E. Lisi, A. Mirizzi, and D. Montainino, Phys.Rev. **70**, 013001 (2004).

[97] M. Malek *et al.*, Phys.Rev.Lett. **90**, 061101 (2003).

[98] M. Wurm et al., Phys.Rev. **D75**, 023007 (2007).

[99] J.F. Beacom and M. R. Vagins, Phys.Rev.Lett **93**, 171101 (2004).

[100] K. Scholberg *Supernova neutrino detection* Proc. of 22nd International Conference On Neutrino Physics And Astrophysics (Neutrino 2006), Sante Fe, New Mexico, 13-19 Jun 2006). arXiv:0701081 [astro-ph].

[101] C. Callan, F. Dyson, S. Treiman, *Neutrino Detection Primer*, JSR-84-105, JASON, The MITRE Corporation, (1988).

[102] E. Kolbe, K. Langanke and P. Vogel, Phys.Rev. **D66**, 013007 (2002).

[103] J. F. Beacom, W. M. Farr and P. Vogel, Phys.Rev. **D66**, 033001 (2002).

[104] J.F. Beacom and P. Vogel Phys.Rev. **D60**, 033007 (1999).

[105] G. Fiorentini and C. Acerbi, Astropart.Phys. **7**, 245 (1997).

[106] B. Pontecorvo, *Chalk River Report*, PD205, (1946).

[107] C. J. Horowitz, K. J. Coakley and D. N. McKinsey, Phys. Rev. D **68**, 023005 (2003). arXiv0302071 [astro-ph].

[108] D. Dangelo, *Towards the detection of low energy solar neutrinos in BOREXino: data, readout, data reconstruction and background identification*, Technische Universitat Munchen, PhD Thesis, (2006).

[109] Cowan, C, F. Reines, F. Harrison, E. Anderson, and F. Hayes, Phys.Rev. **90**, 493 (1953).

[110] I. V. Sanin, G. N. Markov, and N. G. Ivchenko, Atomnaya Energiya, **27**(4), (translated) 354 (1969).

[111] W. R. Leo, *Techniques for Nuclear and Particle Physics Experiments*, Springer-Verlag (1987).

[112] A. Bernstein, V. Gupta, and T. West, *An Assessment of Antineutrino Detection as a Tool for Monitoring Nuclear Explosions* , Sandia Natiional Labratory Report SAND99-8497, (1999).

[113] W.C. Haxton, Phys.Rev.Lett. **76**, 1562 (1996).

[114] R.S. Raghavan, S. Pakvasa, and B.A. Brown, Phys.Rev.Lett **57**, 1801 (1986).

[115] G. von Dardel and N.G. Sjostrand, Phys.Rev. **96**, 1566 (1954).

[116] I. Shimizu, Nuclear Physics **B168**, 147 (2007).

[117] B. Achkar *et al.*, Nucl.Phys. **B434**, 503 (1995).

[118] Jrgen Wendland *Integral Fluxes, Day-Night, and Spectrum Results from SNO's 391 Day Salt Phase* Fundamental Interactions: Proceedings of the 20th Lake Louise Winter Institute Lake Louise, Alberta, Canada, 20 - 26 February 2005, arXiv:0507058v1 [hep-ex].

[119] A. Morel *et.al. Optical properties of the "clearest" natural waters* Limnol, Oceanogr. **52**(1), 217 (2007).

[120] M. Vagins, (http://sn1987a-20th.physics.uci.edu-1105-vagins.pdf).

[121] M. A. Hayat *Cancer Imaging* 1st. Ed. (Academic Press, 2007), p. 63.

[122] T. J. Haley, K. Raymond, N. Komesu, H.C. Upham, Brit. J. Pharmacol. *17*, 526 (1961).

[123] S. Yoneda, N. Emi, Y. Fujita, M. Omichi, S. Hirano and K.T. Suzuki, Brit.Fundam.Apll.Toxicol. *28*, 65, (1995).

[124] S. Dierks, *Material Safety Data Sheet for Gadolinium Chloride*, Jan 1991

[125] M. L. Chu, arXiv:0701029v1 [hep-ex].

[126] Bicron products BC-521 and BC-525, Bicron Corp. 12345 Kinsman Rd., Newbury OH 44065-9677.

[127] Table of Nuclides, (http://necs01.dne.bnl.gov/CoN/index.html).

[128] R. Svoboda, *Results from Long-Term Soak Testing of Super-Kamiokande Materials in a 2% $GdCl_3$ Aqueous Solution*, Sep 2006, (Unpublished Department of Energy Report).

[129] G. Guillian, J. Learned, Marc Rosen, and M. Vagins, *A SKAT-based Measurement of the Attenuation Length of Light of Water with Dissolved Gadolinium*, April 2004, (Unpublished).

[130] A. T. Reghunath *et. al.*, Def.Sci, **41**(1), 1 (1991).

[131] J. D. Jackson, *Classical Electrodynamics* 3rd ed. (John Wiley Sons, Inc. 1999), pp 468-470.

[132] A. Morel, *Optical Properties of pure water and pure seawater*, in Optical Aspects of Oceanography, edited by N. Jerlov and E. Steeman-Neilson, (Academic Press, New York, 1974) pp 1-24.

[133] F. Bohren, D. R. Hoffman, *Absorption and Scattering of Light by Small Particles* paperback ed. (John Wiley & Sons Inc., 1998).

[134] H. Buiteveld, *The optical properties of pure water*, SP1E Vol.2258 Ocean Optics Xl (1994) pp 174-183.

[135] Y. Fukuda *et. al.*, Nucl.Instrum.Meth. A **501**, 418 (2003).

[136] High-Q, Inc., *Reagent-Grade Water Newsletter*, issue No. 0201, (High-Q,Inc., Wilmette, IL.,2002).

[137] Sterilight(R) Ultraviolet Disinfection System, *Model S24Q-Gold*, R-Can Environmental Inc. Guelph, Ontario Canada, N1H7X4 (www.r-can.com).

[138] Model VSL-337ND-S User Manual, Spectra-Physics PN 000-318A Rev A, (2004).

[139] Model DUO-210 Service Manual, Spectra-Physics PN 999-210 Rev A, (1999).

[140] M.M. Neito, *et. al.*, Nucl.Sci.Engin. **149**, 270 (2005).

[141] Davis B. R. *et. al.*, Phys Rev. **C19**, 2259 (1979).

[142] P Vogel *et. al.*, Phys Rev. **C24**, 1543, (1981).

[143] K Schreckenbach *et. al.*, Phys Lett. **B160**, 325 (1985).

[144] Y.V.Klimov, *et. al.*, Atomnaya Energiya **76**, 130 (1994).

[145] A. Bernstein, N. Bowden, A. Misner and T. Palmer, J.Appl.Phys. **103**, 074905 (2008).

[146] N Bowden, *et. al.*, Nucl.Instrum.Meth. **A572**, 985 (2007).

[147] N Bowden, A. Bernstein, S. Dazeley and R. Svoboda, arxiv:0808.0698v2 [nucl-ex].

[148] A.I.Afonin *et.al.*, Sov.J.Nucl.Phys. **46**, 944 (1987).

[149] Patrick Huber and Thomas Schwetz, *Precision Spectroscopy with reactor antineutrinos*, Phys.Rev. **D70**, 053011 (2004).

[150] L. A. Mikaelian L.A. Proc. Int. Conf. Neutrino-77,V-2,383-387.

[151] G.Mention, (http://www.apc.univ paris7.fr/AAP2007/Talks/Mention.ppt).

[152] A.Porta, textitet.al., *Reactor antineutrino detection for thermal power measurement and non-proliferation purposes*, in Proc. Int. Conf. Physics of Reactors: "Nuclear Power: A Sustainable Resource" (2008).

[153] F.Suekane, (http://www.apc.univ-paris7.fr/AAP2007/Talks/Suekane.pdf).

[154] J.C. Anjos, *et. al.*, NuclPhys.Proc.Suppl. **155**, 231 (2006).

[155] N.S Bowden, *Reactor monitoring and safeguards using antineutrino detectors*, The XXIII Conf. on Neutrino Phys. and Astrophys., Journal of Physics: Conference Series 136 022008 (2008).

[156] S. Dazeley, A. Bernstein, N. Bowden, R. Svoboda, Nucl.Instrum.Meth. **A607**, 616 (2009).

[157] A. Bernstein and N. S. Bowden, arXiv:0612152v1 [physics.ins-det].

[158] T. Misui Earth, Moon, and Planets **99**(265), 273 (2006).

[159] Glen F. Knoll, *Radiation Detection and Measurement*, 2nd Ed. (John Wiley & Sons Inc., 1989), pp. 20 - 21.

[160] R.Brun, PAW Reference Manual, CERN Program Library Write-Up Q121 (1993).

[161] Will Farmer, *Characterization of PMTs Used in Water-Based Detector*, LLNL Internal Report, (2007).

[162] A. Roodman, *Blind Analysis in Particle Physics*, in the Proc. of PHYSTAT2003: Statistical Problems in Particle Physics, Astrophysics, and Cosmology, edited by L. Lyons, R. Mount, R. Reitmeyer, Menlo Park, California, 8-11 Sep 2003, pp TUIT001.

[163] F. James, CERN Program Library Long Writeup D506 (1994).

[164] Reports from Misui Engineering and Shipbuilding Co., LTD (2007) (Unpublished).

[165] Atsuko Kibayashi, arxiv:0909.5528v1 [astro-ph.IM].

[166] M.R. Vagins, *Selective Filtration of Gadolinium Trichloride for Use in Neutron Detection in Large Water Cherenkov Detectors*, A Proposal for the U.S. Department of Energy's Advanced Detector Research Program (2006).

Vita

William Fitzgerald Coleman was born in August 1961, in Evergreen, Alabama. After completing high school in Ponchatoula, Louisiana, he attended Southeastern Louisiana University where he graduated in 1983 with a Bachelor of Science degree in physics.

After graduation, he joined the United States Navy as an Engineering Duty Officer. While in the Navy, he attended the U.S. Naval Postgraduate School in Monterey, California, and graduated with the degree of Master of Science in physics in December, 1993.

He retired from the Navy in 2004 and entered the doctoral program in physics at Louisiana State University during the fall of that year. Since January 2006, he has been a full-time research associate in the Department of Physics and Astronomy.

He is married to the former Nancy Brum of Dartmouth, Massachusetts. They have one son, Lucas.